MEASUREMENT OF CEREBRAL METABOLISM AND VASCULAR FUNCTION WITH MAGNETIC RESONANCE IMAGING

APPROVED BY SUPERVISORY COMMITTEE

Hanzhang Lu, Ph.D. (Mentor)

A. Dean Sherry, Ph.D.

Vikram Kodibagkar, Ph.D.

Georgios Alexandrakis, Ph.D.

Roderick McColl, Ph.D.

ACKNOWLEDGEMENT

I want to give the most sincere thanks to my advisor, Dr. Hanzhang Lu for his five years' guidance. I had rewarding years under his mentorship. His insightful comments inspired my interest of neuroscience and magnetic resonance physics. His mentorship opened the door of research for me. From coming up the idea to publishing the paper, he guided me through every single step of conducting a good research. Moreover, he never fails to lead me out of the struggling and shed a light on my confusion. He always generously gave his brilliant opinions and in-depth suggestions. Discussing questions with him gave me great opportunities to prepare my scientific thinking and reasoning. Most of all, his devoted attitude for work, research and family shows me the merits of a successful scientist.

I am lucky to work with a group of kind and smart people. I want to thank my colleagues who helped me from various aspects. Jinsoo Uh and Chengguang Zhao shared a lot of their knowledge and academic experience, who laid out the foundation of my work. Uma Yezhuva, Peiying Liu and Yamei Cheng actively and constantly supported my "tedious" experiments. Our MR Technologist, Rani Varghese, and research coordinators, Kelly Lewis-Amezcua and Jennifer Fehmel, gave me so many conveniences for my experiments. My studies are also benefited from chalk talks with Sina Aslan and KC Tung.

I want to thank Dr. A. Dean Sherry, Dr. Vikram Kodibagkar, Dr. Georgios Alexandrakis and Dr. Roderick McColl for serving the defense committee, as well as Dr. Hanli Liu for serving the exam II committee previously. Their comments and critiques improved the quality of this work.

I also want to thank Mingxi Yang and Gus Perez for revising my writing. Their careful job made my lengthy writing easier to read.

I am grateful to the Advanced Imaging Research Center at University of Texas Southwestern Medical Center. I had great experience working at this nice environment. Besides the sate-of-art facilities, the friendly and inspiring research atmosphere motivates me every day. Faculties, stuffs and students work as a team beyond the boundary of groups. They assisted my studies in many ways.

Several people must be mentioned. They are administrative crew, Kay Emerson, Christene Sanders, Marilyn Jimmerson, Laura Hartley and Patricia Bleigh. Their patient and effective helps with the student issues made my graduate study much more enjoyable.

Beyond the science community, I am lucky to have nice friends and relatives around who let me feel I am not alone. I appreciate the valuable time I spent with them. Especially, I want to mention, Yujioa Sun (my cousin), Zhangyan Ma, Yuan Yang, Liyue Tong, Yongcheng Huang, Judith and David Howard, Meng Zhao, Heling Zhou, Mai Lin, Peiying Liu, Luo Ouyang, Yang Hu, Yan Fang, Jun Wang, Yong Wang, Zhuo Gan, Wei Liu, Junhui Zhen, Yao Ding,

Yemeng Kong, Rui Wan, Fei Chen, Pam Lee and her families, Xiaoping Chen and his families, Jingshun Zhang and his families, and Guosheng Xiang and his families.

Last but not least, the deepest gratitude goes to my dearest parents, Wenyuan Zhang and Muqi Xu. My Dad made his Ph.D. of biology in his 40s. He had to devote almost all his time on studying and research. During those days, my Mum had to work extra hard to take care of the family as well as her work. Their determination and persistence inspired me ever since. Along the way, their encouragement is the largest motivation for me to come oversea for the graduate school. Their love always makes me feel that they are just a phone-call away. They always consider all about me but forget themselves and guide me through both the good and difficult time because they know me so well. I dedicate this dissertation to them, my great parents.

MEASUREMENT OF CEREBRAL METABOLISM AND VASCULAR FUNCTION WITH MAGNETIC RESONANCE IMAGING

by

Feng Xu

DISSERTATION

Presented to the Faculty of the Graduate School of Biomedical Sciences

The University of Texas Southwestern Medical Center at Dallas

In Partial Fulfillment of the Requirements

For the Degree of

DOCTOR OF PHILOSOPHY

The University of Texas Southwestern Medical Center at Dallas

Dallas, Texas

July, 2011

MEASUREMENT OF CEREBRAL METABOLISM AND VASCULAR FUNCTION WITH MAGNETIC RESONANCE IMAGING

Feng Xu, Ph.D.

The University of Southwestern Medical Center at Dallas, July 2011

Mentor: Hanzhang Lu, Ph.D.

The brain relies on oxidative metabolism to function properly. Cerebral metabolic rate of oxygen ($CMRO_2$) is thus an important marker for brain health. Existing techniques for quantification of $CMRO_2$ with positron emission tomography (PET) or magnetic resonance imaging (MRI) involve special equipment and/or exogenous agents, and may not be suitable for routine clinical studies. To fill this gap, I developed a noninvasive method for quantifying whole brain $CMRO_2$. This method uses the Fick principle of arterio-venous difference

for the calculation of $CMRO_2$.and employs phase-contrast MRI for quantitative blood flow measurement and T_2-relaxation-under-spin-tagging (TRUST) MRI for venous oxygenation estimation. During this thesis, I conducted several technical development studies. I first optimized TRUST and phase-contrast MR imaging parameters and demonstrated the ability to measure $CMRO_2$ using completely non-invasive procedures. I further performed calibration and validations studies to show that blood oxygenation measured with TRUST reveals an excellent agreement with the gold standard Pulse Oximetry method. A final technical study was to improve the speed and reliability of TRUST MRI by shortening the scan duration by 60% while reducing the measuring error by half.

I have also applied this novel $CMRO_2$ method in better understanding brain physiology in younger and older adults. I studied the effect of CO_2 inhalation (also known as hypercapnia) on brain metabolism. A reduced $CMRO_2$ was observed and this effect was further supported by findings using functional connectivity MRI and electroencephalography techniques. I also investigated the effect of O_2 modulation (hypoxia and hyperoxia) on brain metabolism and showed a dose dependent effect of O_2 concentration on brain activity. Finally, I used this method to assess aged-related differences in brain metabolism and blood supply, and demonstrated a paradoxically higher metabolic rate in older adults, which may be associated with lower neural efficiency in elderly individuals.

TABLE OF CONTENTS

PRIOR PUBLICATIONS

1. **Xu F**, Liu P, Lu H. The effect of graded oxygen challenge on vascular and metabolic parameters. J Cereb Blood Flow Metab. In-preparation.

2. **Xu F**, Uh J, Liu P, Lu H. On improving the speed and reliability of T_2-Relaxation-Under-Spin-Tagging (TRUST) MRI. Magnetic Resonance in Medicine. In-press.

3. Lu H, **Xu F**, Grgac K, Qin Q, Liu P, van Zijl P. Calibration and validation of TRUST MRI for the estimation of cerebral blood oxygenation. Magnetic Resonance in Medicine. In-press.

4. Lu H, Huthison, **Xu F**, Rypma B. The relationship between M in "calibrated fMRI" and physiologic modulators of fMRI. ONIJ. In-press.

5. Lu H, **Xu F**, Rodrigue KM, Kennedy KM, Cheng Y, Flicker B, Hebrank AC, Uh J, Park DC. Alterations in cerebral metabolic rate and blood supply across the adult life span. Cereb Cortex. 21(6):1426-34, 2011.

6. **Xu F**, Uh J, Brier MR, Hart, J Jr, Yezhuvath US, Gu H, Yang, Y, Lu H. The influence of carbon dioxide on brain activity and metabolism in conscious humans. J Cereb Blood Flow Metab. 31(1):58-67, 2011.

7. Aslan S, **Xu F**, Wang PL, Uh J, Yezhuvath US, van Osch M, Lu H. Estimation of labeling efficiency in pseudo-continuous arterial spin labeling, Magnetic Resonance in Medicine, 63(3):765-771, 2010.

8. **Xu F**, Ge Y, Lu H. Non-invasive quantification of whole-brain cerebral metabolic rate of oxygen by MRI, Magnetic Resonance in Medicine, 62(1):141-8, 2009.

LIST OF FIGURES

LIST OF TABLES

LIST OF DEFINITIONS

$[O_2]_a$ Arterial Oxygenation including the dissolved oxygen.
$[O_2]_v$ Venous Oxygenation including the dissolved oxygen
ASL Arterial Spin Labeling
ATP Adenosine Triphosphate
BBB Brain Blood Barrier
BOLD Blood Oxygen Level Dependency
CBF Cerebral Blood Flow
$CMRO_2$ Cerebral Metabolism Rate of Oxygen
CNS Central Nervous System
dHb Deoxygenated Hemoglobin
fMRI Functional Magnetic Resonance Imaging
GABA γ-Aminobutyric acid
HbO Oxygenated hemoglobin
Hct Hematocrit
MRI Magnetic Resonance Imaging
NMR Nuclear Magnetic Resonance
NAD Nicotinamide Adenine Dinucleotide
NIRI Near Infra-Red Imaging
NO Nitric Oxide
OEF Oxygen Extraction Fraction
PET Positron Emission Tomography
qBOLD Quantitative BOLD
QUIXOTIC Quantitative Imaging of eXtraction of Oxygen and Tissue Consumption
SNR Signal to Noise Ratio
TCA cycle tricarboxylic cycle
TRUST T_2 Relaxation Under Spin Tagging
VASO VAscular Space Occupancy
Y_a Arterial Oxygenation
Y_v Venous Oxygenation

1 The review of cerebral energy metabolism

The cerebral energy metabolism can be used as a biomarker of the brain development and neural function. With the novel technology of magnetic resonance imaging (MRI), this parameter can be quantified *in vivo*. Before introducing my work on noninvasive measurement of cerebral and vascular function, I would like to review basic neurophysiology about energy metabolism. The chapter will start with the neural cytology, followed by the energy expense on various types of neural activities, and the energy production. The energetic metabolism is closely related to the blood supply, so this chapter also reviews the anatomy of blood supply and the neurovascular coupling.

This chapter is written based on the books of Augustine (2004), Champe (2008) and Siegelbaum (2000) (Augustine 2004; Champe *et al* 2008; Siegelbaum and Koester 2000).

1.1 Neuron cell and astrocyte

A neuron consists of a cell body, dendrites and an axon (Figure 1). The cell body, also known as soma, contains various cell organelles such as a nucleus, endoplasmic reticulum, ribosome, Golgi body, and mitochondria. The cell body is like a factory that 'assembles' the proteins needed for neuronal function. Cell bodies are located throughout both grey and white matter. At one end of the cell body, root-like structures are formed, which are called dendrites. Dendrites primarily appear in grey matter. Their function is analogous to roots, since

dendrites receive inputs from other neurons through their branches, and integrate the signals for further signal transduction at the axon. The axon transports the signal received from dendrites through its long tail, which can stretch to another neuron up to one meter away. The axon plays the important role in transmission of signals to other neurons. These signals are transported in the form of electric potential which is named as action potentials. The action potential is produced by the current of ions across cell membrane. To prevent the dissipation of these electrical signals during travel, the axon is sheathed in a layer of myelin, which helps to improve conductivity and keep electrical current within the axon. The terminus of the axon encounters the dendrites or cell body of the next neuron at a synapse. The synapse is the connection between two neurons where the signals are passed from one to the other. The synapses formulate a complicated neural network through millions of connections.

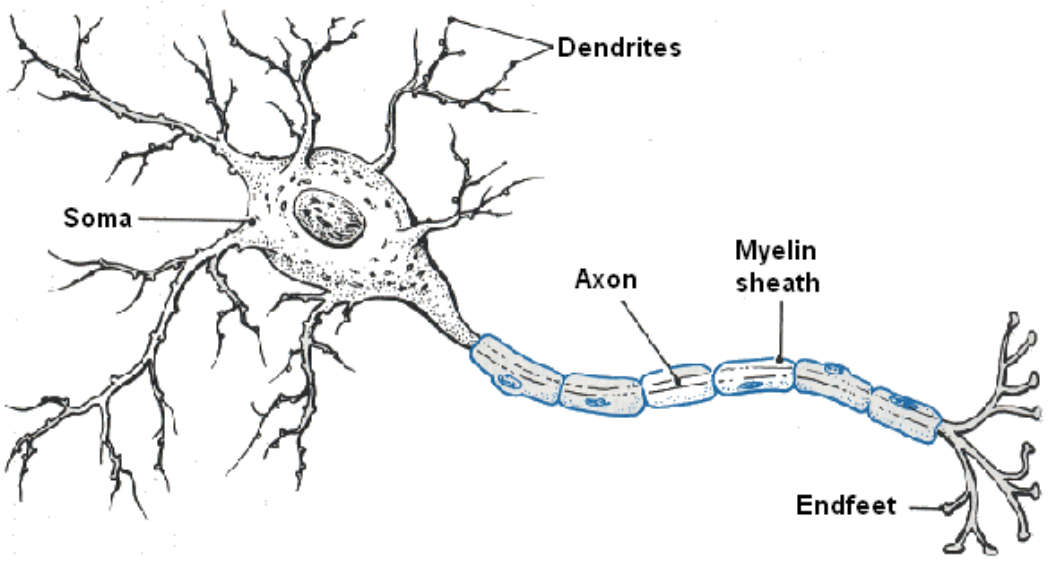

Figure 1 The diagram of a neuron cell.
The neuron consists of a cell body, also called soma, dendrites, and an axon. The dendrites have many branches that receive signals from previous neurons' axons. The axon is enclosed by a myelin sheath and sends out a signal to the next neuron (copied from website http://www.mindcreators.com/NeuronBasics.htm).

The glial cell is the supporting cell of the central nervous system (CNS). There might be twice more glial cells than neurons existing in the brain. They are divided into three categories, astrocyte, oligodendrocyte, and microglia. The astrocyte consists of two subtypes: fibrous astrocytes and protoplasmic astrocytes. Fibrous astrocytes elaborate long sparsely branched processes, which exist in white matter. Protoplasmic astrocytes have short and highly branched processes, which are located in grey matter. The branches of an astrocyte may project end-feet to neurons or the walls of blood vessels (Figure 2). These astrocytic endfeet on both vessel walls and neurons provide anatomic connections to allow neuron-vessel interactions. The significance of having such interactions includes maintaining a proper chemical environment for neurons as well as signaling vessel walls to regulate the blood flow. Astrocyte together with endothelial cells and neurons compose 'neurovascular units'. Among the unit, astrocytes mediate the signaling pathways involved in both neurons and vessels, and modulate permeability of the blood brain barriers (Abbott *et al* 2006). Consequently, the astrocytes give functional regulation to neurons as well as the anatomical support.

Oligodendrocytes form myelin sheaths for axons in white matter or are located adjacent to neuronal cell bodies in grey matter. Microglias are phagocytic

cells of the CNS. Similar to tissue macrophages, microglial cells react to injury and participate in repair processes.

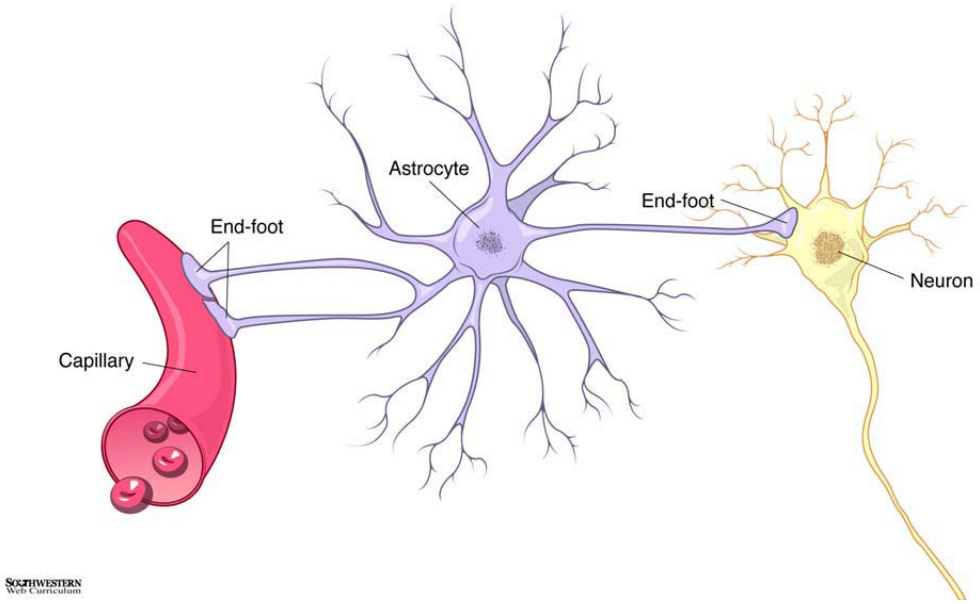

Figure 2 The diagram of the connection among the blood vessel, the neuron and the astrocyte.
The astrocyte has a star-like shape with branches projecting various processes. Its end-feet can make contact on neurons and/or the vessel wall (copied from University of Texas Southwestern Medical Center curriculum website).

1.2 Energy expenditure of neuronal and glial cells

The brain represents 2% of whole body weight but consumes 20% of the body's total energy budget (Attwell and Laughlin 2001). The brain's energy usage is mainly attributable to the activities of neuronal and glial cells. The neuronal activities include in-house protein synthesis, resting potentials, action potentials, signal transduction, synaptic potentials, and neural transmitter recycling. The glial cells spend energy in supporting and regulating neural and vascular activities.

The energy supporting neural and glial activities comes from exhausting adenosine triphosphate (ATP). The energy is produced when ATP is hydrolysized to adenosine diphosphate (ADP), or even adenosine monophosphorate (AMP). This conversion from ATP to ADP releases energy from breaking down a high energy bond (–P).

1.2.1 Maintenance of membrane potential

The cell membrane is embedded with ion channels that are specifically permeable to certain type of ions such as sodium (Na^+) and potassium (K^+). The ion concentration difference between the inner and outer membrane yields the membrane potential. For instance, the neuron maintains low sodium and high potassium concentrations inside the cell but high sodium and low potassium concentrations outside the cell. This ion gradient is maintained by osmotic pressure and the switching on and off of voltage dependent ion channels. So the potential across membrane is usually maintained around -70mV. The switching of ion channels can be triggered by electrical, chemical and mechanic stimuli. Opening ion channels would disturb the resting membrane potential due to the influx and efflux of ions. To sustain the resting state potential, Na^+/K^+ pumps must work against the gradient at the cost of ATP. The Na^+/K^+ pump binds three sodium ions from inside cell. The hydrolyzed ATP phosphorylates the pump which loses its affinity for sodium, and subsequently releases the sodium ions to the extracellular environment. Subsequently, two potassium ions are bound

outside of the cell wtih the pump. When the pump is dephosphorylated, it releases potassium ions to the intracellular space. The membraine potential spends energy in such way that the ion pumping cycle requires ATP.

1.2.2 Action potential

An action potential is initiated at the axon hillock at the time that the membrane potential exceeds a threshold. The increased membrane potential is usually resulted from the input signals from dendrites. The voltage-gated Na^+/K^+ channels will respond to the increased membrane potential by opening the channels. The opening of Na^+ channels precedes K^+ channels. The influx of Na^+ immediately raises the potential of inner membrane, so the membrane is depolarized. As such, the membrane potential can be raised significantly above zero. As K^+ channels open, the efflux of K^+ brings down the membrane potential gradually, therefore, the cell is again hyperpolarized. The peak of positive potential is called the action potential. Re-establishing the Na^+ and K^+ concentration gradient across the membrane requires Na^+/K^+ pumps and ATP.

Energy is also needed for transmitting action potential through axon, so there are mitochondria along the axon. The ion flow at the action potential depolarizes the neighboring membrane and provokes another action potential at an adjacent region. As the action potential is propagated along the axon, the ion gradients need to be reset at the cost of energy before the next action potential can propagate.

1.2.3 Synaptic transduction

Synapses are the communicating media between two neurons. This means of neuronal connection can be categorized into electrical synapse and chemical synapse. The majority of the synapses in the brain are chemical synapses. The neuron passing the signal out at the foot of the axon is called the presynaptic neuron and the neuron receiving the signal at its dendrites or cell body is called the postsynaptic neuron. Electrical synapses are located between two tightly associated neurons, and the electrical signal of the presynaptic neuron is instantly and directly transmitted to the postsynaptic neuron through gap-junction channels. The gap junction channels of two membranes form an array of hemi-channels allowing for the ion current to flow from the presynaptic membrane to the postsynaptic membrane.

The chemical synapse, on the other hand, is formed in a larger space between two neurons. The interneuronal space is called synaptic cleft. The electrical signal, i.e. the action potential, travels down to the end of the axon, and opens voltage-gated Ca^{2+} channels. The incoming Ca^{2+} binds the proteins associated with the membrane of vesicles that are filled with neurotransmitters and triggers vesicle fusion at the synaptic membrane. The neurotransmitters are released from vesicles and come out of the presynaptic neuron. Once they appear in the synaptic cleft, they bind the receptors on the membrane of the postsynaptic neuron. This binding triggers a cascade of reactions that open selective ion

channels at postsynaptic neurons, which eventually alters the postsynaptic membrane potential. The polarity of the changed potential depends upon the type of neurotransmitters that were released. Through chemical synapses, the electrical signal from the presynaptic axon is transferred to chemical signal at the synapse then finally converted back to electrical signal at the postsynaptic dendrites.

In electrical synapses, energy is mainly spent on restoring the ion gradient. But, in chemical synapses, energy is needed in various ways other than pumping ions. At the presynapse terminal, ATP is needed for transporting neurotransmitters, synthesizing enzymes, docking and fusing of vesicles. At the postsynaptic terminal, energy is used for activating the ligand-gated ion channels via neurotransmitters bind with metabotropic receptors. The metabotropic receptors, consisting of G-proteins or tyrosine kinases, confer the indirect regulation of opening iron chennels via a secondary messager which relays to phosphorylate the ion channel or activate protein kinases to regulate the opening of the channels. So this process involves the conversion of ATP to ADP, i.e. spending energy. Furthermore, the released neurotransmitters are taken up by astrocytes and recycled back to the presynaptic neuron to be docked in vesicles again. The metabolic pathways involving neurotransmitter recycling consumes energy as well.

1.2.4 Neurotransmitters recycling

The neurotransmitters are recycled from extracellular space directly or through the shuttle between astrocytes and neurons. In latter case, astrocyte is involved in some intermediate steps of recycling neurotransmitters. Take glutamate for example. After glutamate is released into the synaptic cleft, a large proportion is taken up by the astrocyte where the glutamate reacts with ammonia to become glutamine. In the neuron, glutamine is the precursor of glutamate. The flux of glutamine from astrocyte to neuron completes restoring glutamate in the neuron. The conversion of glutamate to glutamin requires an ATP dependent enzyme in the astrocyte. Therefore, part of the energy spent by an astrocyte is used for maintaining neuronal activities.

1.2.5 Summary

A good summary of energy expenditure of neurons and astrocytes is the following figure used by Attwell and Iaecola (Attwell and Iadecola 2002). While the fraction of energy expense is still under debate, the components of energy budget are fairly well understood.

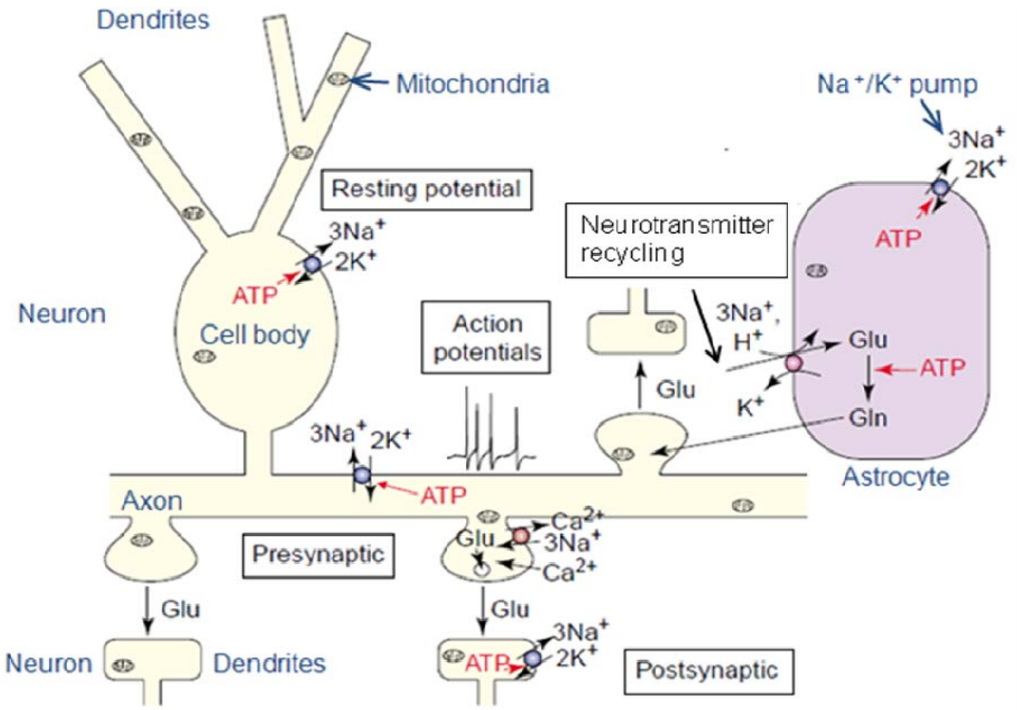

Figure 3 The schematic diagram of the energy expenditure.
The energy expense of an excitatory neuron and a glial cell, including housekeeping, maintaining ion gradients for resting state membrane potential, action potential and neurotransmitters recycling. (Modified based on Attwell and Iadecola 2002).

1.3 The energy generation

O_2 and glucose are the primary fuel for the brain. The majority of the energy is produced by the aerobic metabolism of glucose in which glucose is catabolized to CO_2 and O_2 is reduced to water. CO_2 is produced in the tricarboxylic cycle (TCA cycle) as the intermediate substrates of TCA cycle break down to smaller molecules (Figure 4). The O_2 does not directly participate in the reactions of the TCA cycle, instead, drives the TCA cycle by accepting the free electrons produced in certain steps of the TCA cycle. Transporting free electrons to oxygen yields the conversion of ATP from ADP and inorganic phosphate (Pi).

The energy is stored within the high energy phosphorus bond of ATP. Figure 4 shows the metabolic pathway of glycolysis and the TCA cycle and summarizes the production of ATP molecules and free electrons by reducing NAD^+ or FADH.

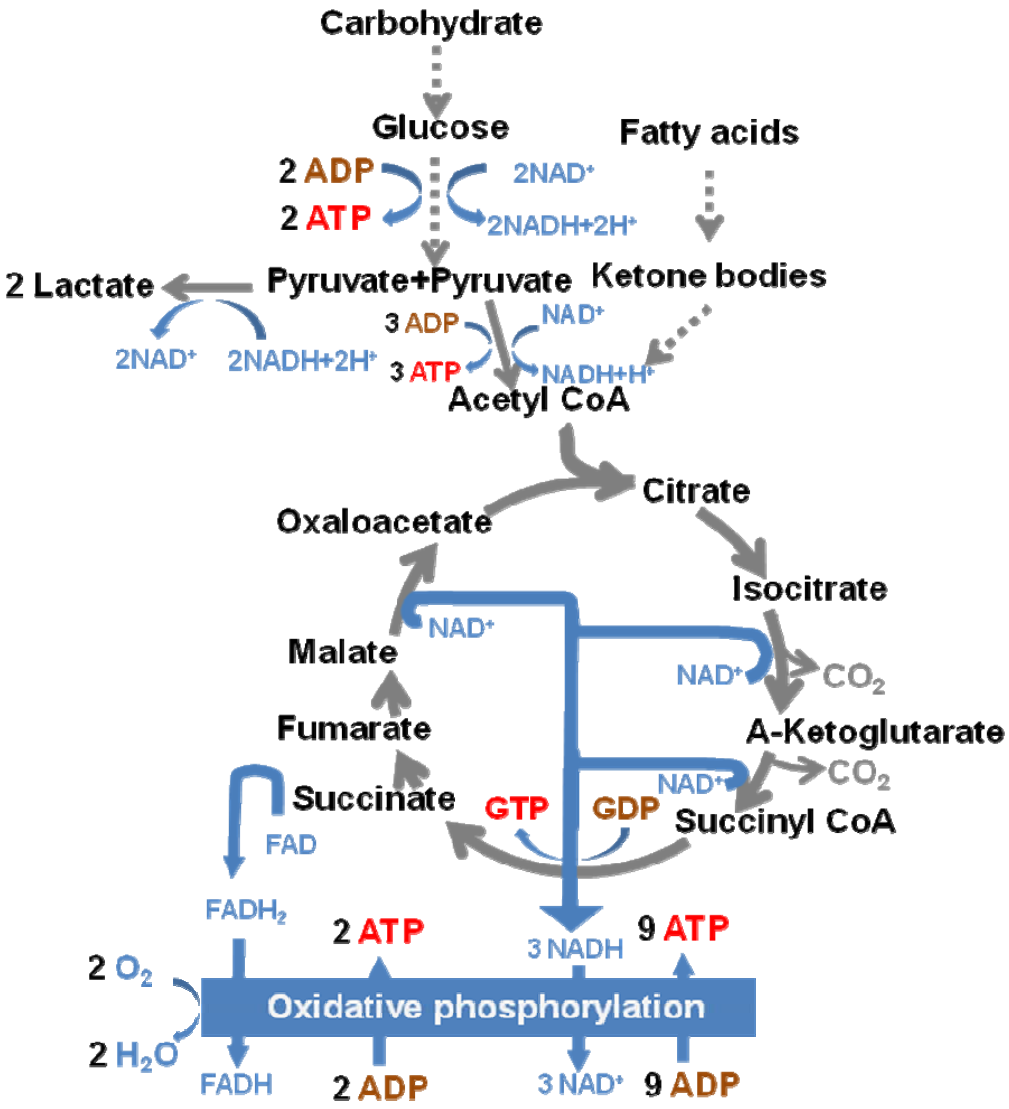

Figure 4 The skeleton of energy production of glycolysis and the TCA cycle.
One glucose molecule produces two pyruvate molecules and two ATP molecules through glycolysis. One pyruvate molecule is oxidized to one acetyl-coA molecule, and produces one free electron and three molecules of ATP. One acetyl-coA after one turn of the TCA cycle produces

four free electrons by reducing three NAD^+ molecules and one FADH. Three molecules of O_2.are used to take up six free electrons and fifteen molecules of ATP (modified based on (Champe *et al* 2008).

ATP is produced through electron transfer involving nicotinamide adenine dinucleotide (NAD) and NADH + H^+, a process facilitated by the electron transfer from O_2 to H_2O. The electron transport chain, illustrated in Figure 5 involves five steps at five protein complexes of mitochondrial membrane matrices, called complex I, II, III, IV and V. The electrons originate from the oxidation of the substrates. As a result, NAD^+ is reduced to NADH by accepting electrons from substrate oxidation. NADH is eventually oxidized back to NAD^+ via the reduction of oxygen. This Reduction-Oxidation (Redox) process is achieved by transporting the electrons through a series of conversions of coenzymes including NAD, flavin mononucleotide (FMN), flavin adenine dinucleotide (FAD), Coenzyme Q (CoQ) and the electron carriers ferrous ion (Fe^{2+}). Finally, O_2 takes up the electrons and is converted to H_2O. ADP is pumped from the intermembrane space into the mitochondrial space at complex V where efflux of protons driven by the electron transport chain returns mitochondrial space. Inside the mitochondrial space, ADP is phosphorylated to ATP (this process is summarized in Figure 5).

ATP production is well maintained in normal physiological condition. When available glucose is not sufficient for the energy demands of the brain, ketones become the alternative substrates for producing acetyl CoA and, consequently, maintain ATP production of the TCA cycle. On the other hand,

when there is not sufficient oxygen for an immediate energy demand, ATP can still be produced without the presence of O_2 through anaerobic metabolism of glucose. In anaerobic metabolism, ATP is produced less efficiently than in aerobic metabolism per unit glucose (Figure 4).

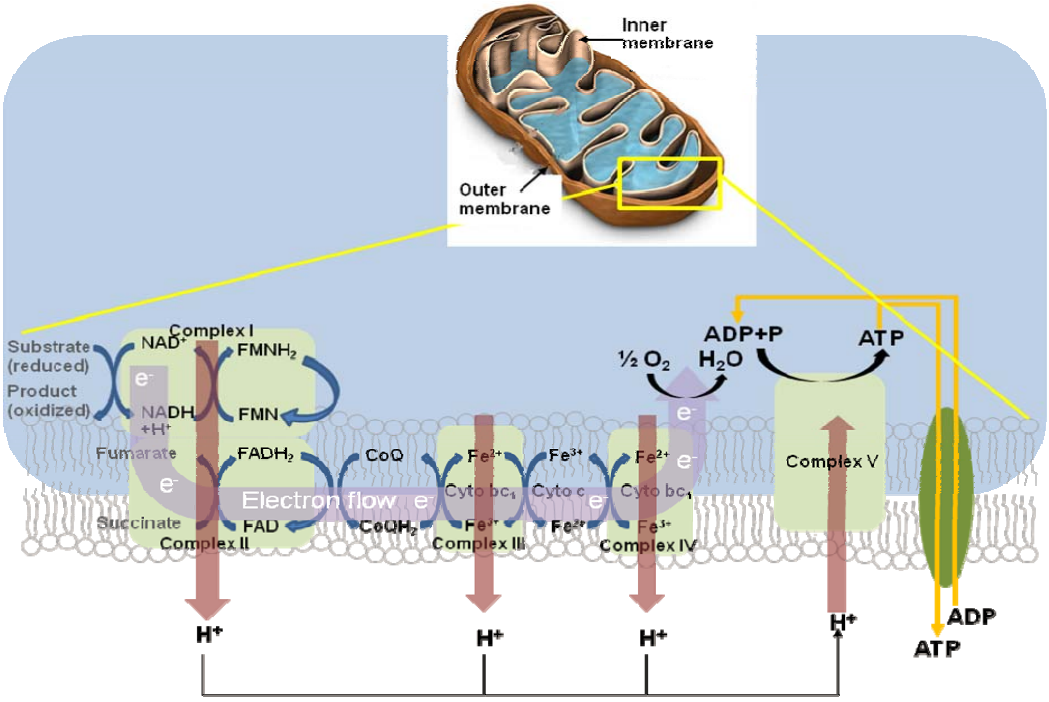

Figure 5 The diagram for the electron transport chain and ATP production.
Free electrons produced in TCA cycle are transported through protein complexes at the mitochondrial membrane. ADP is pumped into the mitochondria and converted to the ATP at the complex V (modified based on (Champe *et al* 2008).

1.4 Cerebral vasculature and neurovascular coupling

1.4.1 Blood supply and drainage

The oxygen and glucose are carried to the brain through the blood stream. The cerebral blood flow (CBF) is derived from the internal carotid and vertebral

arteries. The internal carotid arteries branch from common carotid arteries and the vertebral arteries branch from subclavian arteries. The internal carotid arteries travel straight up to the brain and enter the intracranial cavity via the carotid canal without making any branches. The vertebral arteries ascend along the spinal column through foramina in the transverse process of the sixth cervical vertebrae (C6) to C2. Then, they bend laterally and posteriorly to pass the foramen transversarium of C1 then turn superiorly and medially behind the atlas (C1), and finally enter the intracranial cavity though the foramen magnum (Figure 6a). After entering the intracranial cavity, the left and right internal carotid arteries as well as the left and right vertebral arteries merge at the base of the brain and form the circle of Willis (Figure 6b). The internal carotid arteries mainly supply the anterior circulation of the brain and vertebral arteries supply the posterior circulation. (Huettel *et al* 2004).

The venous drainage originates from the capillary bed then gradually joins veins on the surface of the cortex and finally joins the superior sagittal, inferior sagittal or transverse sinuses. Most of the cortical veins originate from deeper layers of the brain and join superficial sinuses. The superior sagittal sinus passes in the midline between the two hemispheres from anterior to posterior. The inferior sagittal sinus also runs anterior to posterior parallel with the superior sagittal sinus. They meet at the junction of the transverse sinus and then split

bilaterally and continue as the transverse sinuses, which are followed by sigmoid sinuses, and finally exit the brain via internal jugular veins.

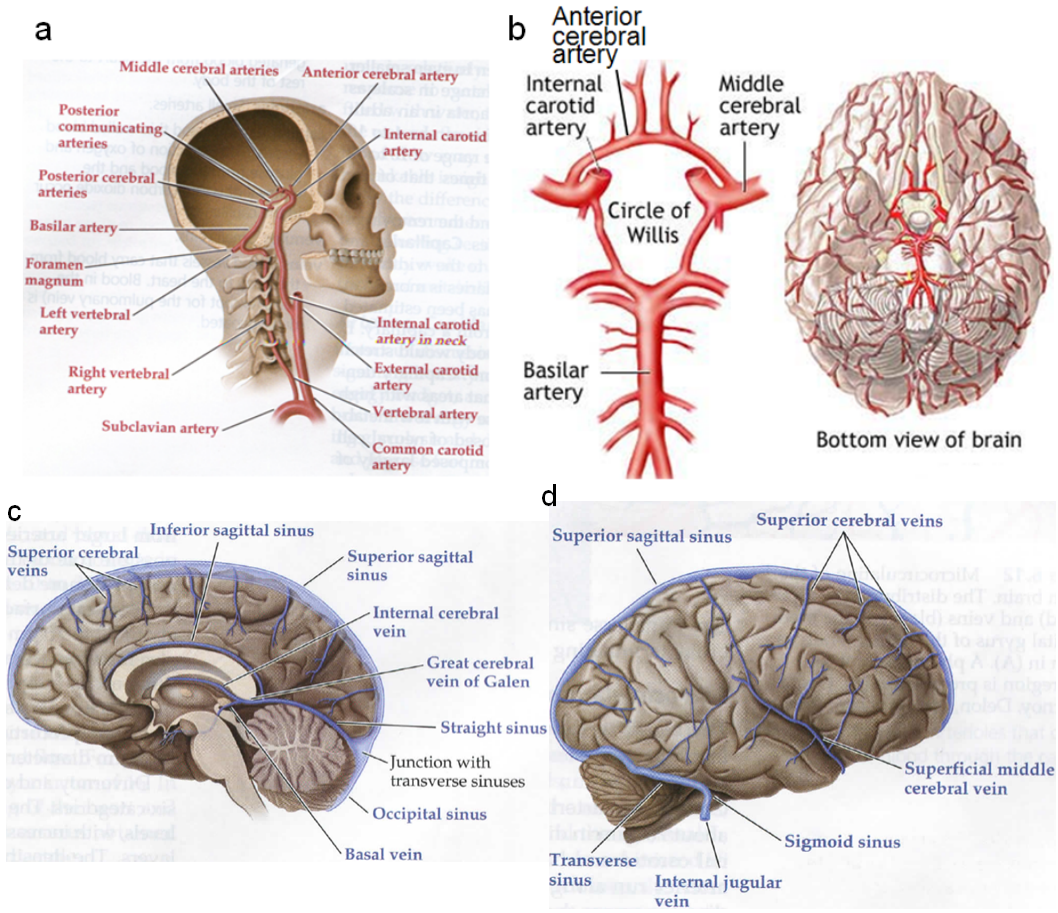

Figure 6 The diagram of blood supply of the brain.
(a) Sagittal view of internal carotid and vertebral arteries traveling from neck to the brain. (b) Dorsal view of blood circulation formed by internal carotid and vertebral arteries. (c) Medial sagittal view of venous sinuses. (d) Lateral sagittal view of sinuses (copied from (Huettel *et al* 2004).

1.4.2 How oxygen and glucose enter the brain

Glucose and oxygen enter the brain tissue at capillaries where the vessel wall is relative thinner comparing to arteries, but they still need to cross a barrier to get into neurons. The molecules that can pass through the interface between

brain tissues and blood vessels are highly selective because there are continuous tight junctions that separate these two compartments. These tight junctions are formed by a layer of endothelial cells. The endothelial cells wrap around the capillary, and connect adjacent cells tightly without any gap. The tight junction prevents many lipid insoluble molecules from moving from intravascular space into the intracellular space of the brain tissue hence is named blood-brain-barrier (BBB).

Unlike glucose, ketones are the catabolites of lipid soluble fatty acids, and thus can cross BBB through free diffusion. Glucose is a hydrophilic molecule and has low solubility in fat. Yet it is the primary energy substrate of the brain. Glucose traverses the BBB via a carrier mediated transport. GLUT-1 and GLUT-3 are the most abundant glucose transporters in the brain, which facilitate the transfer of glucose to neurons and astrocytes. This transfer mechanism is sufficient enough to transport glucose by two to three times more than that is normally utilized in the brain. The GLUT-1 is insulin independent, so the brain glucose level remains relatively stable.

O_2, on the other hand, is freely diffusible across the BBB depending on the gradient of pressure. The oxygen tension of brain tissue depends on oxygen tension of blood (Vazquez *et al* 2010). Like O_2, CO_2 and H_2O can also cross the BBB by free diffusion. The metabolized CO_2 can be carried away by the blood stream.

1.4.3 Neurovascular coupling

The interaction between the neuron and the vasculature has long been the topic of interest in physiology and neuroscience (Roy and Sherrington 1890), and it forms the basis of several brain mapping techniques such as functional magnetic resonance imaging (fMRI) (Bandettini et al 1992; Frahm et al 1992; Kwong et al 1992; Ogawa et al 1992), positron emission tomography (PET) (Fox and Raichle 1986) and infra-red optical imaging (Vanzetta and Grinvald 1999). These techniques essentially use the hemodynamic response as a surrogate to assess the evoked neural activities.

The hemodynamic response originates from neural stimulation and is hypothesized to provide the metabolic need of neurons. The evoked neural activity causes increased local CBF which supplies the need for fuel, especially when there is a thirst for oxygen. The stimulated CBF always delivers more oxygen than what is needed. As a result, the venous capillaries drain more oxygenated blood at the activated regions. The elevated CBF, known as "functional hyperemia" leads to increases in blood volume and blood oxygenation. These hemodynamic features yield the basis of the contrast for various neuroimaging techniques with MR, such as blood-oxygen-level-dependent (BOLD) fMRI, arterial-spin-labeling (ASL) MRI, vascular space occupancy (VASO) MRI and so on.

The mechanism of functional hyperemia involves neurons, pyramidal cells, interneurons and astrocytes, even though hyperemia is initiated by cortical neural activities. The cortical neuron communicates with vasculature through various ways, as shown in Figure 7. The cortical neurons, interneurons, pyramidal cells and astrocytes make contact with microvessels through their endfeet and modulate blood flow with various vasodilators. The vasodilators can be categorized by their origins. For example, nitric oxide's (NO) cellular origin is interneurons, prostaglandin (PgE2) originates from pyramidal cells, and epoxyeicosatrienoic acids (EETs) is found in astrocytes. The process of releasing vasodilators is associated with the activation of excitatory or inhibitory neurotransmitters, i.e. glutamate or γ-Aminobutyric acid (GABA) (Cauli and Hamel 2010). The action of these vasodilators takes effect on increasing CBF in different temporal resolutions and amplitude scales. For instance, NO affects on vasculature more rapidly than EETs. But EETs are more effective for a bigger augment of CBF than NO (Cauli and Hamel 2010).

However, the amplitude, spatial distribution or time course of CBF changes does not correlate well with oxygen metabolism or glucose metabolism, even though hyperemia is primarily driven by the neural activity and is closely associated with energy demand (Raichle and Mintun 2006). The increased CBF brings excessive amount oxygen which is partially recruited by the neural activation. The post-stimulus CBF returning to baseline precedes the oxidative

metabolism recovery (Hua *et al* 2011). The spatial hemodynamic response extends the CBF changes beyond the activated region due to the extension of blood supply network and the overcompensation mechanism. Therefore, CBF changes reduce the spatial specificity of neuronal activity (Smirnakis *et al* 2007). These mismatches of hemodynamic response and energy demand suggest that increased CBF is not a simple surrogate for neural activity.

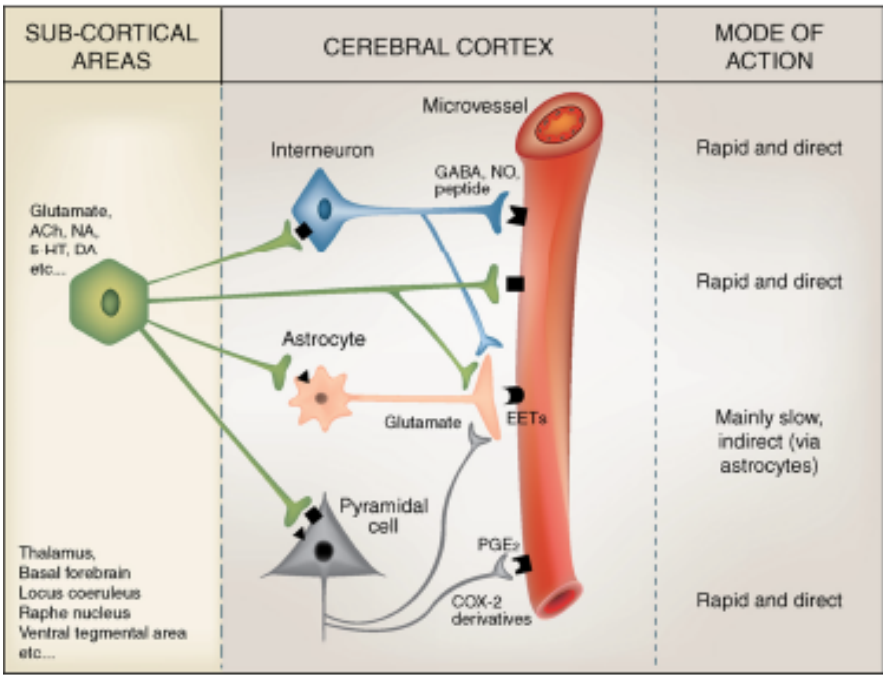

Figure 7 The communication of neurons and vasculature.
The neuron affects the blood vessel directly, or via an interneuron, a pyramidal cell or an astrocyte. Different vasodilators have various temporal reactions (copied from (Cauli and Hamel 2010)).

1.5 Summary

Neural activities heavily rely on the ATP molecule for their energy expense. Their ATP demand is mainly met by aerobic metabolism of glucose. CBF delivers the fuel of ATP (glucose and O_2) to neurons and regulates the

supply responding to the demand via hemodynamic response. This neurovascular coupling mechanism renders the exciting contrast for neuroimaging techniques such as fMRI and PET. However, the complexity of neuronal-astrocytic-vascular interaction challenges the interpretation of the signal observed by fMRI or PET. A straightforward method of assessing the neural activity should be able to target at energy metabolism directly.

2 The review of techniques for measuring cerebral metabolic rate of oxygen ($CMRO_2$)

2.1 The Fick principle based methods

2.1.1 The Fick principle

The Fick principle tells that the whole brain O_2 consumption is equal to be the arterial-venous (A-V) O_2 difference (Figure 8). The arterial blood carries O_2 molecules to the brain. The brain tissue extracts some of them to utilize immediately. The brain only extracts the amount is needed and does not store extra O_2. Therefore, the remaining O_2 is drained by the veins. Efficiently carrying O_2 relies on the protein called hemoglobin expressed in erythrocytes. The O_2 carrying ability is proportional to the fraction of erythrocytes in a unit blood volume, which is named hematocrit (Hct). For a given Hct level, the amount of O_2 that **can be carried** in unit blood is a constant (noted by C_h in units of μmol O_2/ml blood). Clearly, venous blood carries less O_2 than arterial blood, even though they have same CBF and C_h. The amount of O_2 **actually carried** by blood is equal to the product of blood flow (CBF), C_h and the oxygenation (Y) that is the fraction of erythrocytes binding with O_2. The aterio-veneous O_2 content difference is determined by the difference of Y, i.e. Y_a-Y_v. Y_a-Y_v is also known as oxygen extraction fraction (OEF), representing the fraction of O_2 extracted by the brain tissue. The cerebral metabolic rate of oxygen ($CMRO_2$) is therefore quantified by the CBF, OEF and C_h as the following equation

Eq.1

$$CMRO_2 = CBF \cdot Y_a \cdot C_h - CBF \cdot Y_b \cdot C_h = CBF \cdot (Y_a - Y_b) \cdot C_h$$

where CBF is the amount of blood passing through the brain tissue in ml/100g/min, Y_a and Y_v are arterial and venous oxygenations (in %), respectively, The value of C_h is reasonably well established in hematology and pulmonary physiology literature (Guyton and Hall 2005). Considering that each gram of hemoglobin can carry 55.6 µmol of oxygen (Guyton and Hall 2005) and there are 15 grams of hemoglobin in 100ml blood (at a typical hematocrit of 0.44) (Guyton and Hall 2005), the value of C_h is 833.7 µmol O_2/100ml blood. Under normal conditions, arterial blood is close to fully oxygenated, thus Y_a can be considered 100%, or measured by Pulse Oximeter.

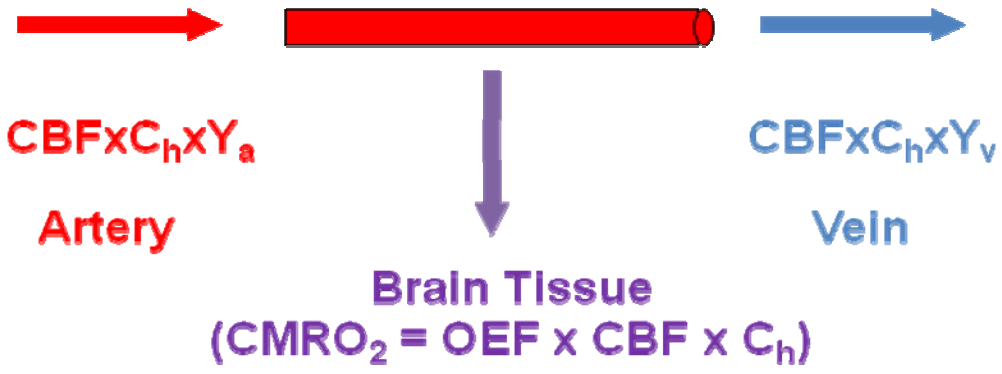

Figure 8 The diagram of the Fick principle.
The cerebral metabolic rate of oxygen ($CMRO_2$) is the difference between the O_2 supplied by arteries and the O_2 drained by the veins per unit time. The O_2 carried by the blood can be computed by the product of cerebral blood flow (CBF), oxygenation (Y) and a constant C_h representing the amount of O_2 carried by unit of blood. The CBF and oxygen carrying ability noted by C_h are same between arteries and veins. So the arterio-venous difference is primarily determined by the extraction fraction (OEF = Y_a-Y_v). Therefore, $CMRO_2$ is a function of OEF, CBF and C_h.

2.1.2 MRI techniques for measuring oxygen extraction fraction (OEF)

Oxygen extraction fraction (OEF) is the deference of arterial oxygenation (Y_a) and venous oxygenation (Y_v) (i.e. OEF=Y_a-Y_v). Since Y_a can be easily measured by Pulse Oximetry noninvasively at the finger, the measurement Y_v is the key for quantifying OEF. So far, three types of noninvasive MR techniques have been developed to quantify Y_v using the endogenous contrast, deoxygenated hemoglobin.

2.1.2.1 Intravascular T_2/R_2 method

Thulborn, et al. found that the blood sample R_2 (=$1/T_2$) is correlated with blood oxygenation (Y) (Thulborn *et al* 1982). Thulborn used the early work done by Luz and Meiboom to explain the altered blood R_2. Luz and Meiboom reported and quantified that the R_2 of the solvent is a function of protons exchanging rate between the solvent and the water that have different proton larmor frequencies (Luz and Meiboom 1963). The proton larmor frequency, short for larmor frequency, is the proton spinning frequency and is proportional to the applied field strength. Here, deoxygenating blood (i.e. lowering Y) is the mechanism for altering the blood proton larmor frequency. The water exchanging between the tissue and the blood leads to the change of blood R_2. This special property of the blood is due to the characteristics of the hemoglobin that consists of four heme groups (Fe^{2+}). There are two structural forms of the hemoglobin, oxygenated (HbO) and deoxygenated hemoglobin (dHb). Binding with O_2 (HbO), the iron

stays at the low spin state. HbO appears to be diamagnetic, which has no different proton larmor frequency from the plasma. Losing O_2 (dHb), the iron moves to the high spin state. dHb is paramagnetic, which yields a different proton larmor frequency. The paramagnetic dHb disturbs the homogeneity of local magnetic field, which alters the larmor frequency of water proton adjacent to dHb. The effect of dHb is regional. The protons exchange between the site from dHb and the site from plasma, HbO or extravascular space. The blood R_2 is altered through the water exchange between an altered larmor frequency regime and the unchanged regime. In addition, the amount of chagne is Y dependent. Later, using the exchange model derived by Luz and Meiboon's model, van Zijl sophisticatedly modeled that the shifted blood proton larmor frequency was a function of Y (Golay *et al* 2001; van Zijl *et al* 1998), shown in the Eq.2

Eq.2

$$R_2 = A + B \cdot (1 - Y) + C \cdot (1 - Y)^2$$

Where A, B, C are functions of Hct, R_2 of dHb, HbO and plasma, water exchange rate, and pulse sequence parameters. These coefficients can all be fitted by *in vitro* blood R_2 measurement. No assumption for each parameter is needed. The relationship of R_2 and Y can be better illustrated by the Figure 9.

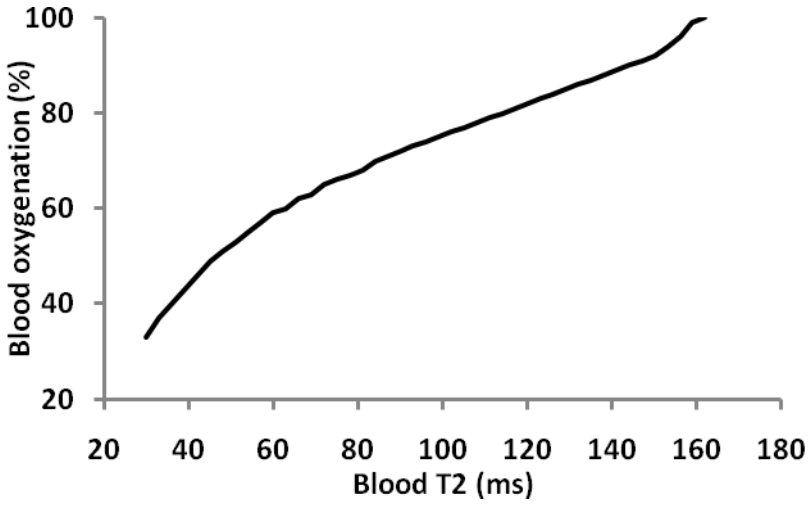

Figure 9 The calibration curve for converting blood T_2 to blood oxygenation.

Once *in vivo* blood R_2 is measured, we can estimate Y on humans based on a calibration plot. So the challenge is how to separate blood signal and measure the blood R_2 on human brain given that a single image voxel always contains multi-components, e.g. tissue, CSF and blood. The recent developed technique, T_2-Relaxation-Under-Spin-Taging (TRUST) MRI, applies spin tagging on the venous blood (Lu and Ge 2008b). The spin tagging refers to tagging blood signal magnetically and comparing the tagged image to untagged image. The difference between the two images yields the pure blood signal and eliminates static tissue signal because blood tagging selectively attenuates the blood signal but not tissue signal. Following spin tagging pulse, TRUST uses non-slice selective τCPMG to perform T_2 preparation on the whole brain which is not sensitive to outflow effect. Therefore, one can measure venous blood R_2/T_2 by

applying TRUST on sagittal sinus, which can be converted to oxygenation using the calibration curve.

So far TRUST only works well on major veins because it does not have enough sensitivity to separate venular signal due to the difficulty of tagging the capillary blood. Therefore, TRUST only gives a point measurement of Y at major vessels and the whole brain OEF. The new technique named QUantitaitve Imaging of eXtraction of Oxygen and TIssue Consumption (QUIXOTIC) (Bolar 2010) utilizes the velocity selective tagging method to selectively preserve the low velocity signal that contains tissue and capillary blood signals. QUIXOTIC sequence waits for a certain time to allow the capillary blood to flow to venules; it then applyies another flow velocity selective tagging to separate the venular blood from tissue and capillary arterial blood. The two successive flow tagging separate the blood signal from tissue signal and venous blood from arterial blood in microvasculature. Therefore, regional $CMRO_2$ and OEF mapping is able to be achieved by this novel idea. However, selecting proper threshold for the velocity of capillary blood and waiting time could substantially impact the signal sensitivity, specificity and signal to noise ratio (SNR), given that venular signal only takes less than 5% signal of each voxel. The accuracy and reliability of this technique require further validation.

In summary, the intravascular R_2 approach is insensitive to the field inhomogeneity, and does not require any assumption on physiological parameters.

Although this method is based on chemical exchange model, all the parameters in the blood R_2-Y model can be obtained from another *in vitro* measurement. In this sense, this approach is assumption-free since every parameter is measured.

2.1.2.2 Intravascular susceptibility method

This susceptibility method proposed by Haacke et al, relates the phase change caused by dHb susceptibility to the Y level (Haacke *et al* 1997). The magnetic susceptibility is the degree of magnetization of a material in response to an applied magnetic field. As explained above, the HbO is diamagnetic and does not affect the surrounding magnetic field, while the dHb is paramagnetic and reduces local magnetic conduction, consequently disturbs local magnetic field. dHb presents a different susceptibility from HbO. So the blood susceptibility (χ_{blood}) is different from tissue susceptibility (χ_{tissue}). The deviation between the two ($\Delta\chi_{blood\text{-}tissue}$) is dependent on Y: $\Delta\chi = Hct \cdot (1-Y) \cdot \Delta\chi_{do}$ where χ_{do} is a constant representing the susceptibility difference between fully deoxygenated and fully oxygenated blood.

Assuming the blood vessel is an extremely long straight cylinder, the difference in field strength between blood and surrounding tissue caused by dHb is $\Delta B_{blood-tissue} = B_0 \cdot (\cos^2\theta - 1/3) \cdot \Delta\chi_{blood-tissue}$, where θ is the angle between blood vessel and magnetic field. Because the larmor frequency (ω) is proportional to the field strength (B), $\omega = \gamma B$, where γ is a ratio, called gyro-ratio. The

difference of larmor frequency (Δω) between blood and tissue is proportional to the difference of field strength, $\Delta\omega_{\text{blood-tissue}} = \gamma\Delta B_{\text{blood-tissue}}$. So after a certain echo time (TE), a phase variation (Δφ) is observed between blood and tissue since the two regions' protons process at different frequency. In this way, Y is linearly related to the Δφ through Δχ, ΔB, Δω.

$$\Delta\varphi_{\text{blood-tissue}} = \Delta\omega \cdot TE \cdot = \gamma \cdot \Delta B \cdot TE = \gamma \cdot B_0 \cdot \Delta\chi_{blood-tissue} \cdot 1/6(3\cos^2\theta - 1) \cdot TE$$
$$= \gamma \cdot B_0 \cdot Hct \cdot (1-Y) \cdot \Delta\chi_{do} \cdot 1/6(3\cos^2\theta - 1) \cdot TE$$

where Δφ is measureable by using susceptibility weighted MR sequence with a small flip angle and short TE (Jain *et al* 2010). Then Y can be calculated backward.

The advantage of this susceptometry technique is that it provides greater temporal resolution, as data acquisition can be completed within a couple of minutes. But, this technique is heavily dependent on the homogeneity of magnetic field (both B0 and B1 homogeneity) and sensitive to blood vessels' orientation and length. In addition, this approach requires pure blood signal to correctly quantify the phase angle of blood. Thus it is limited to great blood vessels that are bigger than the size of a single voxel.

2.1.2.3 Extravascular R_2' method

The R_2' ($R_2' = R_2^* - R_2$) relaxation is the signal loss due to a defined "static dephasing regime". The static dephasing affects the mesoscopic field of extravascular tissue protons. This reversible mesoscopic field inhomogeneity is

caused by dHb, the degree of its effect is related to blood oxygenation (Y), venous blood volume, hematocrit (Hct) and local magnetic field strength (Yablonskiy and Haacke 1994).

In this static inhomogeneity theory, the signal decay is modeled by a few complicated functions associated with R_2' and venous blood volume. An et al used a hybrid spin echo and gradient echo sequence to acquire R_2' weighted signals; and assumed all the extravascular signals are originated from the same type of tissue (An *et al* 2001). He and Yablonskiy dissected the R_2' signals into multicomponents including blood, grey matter, white matter, cerebral and cerebrospinal fluid (He and Yablonskiy 2007).

This method gives voxel based OEF and $CMRO_2$, which is important for investigating the focal changes. However, this method is based on several assumptions that might be violated in certain circumstances. For example, the static dephasing regime ignores diffusion effect that might be important for modeling capillary signal. Blood vessels are assumed to be infinitely long, which may be biased on microvasculature. The success in estimating R_2' is challenged by the macroscopic field inhomogeneity due to static B0 inhomogeneity, susceptibility artifact of air cavity in the bone and other reasons.

2.1.3 The non-MR method based on the Fick principle

The earliest technique based on the Fick principle to measure $CMRO_2$ was invented by Kety and Schmidt (Kety and Schmidt 1948a). This method requires

an inhaling gas tracer (e.g. nitrous oxide (N_2O)) and sampling blood at the peripheral artery and internal jugular vein. A CBF is obtained from the two time courses of arterial N_2O and venous N_2O base on modeling. Y_a and Y_v are measured by a gas analyzer. This early attempt of quantifying $CMRO_2$ involves invasive procedures, sampling arterial blood at femoral artery and venous blood at jugular vein. Since the arterial blood sample is taken at a peripheral site away from the brain and the venous blood sample on one side of the internal jugular veins, a number of factors could impact the accuracy of the measurement. The confounding factors include the heterogeneity of N_2O along the blood stream, the asymmetric CBF across hemispheres, the ex-cerebral contamination due to muscles and fats, the mental stress during the experiment, the N_2O effect on physiological state, and so on (Lassen 1978).

2.2 Alternative methods for measuring $CMRO_2$

2.2.1 PET- $^{15}O_2$

Positron emission tomography (PET) detects gamma rays produced by annihilating a pair of positron and electron. PET images are reconstructed based on the origins of gamma rays that correspond to the locations of radioactive tracers. The radiotracers are the biological active components synthesized with radioactive isotopes producing positrons. When the positrons meets with the electrons existed in the natural biological environment, gamma rays are emitted.

The radiotracers are specially designed molecules that selectively participate the metabolic pathways we are interested. Thus, once the isotopes are tagged onto drugs and metabolites, PET imaging can be used to assess the uptake of drugs and metabolic functions.

Based on the development of implementing PET technique in measuring CBV and CBF (Herscovitch *et al* 1983; Raichle *et al* 1983), Mintun et al proposed the following method to quantify the $CMRO_2$ (Mintun *et al* 1984; Videen *et al* 1987). Because the $CMRO_2$ essentially measures how much O_2 is metabolized to H_2O, Mintun's method uses PET to image the amount of ^{15}O labeled O_2 converted to $[O^{15}]H_2O$ in the brain tissue. The challenge is how to distinguish the gamma rays emitted by $^{15}O_2$ and $H_2{}^{15}O$ in tissue and blood. Mintun's method uses the kinetic model shown in Figure 10 to separate the radioactivity related to the tissue $CMRO_2$ and the radioactivity carried by CBF. In this method, a dose of $^{15}O_2$ gas is inhaled by a couple of breaths. The inhaled $^{15}O_2$ is carried by blood to the brain tissue, and the metabolized $H_2{}^{15}O$ is freely diffused across the tissue and blood boundary. Then the accumulated $H_2{}^{15}O$ and remaining $^{15}O_2$ are drained by veins to the heart and they are continuously circulated in the artery. The image intensity measured by PET (C_{PET}) depends on the gamma counts from $^{15}O_2$ (noted by $C(^{15}O_2)$) and $H_2{}^{15}O$ (noted by $C(H_2{}^{15}O)$,

$$C_{PET} = C_{blood,\ tissue}(^{15}O_2) + C_{blood,\ tissue}(H_2{}^{15}O).$$

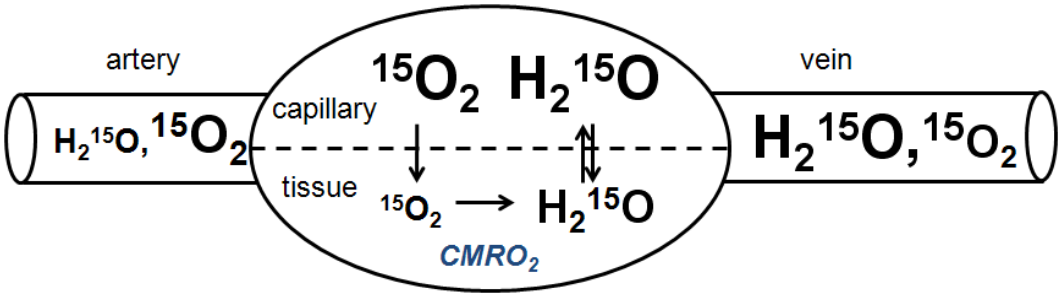

Figure 10 The model for PET $^{15}O_2$ measuring $CMRO_2$.
The $^{15}O_2$ is inhaled, and delivered to the brain in artery. $^{15}O_2$ is reduced to $H_2{}^{15}O$ as soon as it enters the tissue at the rate of $CMRO_2$. $H_2{}^{15}O$ is in the equilibrium between the tissue and blood. The relative size of the symbols represents the relative concentration of elements in each compartment.

To simplify the model, a few assumptions are applied, such as 1) O_2 is reduced to H_2O as soon as it enters tissue, so that the tissue only contains the radioactivity of $H_2{}^{15}O$ and all of the radioactivity of $^{15}O_2$ comes from blood; 2) H_2O freely diffuses between brain and blood, and the water content ratio of tissue and blood is constant across all brain regions, such that the tissue water content can be converted to blood water content ($C_{artery}(H_2O)$); 3) the capillary $^{15}O_2$ concentration is the average of arterial compartment and venous compartment in each voxel, so that the capillary $^{15}O_2$ can be scaled to arterial $^{15}O_2$ while venous $^{15}O_2$ content is related to arterial $^{15}O_2$ content by OEF; 4) the volume fraction of artery, capillary and vein are 0.16, 0.01 and 0.83, therefore, each compartment blood volume can be scaled to arterial blood volume (CBV_{artery}); 5) the hematocrit ratio of large vessel and small vessel is assumed a constant; 6) the arterial input function is assumed to be similar between peripheral and central.

Therefore, the $C_{blood,\ tissue}(^{15}O_2)$ and $C_{blood,\ tissue}(H_2{}^{15}O)$ in the kinetic model are simplified to $C_{PET} = C_{blood}(O_2) + C_{blood,tissue}(H_2O)$

$$C_{blood}(O_2) = f_1(CBF, C_{artery}(O_2))$$
$$C_{blood,tissue}(H_2O) = f_2(CBF, C_{artery}(H_2O)) + OEF \cdot f_3(CBF, CBV_{artery}, C_{artery}(O_2))$$

Where, f_1, f_2 and f_3 are integration functions of the parameters in the parentheses. Then, OEF can be expressed as:

$$OEF = \frac{C_{PET} - f_1(CBF, C_{artery}(O_2)) - f_2(CBF, C_{artery}(H_2O))}{f_3(CBF, CBV_{artery}, C_{artery}(O_2))}$$

In the equation, C_{PET} is the gamma count from PET images; the CBF and CBV are constant, and can be measured by a separate PET scan using $H_2{}^{15}O$ and $C^{15}O$ tracors respectively; the arterial $^{15}O_2$ and $H_2{}^{15}O$ radioactivity are measured by arterial sampling at the peripheral artery (e.g. radial artery). The gamma count of $^{15}O_2$ and $H_2{}^{15}O$ are measured from erythrocytes and blood plasma after centrifuging blood samples.

Even though this PET ^{15}O technique measures oxygen metabolism directly, its kinetic model uses various assumptions which might introduce measurement bias. The measurement has to be taken after the inhaled O_2 reaches equilibrium, a process that takes a couple of circulation from heart to the brain. Meanwhile, the half life of ^{15}O is less than 2 minutes. The signal that can be detected might be noisy, so the low SNR of PET image gives difficulties for a robust estimation. The accuracy of the measurement highly depends on the arterial input function

($C_{artery}(H_2O,O_2)$) acquired by blood sampling. Similarly, the additional CBF and CBV measurements with other types of radiotracers also add noise to the OEF quantification. Because ^{15}O has a short half life, an onsite cyclotron is needed which is considerably expensive for a research study, preventing a widely application of this method. In addition, the arterial line is placed for frequently sampling arterial blood, which is an invasive and difficult procedure. The timing in sampling arterial blood and measuring its radioactivity is very critical, which may involve many researchers. Therefore, this technique is not widely used for research study or clinic examination.

2.2.2 NMR- $^{17}O_2$

Applying the idea of PET to NMR, Zhu et al demonstrated the $CMRO_2$ map measured by magnetic resonance spectroscopy (MRS) with $^{17}O_2$ (Zhu *et al* 2002; Zhu *et al* 2005). The $^{17}O_2$ molecule is not detectable in blood because of the extremely short T_2 and T_1 when $^{17}O_2$ bind with hemoglobin. So only the signal originated from $H_2{}^{17}O$ can be measured, making the NMR kinetic model of oxygen metabolism in the brain much simpler than PET model (Figure 11). The measured $H_2{}^{17}O$ content ($C_{NMR}(H_2{}^{17}O)$) comes from two sources, the tissue metabolism and the blood flow. Similar to PET, ^{17}O is given by inhaling $^{17}O_2$. Water signal $C(H_2{}^{17}O)$ is measured over the period of inhalation phase and washout phase after stop inhaling $^{17}O_2$. The tissue $H_2{}^{17}O$ signal changes as a

function of $CMRO_2$, CBF and Y, determining arterial/venous $H_2{}^{17}O$ concentration ($C_{artery/vein}(H_2{}^{17}O)$) as shown in following equation:

$$\frac{dC_{tissue}(H_2O)}{dt} = k_1 CMRO_2 + CBF \cdot [k_2 C_{artery}(H_2O) - k_3 C_{vein}(H_2O)]$$, where k_1, k_2 and k_3 are physiological parameters which determine the changing rate of $H_2{}^{17}O$ content and are assumed to be constant. In the equation, the CBF is obtained from another scan with a bolus injection of $H_2{}^{17}O$. The $C_{artery/vein}(H_2{}^{17}O)$ is arterial input function obtained from animal study. $C_{tissue}(H_2{}^{17}O)$ is the NMR spectroscopy measurement.

The advantages of this method are: it gives the regional $CMRO_2$, ^{17}O is not radioactive and safe for human use, and the modeling is straightforward. But this method requires an accurate arterial input function, i.e. $C_{artery}(H_2{}^{17}O)$, which has been tried to be continuously measured on animals (Zhu *et al* 2005). On an animal, implanting a RF coil around the carotid artery is made to avoid frequent blood draw, but this technique is not yet applicable to humans. Another factor may affect the accuracy of $CMRO_2$ measurement is the physiological conversion factors, (e.g. k_1, k_2, k_3). Unlike PET, some of these assumptions can be measured or avoided by further simplifying the kinetic model. For example, the beginning of $^{17}O_2$ inhalation caused NMR peak is linearly proportional to $CMR^{17}O_2$ observed in tissue, while the washout phase is also solely associated with CBF. Then, $CMRO_2$ and CBF can be estimated by just one element differential

equation. However, these simplifications are still based on limited animal experimental data under anesthesia. Furthermore, one critical factor impacting the application of this technique is the high cost because $^{17}O_2$ is very expensive to synthesize. It costs a few thousand dollars for a small animal experiment, it will cost much more on human study.

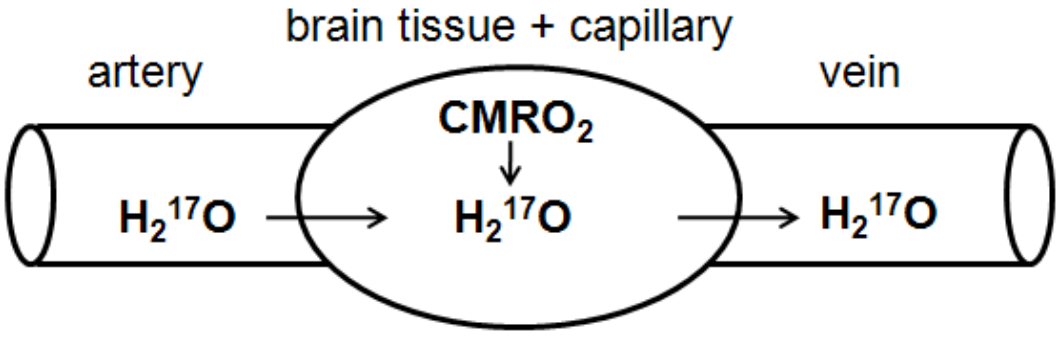

Figure 11 The model for $^{17}O_2$ NMR measuring $CMRO_2$.
$^{17}O_2$ is inhaled and delivered to the brain by artery. In the brain tissue, $^{17}O_2$ is reduced to $H_2{}^{17}O$ to produce ATP. The $H_2{}^{17}O$ is produced at the rate of $CMRO_2$ in the tissue and circulating in the blood stream. Because $^{17}O_2$ is not detectable in NMR, it does not appear in the model simplifying the computation.

2.2.3 NMR-^{13}C glucose

Alternatively, the $CMRO_2$ can be calculated by measuring the flux of TCA cycle using ^{13}C NMR. ^{13}C is stable and NMR visible. ^{13}C labeled metabolites can be identified in carbon spectroscopy. The areas under peaks in the spectrum are proportional to the concentrations. Infusing ^{13}C-1 labeled glucose would result an enrichment of ^{13}C-4 glutamate as a result of the TCA cycle. The time course of plasma glucose concentration and the peaks of ^{13}C-4 glutamate spectrum can be used to calculate the TCA cycle flux (Rothman *et al* 1992). Each molecule of glucose produces two pyruvate molecules and consumes six molecules of oxygen.

One cycle of TCA consumes one pyruvate molecule and uptakes three O_2 molecules. Thus $CMRO_2$ equals three times of TCA flux.

Although ^{13}C NMR gives unique metabolic measurements, this technique faces multitude of challenges including low abundance of ^{13}C, sensitivity of carbon spectrum affected by the coupling between C-H, localization of the spectrum signal, long acquisition time (e.g. 20-60 min) and various artifacts affecting the small signal (e.g. chemical shift, and RF coil sensitivity, etc.) (Gruetter NMR biomed 2006).

2.2.4 Calibrated fMRI

The functional MRI (fMRI) refers to the blood oxygen level dependent (BOLD) signal. The BOLD contrast originates in vasculature, more specifically, hemoglobin. As mentioned in 2.1.2.1, the conversion of oxygenated hemoglobin to deoxygenated hemoglobin changes hemoglobin from diamagnetic to paramagnetic. This change subsequently alters the R_2 and R_2^* relaxation of protons and creates BOLD signal contrast. The change of oxygen content in the blood is intrinsically caused by neural activity. The altered local magnetic field could extend beyond capillary to extravascular space to alter blood as well as tissue R_2 and R_2^* relaxation. The less O_2 the blood contains, the faster signals decay at transverse plane, and the higher R_2 and R_2^* are. So in the case that certain region of the brain is stimulated, local vasculature is able to sense the need of energy and cause hyperperfusion in that region. Due to the overcompensation

mechanism, more O_2 is provided than what is needed. Consequently, more oxygen molecules are dumped to the veins, rendering slower signal decay, smaller R_2/R_2^*, and therefore a higher BOLD signal. In summary, the evoked neural activities influence the vascular hemodynamic response, which causes the BOLD signals changes. Thus BOLD indicates neural activities through the vascular activities.

Davis et al (Davis *et al* 1998) proposed a model to describe these two components of BOLD signal and quantify $CMRO_2$ evoked by the neural stimuli. The model is simplified here as, $\delta BOLD = M \times f(CBF, CMRO_2)$, where M is a factor related to imaging parameters such as TE, B_0 and basal physiology such as CBV, Y; f is a function of CBF and $CMRO_2$. In the model, CBF change can be measured by MRI. M and $CMRO_2$ are two unknowns. This method is called calibrated fMRI because it requires an iso-$CMRO_2$ state changing the BOLD signal which is used to calibrate the vascular component of the BOLD signal, i.e. estimate the M. Hypercapnia challenge is used for this purpose, assuming that hypercapnia does not change $CMRO_2$. In a separate hypercapnia BOLD scan, CBF is measured together with BOLD, and BOLD signal change is determined only by CBF and M. The calculated M is then used for another funcitnoal task BOLD san estimating the detla $CMRO_2$ evoked by the neural stimulation.

This technique is limited to calculate $CMRO_2$ change by stimulation. The relative $CMRO_2$ change found by calibrated fMRI results in a much lower CBF

and $CMRO_2$ coupling ratio (i.e. CBF change versus $CMRO_2$ change) than that was previously reported by PET (Fox *et al* 1988; Hoge *et al* 1999). This discrepancy may due to the assumption that hypercapnia does not change $CMRO_2$, which might cause a biased estimation of the M factor. Other possibilities includes the accuracy of CBF measurement using arterial spin labeling (ASL) MRI, and some constants taken from literature, such as the ratio of blood volume and blood flow and coefficient of R_2 dependence on blood volume.

3 Developing the non-invasive MRI method for quantifying $CMRO_2$

3.1 Introduction of the method

As reviewed in chapter 1, cerebral metabolic rate of oxygen ($CMRO_2$) is an important marker for brain function and brain health. As reviewed in chapter 2, existing techniques for the quantification of $CMRO_2$ are under development for future research and clinical applications. I developed a non-invasive MRI method based on the Fick principle. This method applies phase-contrast MRI for quantitative cerebral blood flow (CBF) and T_2-Relaxation-Under-Spin-Tagging (TRUST) MRI for venous blood oxygenation (Y_v).

In this chapter, I include the sequence details of TRUST MRI and phase-contrast MRI, the quantification of Y_v at sagittal sinus (SS) and internal jugular vein (IJV) using TRUST MRI, optimizing phase contrast MRI for pulsative flow measurement, the *in vitro* blood experiment for calibrating the MR T_2 measurement to blood oxygenation, the technical improvement of the efficiency of TRUST MRI, and the reproducibility study for this $CMRO_2$ quantification method.

3.2 The TRUST MRI technique for quantifying Y

The T_2-relaxation-under-spin-tagging (TRUST) MRI is an intravascular R_2 based method. TRUST measures blood R_2 which is converted to Y through a calibration curve. This type of method was not yet applied on humans because the

partial volume effect within a voxel. The novelty of TRUST technique is that it applies arterial spin labeling (ASL) technique on the venous blood and subsequently separates the blood signal from the static tissue signal. In such way, the pure blood R_2 can be measured *in vivo*.

The TRUST sequence (Figure 12a) consists of interleaved acquisitions of label and control scans. The labeling slab is placed above the imaging slice to tag the venous blood drained by sagittal sinus (Figure 12b). In the label scan, the magnetization of the blood within the label slab is inverted to -1 by the 180° pulse, a process that is called spin tagging. During the period of inversion recovery (TI), the magnetization of tagged blood slowly recovers due to the T_1 relaxation. The image is acquired after TI of 1200ms, when the tagged magnetization is barely above zero based on that the blood T_1 is about 1624ms (Lu *et al* 2004). The thickness of the inversion pulse and the gap between tagging slab and imaging slice are designed as such that the tagged blood just flow through the imaging slice after TI. Therefore, the label scan has the image with tissue signal but suppressed blood signals. In the control scan, there is no inversion pulse applied, so the control image has both tissue and blood signals. The static tissue within the imaging slice experiences the pre-saturation pulse, so the tissue magnetization starts zero for each TR.

To produce T_2 weighted signal, TRUST MRI utilizes a non-slice selective τCPMG scheme (Figure 12a). The $R_2(=1/T_2)$ is measured by the T_2 weighted

signal decay obtained from four different echo times named effective echo times (eTE, here four eTEs are 0, 40, 80 and 160ms) to distinguish from the echo time (TE) between excitation and acquisition. The τCPMG T_2-preparation uses a 90° - 180° -90° scheme. The first 90° pulse flips the magnetization to the transverse plane and initiates T_2 relaxation. A series of 180° pulses refocus the out-phase spins and produce spin echoes. The second 90° pulse flips the transverse magnetization to longitudinal plane. Then, the T2 weighted magnetization along Z direction is ready for acquisition. The reason of using T_2-preparation rather than a slice selective T_2-refocusing pulse to produce T_2 weighting is to minimize the outflow effect on the T_2 measurement. The duration of T_2-preparation, eTE, is determined by the number of 180° pulses which are played with a uniform interval (here use 10ms). These 180° pulses are played in the fashion of composite pulses arranged in MLEV order to minimize the imperfection of RF pulses. To quantify the blood signal and tissue signal, the Bloch equations are used for simulating the magnetization one can acquire as follow:

Eq.3

$$S_{blood,label} = M_0 \cdot (1 - 2 \cdot e^{-(TI - eTE)/T_{1b}}) \cdot e^{-eTE \cdot R_{2b}} \cdot e^{-TE \cdot R_{2b}^*}$$

Eq.4

$$S_{blood,control} = M_0 \cdot e^{-eTE \cdot R_{2b}} \cdot e^{-TE \cdot R_{2b}^*}$$

Eq.5

$$S_{tissue,label} = S_{tissue,control} = M_0 \cdot (1 - e^{-(TI - eTE)/T_{1t}}) \cdot e^{-eTE \cdot R_{2t}} \cdot e^{-TE \cdot R_{2t}^*}$$

Where R_{1b}, R_{2b} and R_{2b}^* are R_1, R_2 and R_2^* of the blood; R_{1t}, R_{2t}, and R_{2t}^* are R_1, R_2 and R_2^* of the tissue.

The pure blood signal is $S_{control}$-S_{label}, since $S_{tissue,control} = S_{tissue,\ label}$, the subtraction only yields S_{blood} in the form of

Eq.6

$$S_{blood} = S_{control} - S_{label} = (S_{blood,control} + S_{tissue,control}) - (S_{blood,label} + S_{tissue,label})$$
$$= 2 \cdot M_0 \cdot e^{-(TI - eTE)\cdot R_{1b}} \cdot e^{-eTE \cdot R_{2b}} \cdot e^{-TE \cdot R_{2b}^*} = 2 \cdot M_0 \cdot e^{-TI \cdot R_{1b} - TE \cdot R_{2b}^*} \cdot e^{eTE(R_{1b} - R_{2b})}$$
$$= S_0 \cdot e^{eTE \cdot C}$$

In which $S_0 = 2 \cdot e^{-TI \cdot R_{1b} - TE \cdot R_{2b}^*}$ and $C = R_{1b} - R_{2b}$. R_{1b} ($0.6s^{-1}$) is much smaller than R_{2b} ($15s^{-1}$), so $C \approx R_{2b}$. The simulation shows that this approximation only affects R_{2b} by $0.1s^{-1}$. In such way, the blood signal is an exponential function of eTE.

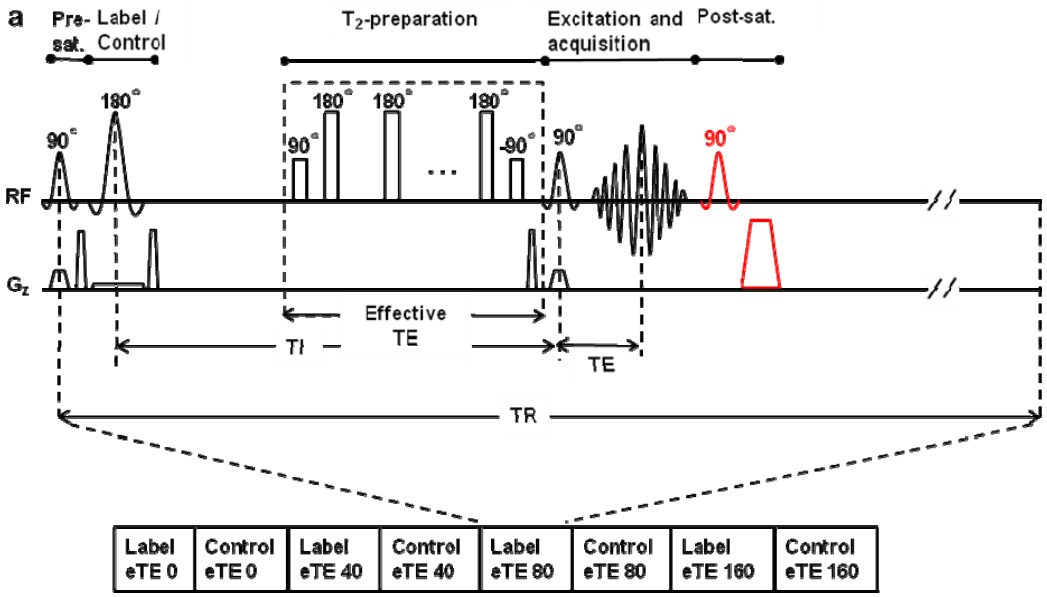

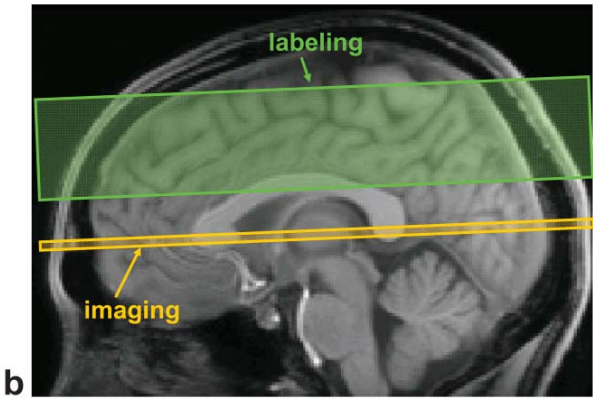

Figure 12 The T_2-relaxation-under-spin-tagging (TRUST) MRI sequence.
a) Pulse sequence diagram for TRUST MRI. The sequence consists of interleaved acquisitions of label and control scans, and each image type is acquired with four different effective echo times (eTEs) ranging from 0 to 160ms. For each scan, the sequence starts with a pre-saturation radiofrequency (RF) pulse to suppress the static tissue signal, followed by a labeling (or control) RF pulse to magnetically label the incoming blood. A brief waiting period (1.2sec) is allowed for blood to flow into the imaging slice. Before data acquisition, a nonselective T_2-preparation pulse train is applied to achieve the T_2-weighting, the duration of which is denoted eTE. The T_2 preparation scheme, instead of conventional T_2-weighted sequence, is used to minimize the blood outflow effect. b) Geometric relationship between the imaging slice (yellow) and labeling slab (green). (copied from Lu and Ge 2008).

The Y can be quantified based on the measured R_{2b} through a calibration curve. Then, OEF can be estimated by Y_a-Y_v.

3.3 Phase contrast MRI for quantifying CBF

CBF can be estimated by phase-contrast MRI or arterial-spin-labeling (ASL) MRI. In this study, I chose to use phase-contrast MRI for CBF quantification for two reasons: 1. Phase-contrast MRI in the feeding arteries can provide an estimation of the whole brain blood flow, which is in line with the whole brain Y_v estimation using TRUST MRI in large draining veins (e.g. sagittal sinus, internal jugular veins). 2. While ASL MRI can assess spatial distributions

of blood flow to the brain, the CBF quantification via ASL is less straightforward and is often dependent on transit time, labeling efficiency and trailing time (Alsop and Detre 1996; Buxton *et al* 1998; Hendrikse *et al* 2003; Yang *et al* 2000). Phase-contrast has been widely used for angiogram and quantitative flow measurements (Haacke *et al* 1999).

Phase contrast (PC) MRI measures flow velocity by utilizing magnetization phase change due to the application of magnetic field gradient. PC MRI is a typical gradient-echo sequence except that a bipolar gradient is inserted before the data acquisition to encode the velocity (Figure 13). The movement of spins yields a phase change after experiencing a pair of balanced bipolar magnetic gradient, but static spins cancel out the effects of two gradients on the phase. The amount of phase change is proportional to the velocity for given gradient. The following diagram shows the sequence.

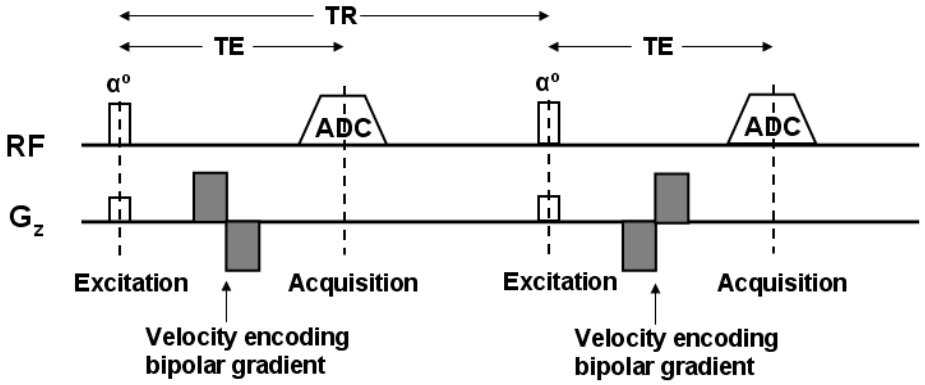

Figure 13 The phase-contrast MRI pulse sequence.
Two successive TR periods are shown. The only difference between the two periods is the sign of the velocity encoding gradient. This paired scheme is used so that a subtraction would remove any spurious phases due to field inhomogeneity and eddy current.

Assuming a base phase of ϕ_0 for the magnetization, the addition of one lobe of gradient would result in a phase of $\phi = \gamma \cdot G \cdot z_1 \cdot t + \phi_0$, where γ is the gyromagnetic ratio, G is the magnitude of the gradient, z_1 is the coordinate of the spin along z direction at this time, t is the duration of the lobe, ϕ_0 is the base phase due to field inhomogeneity, eddy current and other factors. The second gradient is applied with an opposite direction; therefore the phase has a negative sign. The phase becomes

Eq.7

$$\phi_a = \gamma \cdot G \cdot z_1 \cdot t - \gamma \cdot G \cdot z_2 \cdot t + \phi_0 = \gamma \cdot G \cdot (z_1 - z_2) \cdot t + \phi_0 = -\gamma \cdot G \cdot v \cdot t \cdot t + \phi_0$$
$$= -\gamma \cdot G \cdot v \cdot t^2 + \phi_0$$

The v is the flow velocity, and the spins move along z direction. During the next TR period, the order of the gradients is reversed. Thus the phase for the second TR is

Eq.8

$$\phi_b = \gamma \cdot G \cdot v \cdot t^2 + \phi_0 .$$

Taking the subtraction between ϕ_a and ϕ_b will remove the ϕ_0 effect, yielding a phase value that is solely dependent on the flow velocity $\Delta\phi = 2\gamma \cdot G \cdot v \cdot t^2$, from which the velocity map within the vessel can be calculated. Integrating the velocity inside the vessel of interest will give the CBF (in ml blood/min) for this vessel. Note that, although the measurement of velocity is sensitive to the orientation of the slice (ideally perpendicular), the CBF is

relatively insensitive to the orientation because the area of the cross-section (A) will cancel the angle effect:

Eq.9

$$CBF_{measured} = v_{measured} \cdot A_{measured} = v_{true} \cdot \sin(\theta) \cdot A_{true} / \sin(\theta) = v_{true} \cdot A_{true} = CBF_{true}.$$

3.4 Implement the TRUST MRI and phase-contrast MRI for measuring $CMRO_2$

3.4.1 The MRI experiment

MR experiments were performed on a 3 Tesla MRI systems (Philips Medical Systems, Best, the Netherlands). The protocol was approved by Institutional Review Board of our University and informed written consent was obtained for each participant. A total of 36 healthy subjects (16 female, 20 male, age 42±20 years) participated in this study. Five subjects were used in the comparison of gated and non-gated phase-contrast MRI. In seventeen subjects, $CMRO_2$ was estimated using both sagittal sinus and internal jugular vein TRUST MRI. In the remaining fourteen subjects, only sagittal sinus TRUST MRI was used in $CMRO_2$ estimation. The body coil was used for RF transmission and an 8-channel SENSE head coil was used for receiving. Foam padding was used to stabilize the head to minimize motion. The subjects were instructed not to fall asleep during the experiments, and this was verified after each block of scans, because CBF and venous oxygenation may change during sleep (Bangash *et al* 2008).

Venous oxygenation levels of two major draining veins, sagittal sinus (SS) and internal jugular vein (IJV), were studied. The Y_v values and the estimation accuracy between these two venous locations were compared to determine the optimal location with most accurate estimation and minimum scan time. TRUST MRI on SS was performed with the following parameters: single-shot EPI, axial plane, voxel size = 3.44x3.44x5mm^3, field of view (FOV) = 220x220x5mm^3, repetition time (TR) = 8000ms, echo time (TE) = 19ms, inversion time (TI) = 1200ms, tagging slab thickness = 80mm, gap between imaging slab and tagging slab = 20mm, four different T_2-weightings with eTE of 0ms, 40ms, 80ms and 160ms, corresponding to 0, 4, 8 and 16 refocusing pulses in the T2-preparation (τ_{CPMG}=10 ms). For each eTE, four pairs of tag and control images were acquired to improve signal-to-noise ratio (SNR). The total scan time of SS TRUST MRI is 4 minutes and 16 seconds. TRUST MRI on IJV used similar parameters except for the following: two-shot EPI, voxel size = 2x2x10mm^3, FOV = 160x160mm^2, tagging thickness = 170mm, gap = 10mm, three different T_2-weightings with eTE of 0ms, 40ms and 80ms. Compared to the SS TRUST MRI, the spatial resolution was slightly increased to allow the separation of IJV from several other vessels in the neck regions (e.g external jugular veins, venous plexuses, internal and external carotid arteries). To reduce EPI-related image distortions under high resolution, two-shot EPI was used. Consequently, the scan duration of IJV TRUST MRI was

increased to 6 minutes and 24 seconds despite the reduction of eTE number from 4 to 3.

TRUST MRI planning for SS was based on middle sagittal survey image (Figure 14a). It is relatively straightforward to identify the SS along the posterior boundary of occipital lobe located between brain and skull. The SS TRUST imaging slice is oriented axially intersecting the SS at about 1 cm above the sinus congruence where the SS, straight sinus and transverse sinus join. The tagging slab is chosen to tag all the venous blood upstream of the imaging location. For scan planning of IJV, a time-of-flight (TOF) venogram was found necessary in order to reproducibly position the slices. The TOF venogram covered the sigmoid sinus as well as the upper part of the IJV with the following parameters: TR/TE/flip angle=23ms/3.45ms/18°, FOV=160x70x160mm^3, voxel size 1.0x1.0x1.5mm^3, number of slices =47, one saturation slab of 60mm positioned below the imaging slab, duration 1 min 26 sec. Based on the sagittal and coronal views of maximum intensity projection (MIP) of the venogram (Figure 14b), imaging slice of TRUST MRI was positioned to cover the IJV immediately below the jugular bulb, where the vein exits the cranial cavity.

For phase-contrast MRI, non-gated and cardiac-gated implementations were compared to determine the optimal sequence. Non-gated phase-contrast MRI is relatively short in scan duration but the image tends to have cardiac pulsation artifacts. The gated sequence can provide artifact-free velocity maps at different

cardiac phases, but takes much longer time. For both gated and non-gated scans, the following parameters were used: single slice, voxel size = 0.45x0.45x5 mm^3, FOV = 230x230x5 mm^3, maximum velocity encoding = 80 cm/s. The non-gated scan results in one phase-contrast image with scan duration of 30 seconds. The gated scan results in 15 images at different cardiac phases with scan duration around 5 minutes and 30 seconds depending on subject's heart rate. The positioning of the phase-contrast scan was based on a TOF angiogram (acquired with similar parameters as the venogram described above except for opposite location of saturation slab) and the slice was oriented perpendicular to the internal carotid and vertebral arteries (Figure 14c).

In addition, a T1-weighted MPRAGE image (voxel size 1x1x1 mm^3) was acquired to provide an estimation of the intracranial volume, so that blood flow per unit mass of tissue can be calculated, which accounts for the variances in brain sizes across subjects.

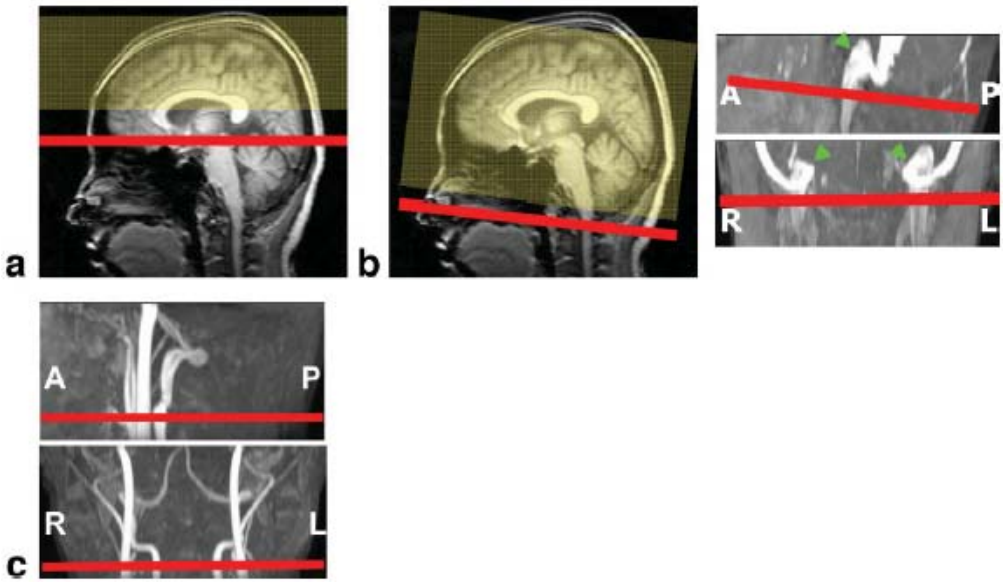

Figure 14 The imaging slice positions for the scans in the $CMRO_2$ measurements.
(a) Venous oxygenation was measured at the sagittal sinus (SS) via TRUST MRI imaging slice in red, while the upstream of SS to the imaging slice was tagged in yellow. (b) The planning of TRUST MRI at the internal jugular vein (IJV) was based on a mid-sagittal survey image (left) and a venogram (right), and the imaging slice was positioned immediately below the jugular bulb (green arrows). (c) Phase-contrast MRI was planned on an angiogram and the slice orientation was perpendicular to internal carotid and vertebral arteries.

3.4.2 Data analysis

Data were processed using in-house MATLAB (Mathworks, Natick, MA) scripts. The data processing procedures for TRUST MRI are based on an algorithm described previously (Lu and Ge 2008b). Briefly, after pair-wise subtraction between control and tag images, a preliminary ROI was manually drawn to include the target veins. This ROI tends to have about 30-50 voxels which include the veins as well as some surrounding tissue. To further define the venous voxels, the voxels with highest blood signals (according to the difference signals) in the ROI were chosen as the final mask for spatial averaging (Figure

15a). For the purpose of standardizing protocol, I used 4 voxels for SS and 10 voxels for IJVs, although I have tested the effect of voxel number and found that the results are relatively insensitive to the number (Lu and Ge 2008b). The number of voxels used was greater in the IJV scan because the scan has smaller voxel size. This way the total area included is comparable to that in the SS scan. The venous blood signals were fitted to a mono-exponential function to obtain T2 (Figure 15b). The T_2 was in turn converted to Y_v via a calibration plot obtained by in vitro bovine blood experiments under controlled oxygenation, temperature and hematocrit conditions (Lu *et al* 2004; Zhao *et al* 2007). In addition, the standard error (SE) of the estimated parameters was calculated based on a goodness-of-fit procedure (Matlab routine nlparci.m).

For phase-contrast MRI data, a preliminary ROI was drawn on each of the four arteries (left and right internal carotid arteries, left and right vertebral arteries) based on the magnitude image. A signal intensity threshold was then applied to the magnitude image to obtain the final vessel mask. For non-gated phase-contrast image, the threshold was set to be 5 times the background noise. For the gated scan, threshold was applied on each of the cardiac phases and the threshold value was reduced to 3.5 times the noise, in order to account for the lower SNR in the gated scan. This mask was applied to the phase image (velocity map) (Figure 16) to yield the whole brain blood flow. The unit volume CBF (in ml/100g/min) was then obtained by normalizing the total CBF to the intracranial volume, which was

estimated from the high resolution T1 weighted image using FSL (FMRIB Software Library, Oxford University) functions (BET, FLIRT, BETSURF).

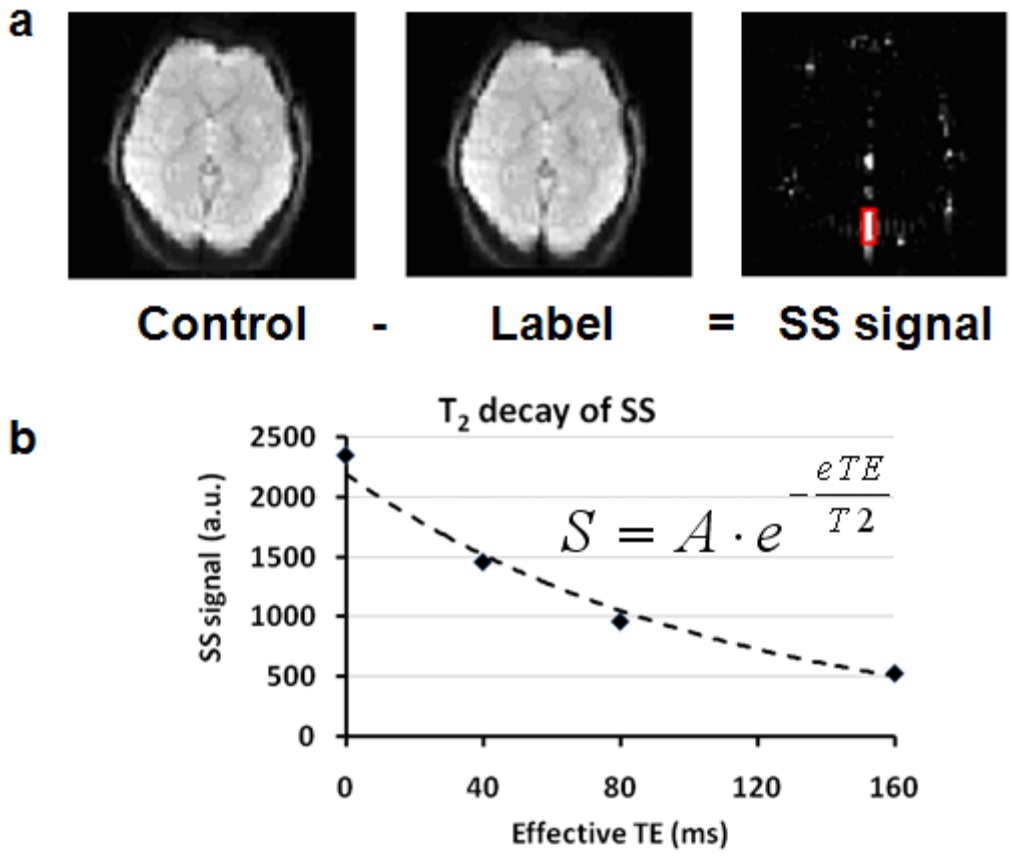

Figure 15 The illustration of the TRUST MRI processing.
(a) Subtracting the label images of TRUST from the control images of TRUST MRI yields the sagittal sinus (SS) blood signals. (b) The SS signals are fitted as a function of effective TE using the Bloch equation in the simulation.

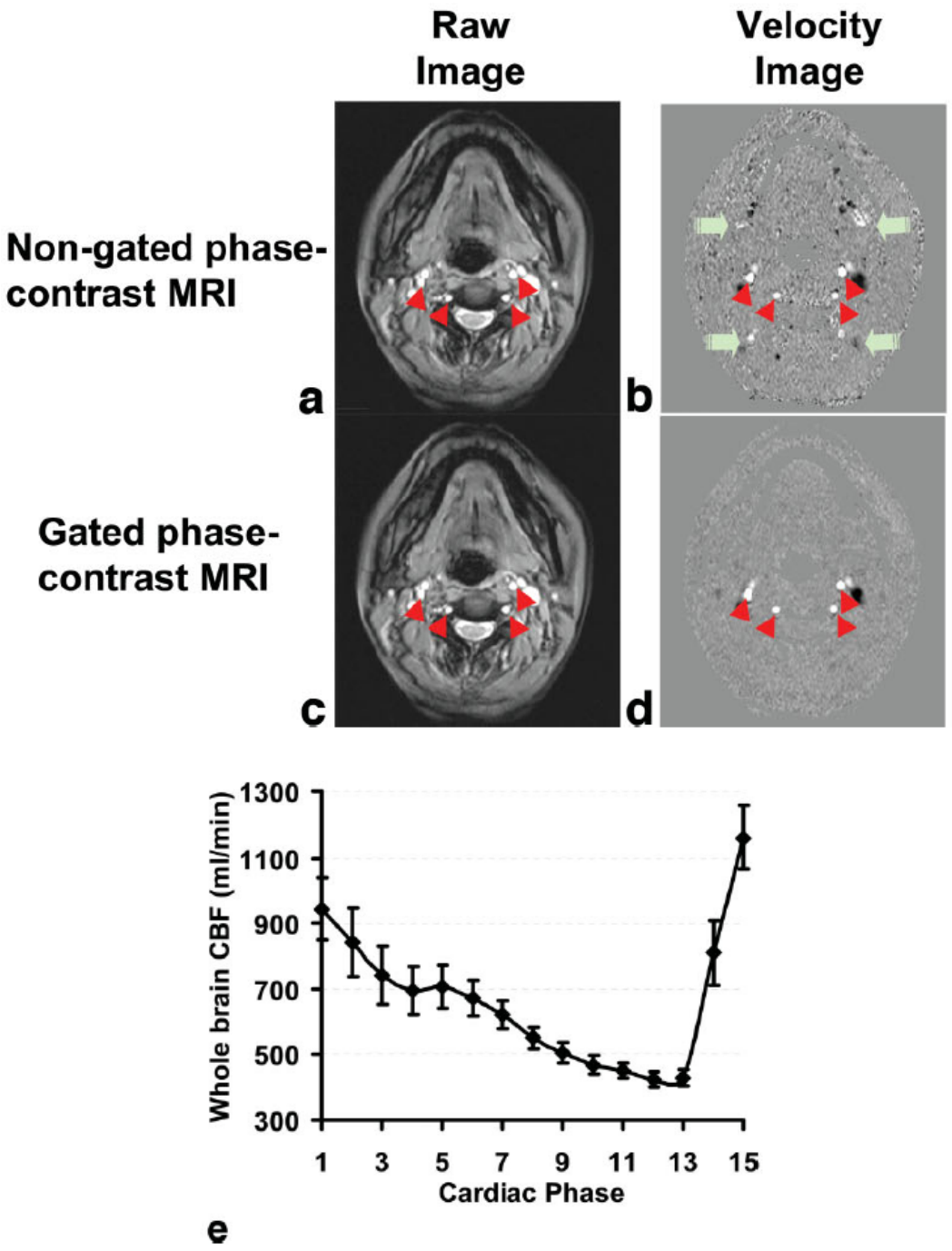

Figure 16 The comparison of gated and non-gated phased-contrast MRI.
The raw images (a and c) of these two sequences are similar. However, the velocity map (b) of the non-gated scan shows some ghosting artifacts (green arrows) along the phase-encoding direction (anterior-posterior), due to flow pulsation in large vessels. Red arrowheads indicate the internal

carotid and vertebral arteries. (e) Whole brain CBF (summation of internal carotid and vertebral arteries) at different cardiac phases during a heart beat (n=5). The averaged value of all the cardiac phases is comparable the non-gated value (p=0.53). The R-R interval was evenly divided into 15 phases. Error bars indicate the standard errors of mean.

3.4.3 Results

Figure 16b and d show the velocity maps for non-gated and gated phase-contrast scan, respectively. Cardiac-pulsation-induced ghosting can be seen in the non-gated image (green arrows), whereas the gated image is free to these artifacts. There is a clear fluctuation of whole-brain CBF within the cardiac cycle (Figure 16e). The averaged whole brain flow was 662±118 ml/min (mean±SD, n=5), which is not significantly different from the values, 679±73 ml/min, using the non-gated scan (paired t test, p=0.53). Therefore, given the considerable difference in scan duration (5.5 min and 0.5 min for gated and non-gated scan, respectively), the non-gated phase-contrast sequence was used in all other experiments.

Results of SS and IJV TRUST MRI are illustrated in Figure 17. The control (Figure 17a and d) and tag (Figure 17b and e) images are almost identical and the locations of the veins are not obvious. Subtraction between these images highlighted the venous blood signal shown as bright voxels in the difference images (Figure 17c and f), suggesting an effective tagging of the targeted vessels in both SS and IJV scans. The Y_v in SS and IJV were found to be 62.8±5.3% (n=17) and 64.6±5.4%, respectively. Inter-subject variations in Y_v values are seen in both SS and IJV data, and furthermore the Y_v in SS and IJV shows a significant

correlation (cc=0.71, p= 0.0015) (Figure 17g). The standard errors of Y_v estimations were 1.6±0.9% and 1.6±0.9% for SS and IJV, respectively. These estimation errors show no significant difference between the two venous locations (p=0.95), suggesting that the estimation accuracy are comparable between the SS and IJV TRUST scans. No difference was observed between Y_v in SS and IJV (paired t-test, p=0.09). I considered that the IJV TRUST MRI requires a longer scan duration compared to SS TRUST and also needs a venogram as a localizer, all together taking approximately 9 minutes, which is twice the duration of the SS TRUST scan. Thus, SS TRUST MRI was used in all later experiments.

Combining the phase-contrast MRI and TRUST MRI measurements and utilizing in chapter 2.1.1, whole brain averaged $CMRO_2$ was estimated. Table 1 summarizes the $CMRO_2$ results. The estimated $CMRO_2$ values are in good agreement with previous PET studies (Table 2).

Given the different brain physiology that CBF, Y_v (i.e. OEF) and $CMRO_2$ represent, it would be of interest to examine whether they have intrinsic correlations across subjects. Experiments were therefore performed in additional subjects and the scatter plot of these parameters were studied (Figure 18). It can be seen that the blood flow and venous oxygenation are highly correlated (cc=0.65, p<0.0001, Figure 18a) across subjects, and that subjects with higher blood flow tend to have higher Y_v. Similarly, CBF and $CMRO_2$ also showed a trend of positive correlation (cc=0.41, p=0.0222, Figure 18b), although the level

of statistical significance is lower. No correlation was observed between Y_v and $CMRO_2$.

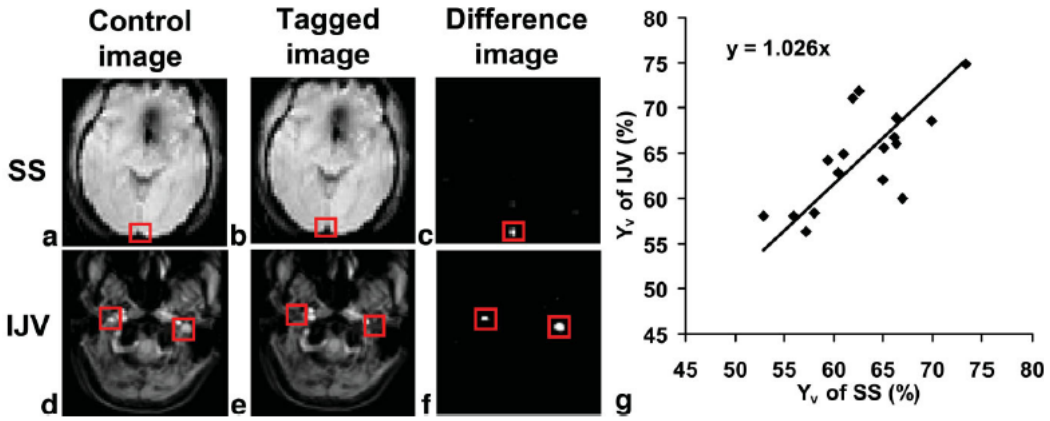

Figure 17 The results of TRUST MRI at the sagittal sinus (SS) and the internal jugular vein (IJV).
The control (a and d) and tagged (b and e) images appear similar, while the different images (c and f) show clear delineation of the tagged vessels. The red boxes illustrate the manually drawn ROI for quantitative analysis. (g) Correlation between estimated venous oxygenation in SS and in IJV (n=17). A significant correlation (cc=0.71, p=0.0015) was found between them. The line is the fitting of the data to y=ax.

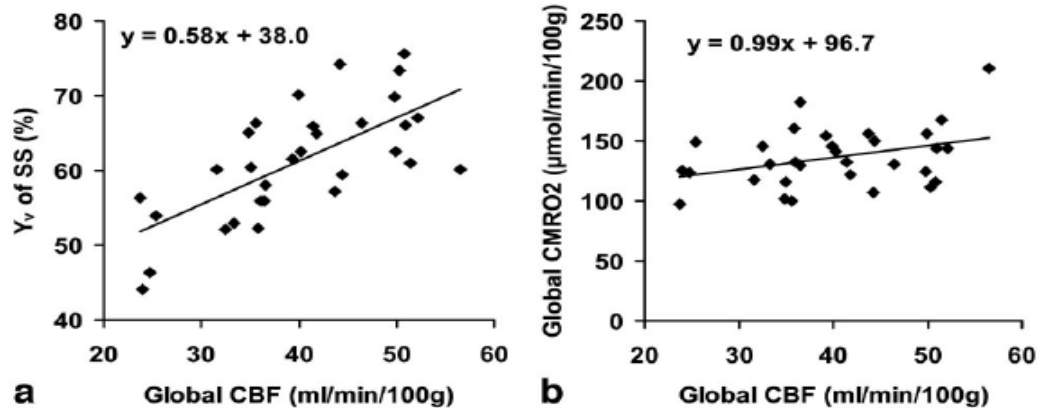

Figure 18 The correlation between different physiologic parameters across subjects.
(a) Scatter plot between global CBF and venous oxygenation (n=31, cc=0.65, p<0.0001). Each dot in the plot represents data from one subject. It can be seen that individual with higher blood flow tends to have higher venous oxygenation, which corresponds to lower oxygen extraction fraction.

The line indicates the linear fitting of the data. (b) Scatter plot between global CBF and $CMRO_2$. A weak correlation (cc=0.41, p=0.0222) is observed.

$CMRO_2$ using Y_v in SS (μmol/min/100g)	Global CBF (ml/min/100g)	Intracranial Volume (ml)
167.3±34.1	59.1±9.0	1608.1±175.3

Table 1 Summary of results for $CMRO_2$ measurement (mean±SD, n=43).

Study	$CMRO_2$ value* (μmol/min/100g)	Subject age (years)	Number of subjects
(Mintun *et al* 1984)	131 (95-201)	23-40	5
(Powers *et al* 1985)	130 (63-219)	18-84	24
(Fox *et al* 1988)	150	19-26	5
(Perlmutter *et al* 1987)	118 (109-134)	20-84	32
(Ishii *et al* 1996)	157 (143-184)$^{\Delta}$	42-73	15
(Hattori *et al* 2004)	127 (105-171)	21-46	16
(Ito *et al* 2005)	139	n/a	70
(Coles *et al* 2006)	125	18-60	10
(Ibaraki *et al* 2008)	147 (114-181))$^{\Delta}$	21-24	8
(Hayashi *et al* 2008)	147	40-69	16

* - values in the parenthesis are ranges across subjects/brain regions.
Δ - gray matter values.

Table 2 A review of literature $CMRO_2$ values in normal subjects.

3.4.4 Discussion

This study presents an MRI approach to quantify absolute cerebral metabolic rate of oxygen (in units of μmol O_2/100g brain/min) in humans. The main advantages of the proposed method are that it is completely non-invasive and can be performed with duration of 5-10 minutes on a standard clinical scanner.

To our knowledge, this is the first approach to assess $CMRO_2$ without any exogenous agents (e.g. radioactive tracers in PET (Mintun *et al* 1984), ^{13}C (Hyder *et al* 1996), ^{17}O tracers (Zhu *et al* 2002) or Gd-DTPA contrast agent (An *et al* 2001) in MRI). The whole-brain averaged $CMRO_2$ values were 167.3±34.1 μmol/100g/min, in relative good agreement with literature reports using PET. Although the MRI measured $CMRO_2$ value is slightly higher than some reports from PET, this discrepancy is due to the CSF related partial volume effect of PET. The limit of spatial resolution of PET overestimates the tissue volume, rendering a lower $CMRO_2$ value. Unlike PET, this MRI technique measures pure tissue $CMRO_2$. This measurement was achieved using a quantitative phase-contrast flow measurement in combination with a recently developed venous oxygenation technique (Lu and Ge 2008b).

Because the accuracy of the $CMRO_2$ estimation is critically dependent on the validity of the individual MRI measurements, each of the MR techniques was assessed in terms of optimal acquisition strategies. The gated and non-gated phase-contrast MRI were compared for the flow quantification, and it was found that the non-gated scan can provide an estimation of total blood flow similar to that using the gated scan. This result is consistent with the finding from a previous study, which showed a difference of 3% between the two techniques (Spilt *et al* 2002). Considering a >10 fold difference in scan duration (30s vs. 5.5 minutes), I recommend the non-gated phase-contrast scan for future studies. TRUST MRI in

SS and IJV demonstrated that the blood oxygenation in SS and IJV are highly correlated across subjects. This is expected because the general venous flow trajectory is from venous sinuses to jugular veins (although some venous blood in sinuses leaves the intracranial space via venous plexuses and dural emissary veins (Moore and Dalley 1999). The estimation accuracy as assessed by standard errors is comparable for both methods. The estimation accuracy is also relatively insensitive to the spatial gap between imaging slice and labeling slab. I have compared Y_v in SS TRUST using gaps of 10, 15, 20mm, and found virtually identical values. Since the IJV measurement takes about twice the time of the SS scan (see Methods and Results for details), I recommend the SS Y_v measurements for future studies. Therefore, our current protocol takes about 7 minutes for the whole-brain $CMRO_2$ measurement which includes the following MR sequences: TOF angiogram (2 minutes), SS TRUST MRI (4.5 minutes), non-gated phase-contrast MRI (0.5 minute).

Scan duration of seven minutes is still considered a relatively long time in a clinical study. In order to further reduce the time for the $CMRO_2$ measurement, several strategies can be used. First, the TOF angiogram is only used for localization of the feeding arteries and positioning of the phase-contrast MRI, but is not used in the actual calculation of $CMRO_2$. Thus, if one can use alternative anatomic landmarks such as vertebral bones or magnum foramen for the positioning of the phase-contrast scan, the angiogram can be omitted and the scan

duration can be shortened by two minutes. However, this requires the MR operator to be quite familiar with the anatomic structures in the neck region. A second strategy to reduce the duration is to shorten the time for TRUST MRI. In the present protocol, TRUST MRI takes 4 minutes and 16 seconds which acquires four eTE weightings with each eTE having four repetitions. Therefore, one can reduce the number of eTEs and/or the number of repetitions. However, this is achieved at the cost of reducing estimation accuracy. I have performed analysis to investigate the dependence of estimation errors on repetition number and eTE number. I found that the reduction of repetition number and eTE number reduces the estimation accuracy in a similar manner. Thus, I grouped them together and plotted the estimation error as a function of scan duration (TR x repetition number x eTE number x 2) (Figure 19). It can be seen that the relationship between estimation error and the TRUST scan duration is not linear. The optimal protocol for each study should be based on how much scan time is available and what the acceptable estimation error is.

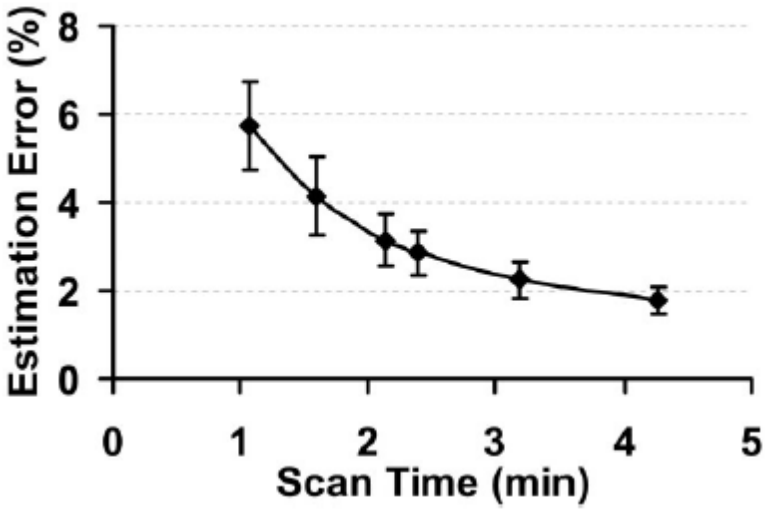

Figure 19 The TRUST MRI measurement accuracy as a function of scan duration.
The measurement accuracy is quantified by the estimation error from the goodness-of-fit analysis.

The present study utilized the effect of deoxyhemoglobin on blood T_2 to estimate the venous oxygenation, a principle used be several previous studies (Oja *et al* 1999; Wright *et al* 1991). It should be noted that blood oxygenation can also be estimated based on the phase of blood magnetization, as demonstrated by Haacke et al. (Golay *et al* 2001; Haacke *et al* 1997) and Fernandez-Seara et al. (Fernandez-Seara *et al* 2006). In addition, based on theoretical framework developed by Yablonskiy and colleagues (Yablonskiy and Haacke 1994), An et al. (An and Lin 2003) and He et al. (He and Yablonskiy 2007; He *et al* 2008) have shown that the effect of deoxyhemoglobin on extravascular tissue can be used for quantification of venous oxygenation. These approaches also have the potential to be used for quantitative estimation for $CMRO_2$.

The proposed technique has a few limitations. First, the method only measures whole brain $CMRO_2$ but not a map of $CMRO_2$. Thus, it cannot provide regional $CMRO_2$ information. As a result, this technique will have limited utility in brain diseases with focal metabolic changes, such as acute stroke and brain tumor, unless the lesion regions cover the majority of the brain. To achieve spatially specific $CMRO_2$ measurement, one would need mapping techniques for both CBF and Y_v. CBF map can be obtained with arterial spin labeling MRI. For Y_v, however, robust mapping measurement is still challenging. The TRUST method can be potentially applied to small veins or venules to estimate local Y_v. However, one would need to develop a method to label the tissue and wait for the labeled spin to enter the venules, where its R_2 is determined. In this regard, tissue-based techniques, such as the ones used by An et al. (An and Lin 2003) and He et al. (He and Yablonskiy 2007; He *et al* 2008), may have an advantage if the biophysical model used can be shown to be applicable for all vessel sizes and orientations. Alternatively, ^{17}O-based spectroscopy method may also prove to be valuable if the cost of ^{17}O can be considerably reduced (Zhu *et al* 2002). Second, the effect of hematocrit (Hct) variations is not considered in this study. Hct will affect the estimation of Y_a-Y_v and C_h in Eq.1. The calculation used in this study was based on Hct level of 0.44. If the actual Hct is higher than 0.44, Y_a-Y_v will be over-estimated, while C_h will be under-estimated (see Appendix for details). Numerical simulations were performed to assess the effect of Hct variations on

the estimated $CMRO_2$ values. In the estimation of $CMRO_2$ in Eq. 1, the value of Hct is needed for the determination of two parameters. First, C_h is linearly dependent on Hct, as more hemoglobin means a greater oxygen-carrying capacity of the blood (the amount of oxygen dissolved in the blood is negligible). Second, the calibration plot to convert blood R_2 into Y_v is affected by Hct. That is, the blood R_2 is dependent on both Y_v and Hct. Such a dependence has been established previously for 1.5T (Stefanovic and Pike 2004; Wright *et al* 1991) and 4.7T (Silvennoinen *et al* 2003), and more recently for 3T (Zhao *et al* 2007). Typical Hct values for normal subjects are within the range of 0.38 to 0.50 (Chanarin *et al* 1984). In the present study, I did not perform blood sampling to measure Hct on a subject-by-subject basis. Instead, the Hct was assumed to be 0.44 for all subjects. Therefore, it is important to estimate the error in $CMRO_2$ when the true Hct is different from the assumed value.

The simulations start with a set of assumptions on true parameter values: Y_a=100%, Y_v=61.5%, CBF=48.3ml/100g/min, oxygen-carrying capacity of 1 gram of hemoglobin=55.6 μmol of oxygen. Hct varies from 0.38 to 0.50 at an interval of 0.01. For each Hct value, the true $CMRO_2$ was calculated using Eq.1. The venous blood R_2 was also calculated using the Hct-specific coefficients established by Zhao et al. (Zhao *et al* 2007). These simulated data were then processed using our standard data processing strategies, in which Hct was always assumed to be 0.44. The estimated Y_a-Y_v, C_h, and $CMRO_2$ was computed and

compared to the true values. Figure 20 plots the bias caused by the incorrect assumption of Hct value. It can be seen that the terms Y_a-Y_v and C_h are biased in the opposite directions and their effects on $CMRO_2$ were partly cancelled out. As a result, the bias in $CMRO_2$ is mild. To correct for this bias, one can measure the Hct of each individual by blood sampling.

Finally, the proposed technique has not been validated with a gold standard method. While the estimated values are in good agreement with previous reports using radioactive tracers, each of the experimental measures in our MR method needs to be validated in order for this method to be routinely used in clinical settings. The flow measurement may be compared to perfusion-CT or Doppler techniques. The oxygenation measurement can be validated by blood sampling from the jugular vein. Alternatively, the entire method can be validated with respective PET techniques (e.g. ^{15}O-labled H_2O for flow, ^{15}O-labeled O_2 for oxygen extraction fraction). These studies shall be the subject of future investigations.

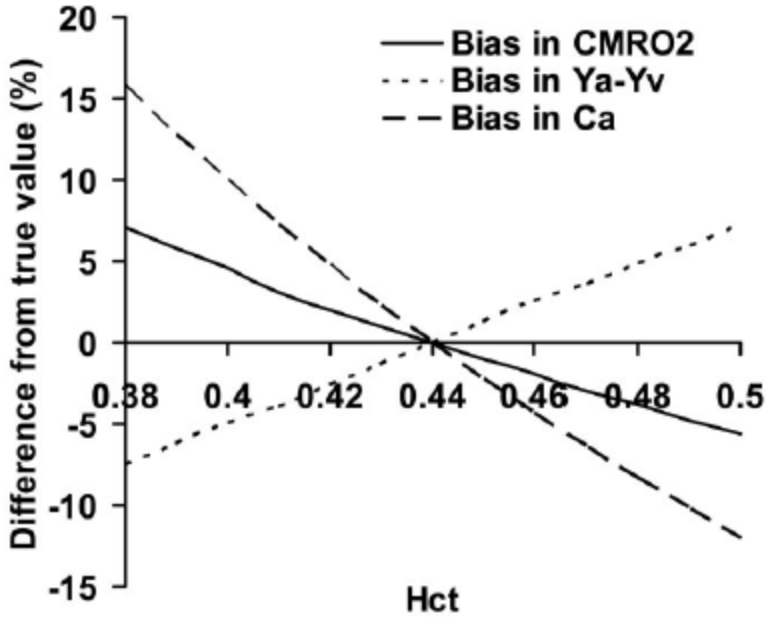

Figure 20 The simulation of the effect of hematocrit (Hct) on biased Y_v estimation.
Variations in Hct cause biases in the estimated Y_a-Y_v and C_a. These two effects are opposite in directions. Thus, the bias in the estimated $CMRO_2$ is smaller in amplitude. All values are shown in relative changes, i.e. (estimated value-true value)/true value x 100%.

3.5 Calibrating the blood R_2 (or T_2) to the blood oxygenation (Y)

3.5.1 The intravascular R_2 (or T_2) is Y and Hct dependent

As discussed in the last section, the blood T_2/R_2 is also related to the hematocrit (Hct) in addition to Y. The blood is mainly composed of plasma and erythrocytes which is also known as red blood cells. The Hct represents the volume fraction of erythrocytes. In the last study, the Y was directly converted from blood R_2 by using an assumed Hct. To count the Hct effect, the blood R_2 is modeled as a function of both Y and Hct, meaning that blood R_2 relaxation is affected by the amount of deoxyhemoglobin (dHb) present in the blood which is determined by both Hct and Y (Hct x (1-Y)). The machemism of dHb altering

blood R_2 relaxation rate is complicated, which is conceptually explained in chapter 2.1.2.1. The water-exchange model has been used to explain the effect of Hct and Y on blood R_2. Van Zijl and Golay extended this model to different different compartments of the blood, i.e. plasma, diamagnetic part of erythrocyte and paramagnetic part of erythrocyte whose susceptibility depends on oxygenation (Golay *et al* 2001; van Zijl *et al* 1998). Specifically according to Equations [3-6] in Golay et al. (Golay *et al* 2001), blood R_2 can be written as:

Eq.10

$$R_2 = \frac{1}{T_2} = R_{2,0} + Hct \cdot (1 - Hct) \cdot (\Delta\omega)^2 \cdot \tau \left[1 - \frac{2\tau}{\tau_{CPMG}} \tanh\left(\frac{\tau_{CPMG}}{2\tau} \right) \right]$$

where

Eq.11

$$R_{2,0} = R_{2,plas} + Hct \cdot (R_{2,ery} - R_{2,plas})$$

and R_2, $R_{2,plas}$ and $R_{2,ery}$ are transverse relaxation rates of blood, plasma and erythrocytes, respectively. $\Delta\omega$ is the larmor frequency shift of erythrocyte. $R_{2,ery}$ can in turn be written as:

Eq.12

$$R_{2,ery} = R_{2,plas} + R_{2,dia} + R_{2,oxy} + (1 - Y)(R_{2,deoxy} - R_{2,oxy})$$

Applying Eq.12 in Eq.11, one can write:

Eq.13

$$R_{2,0} = R_{2,plas} + Hct \cdot [R_{2,dia} + R_{2,oxy} + (1 - Y)(R_{2,deoxy} - R_{2,oxy})]$$

The term $\Delta\omega$ in Eq.10 can be expanded as:

Eq.14

$$\Delta\omega = \omega_{dia} + \omega_{oxy} + (1-Y)(\omega_{deoxy} - \omega_{oxy})$$

Furthermore, the term $\tau\left[1 - \frac{2\tau}{\tau_{CPMG}}\tanh\left(\frac{\tau_{CPMG}}{2\tau}\right)\right]$ in Equation Eq.10 is not dependent on Y or Hct, thus can be treated as a constant. We therefore define:

Eq.15

$$\mu = \tau\left[1 - \frac{2\tau}{\tau_{CPMG}}\tanh\left(\frac{\tau_{CPMG}}{2\tau}\right)\right]$$

Then, applying Eq.11-Eq.15 in Eq.10, we have:

Eq.16

$$R_2 = \frac{1}{T_2} = R_{2,plas} + Hct\cdot[R_{2,dia} + R_{2,oxy} + (1-Y)(R_{2,deoxy} - R_{2,oxy})] + Hct\cdot(1-Hct)\cdot[\omega_{dia} + \omega_{oxy} + (1-Y)(\omega_{deoxy} - \omega_{oxy})]^2\cdot\mu$$

Rearranging Eq.16 in terms of (1-Y) and Hct, one can readily write:

Eq.17

$$R_2 = \frac{1}{T_2} = A + B\cdot(1-Y) + C\cdot(1-Y)^2$$

where *A*, *B* and *C* are in turn dependent on Hct by:

Eq.18

$$A = R_{2,plas} + [R_{2,dia} + R_{2,oxy} + \mu\cdot(\omega_{dia} + \omega_{oxy})^2]\cdot Hct - \mu\cdot(\omega_{dia} + \omega_{oxy})\cdot Hct^2$$

Eq.19

$$B = [R_{2,deoxy} - R_{2,oxy} + 2\mu\cdot(\omega_{dia} + \omega_{oxy})\cdot(\omega_{deoxy} - \omega_{oxy})]\cdot Hct - 2\mu\cdot(\omega_{dia} + \omega_{oxy})\cdot(\omega_{deoxy} - \omega_{oxy})\cdot Hct^2$$

Eq.20

$$C = \mu\cdot(\omega_{deoxy} - \omega_{oxy})^2\cdot Hct\cdot(1-Hct)$$

We can simplify the expressions by defining:

Eq.21

$$a_1 = R_{2,plas}$$

Eq.22

$$a_2 = R_{2,dia} + R_{2,oxy} + \mu \cdot (\omega_{dia} + \omega_{oxy})^2$$

Eq.23

$$a_3 = -\mu \cdot (\omega_{dia} + \omega_{oxy})^2$$

Eq.24

$$b_1 = R_{2,deoxy} - R_{2,oxy} + 2\mu \cdot (\omega_{dia} + \omega_{oxy}) \cdot (\omega_{deoxy} - \omega_{oxy})$$

Eq.25

$$b_2 = -2\mu \cdot (\omega_{dia} + \omega_{oxy}) \cdot (\omega_{deoxy} - \omega_{oxy})$$

Eq.26

$$c_1 = \mu \cdot (\omega_{deoxy} - \omega_{oxy})^2$$

and Eq.18-Eq.20 can be rewritten into:

Eq.27

$$A = a_1 + a_2 \cdot Hct + a_3 \cdot Hct^2$$

Eq.28

$$B = b_1 \cdot Hct + b_2 \cdot Hct^2$$

Eq.29

$$C = c_1 \cdot Hct \cdot (1 - Hct)$$

These six coefficients, a_1, a_2, a_3, b_1, b_2, and c_1, are the outcomes of the model fitting. The blood R_2 becomes a function of Y shown as Eq.2 in chapter 2.1.2.1.

3.5.2 In vivo blood experiment

Experiments on blood samples were performed on a 3 Tesla MRI system (Achieva, Philips Medical Systems, The Netherlands) using a quadrature head coil for radiofrequency (RF) transmission and reception. Sample preparation was similar to that used in our previous studies (Lu *et al* 2004; Zhao *et al* 2007). Briefly, bovine blood, which has physiologic and MR properties comparable to human blood (Benga and Borza 1995), was circulated in a tube to avoid precipitation. The temperature was controlled to be 37°C using a water bath and was monitored with a fiber optic sensor (Oxford Optronix, Oxford, UK). Oxygenation was controlled with a gas chamber and determined with a blood analyzer (Radiometer America Inc., Westlake, OH). Five Hct levels (controlled through mixing of plasma and blood cells) within the physiologic range (0.35-0.55) were studied. At each Hct level, four physiologically relevant oxygenation levels (0.4-1) were investigated.

Once the sample condition reached a stable state, the TRUST sequence was performed. For the case of blood samples, there is no partial voluming between blood and tissue or the need for control/label subtraction, thus only control images were acquired. Under each sample condition, four TRUST scans were performed with inter-echo spacing (τ_{CPMG}) of 10. For each TRUST scan, images with four different levels of T_2-weighting were acquired and these were achieved by placing 0, 4, 8 or 16 non-slice-selective preparation pulses before the

excitation pulse. Therefore, TRUST with τ_{CPMG} of 10ms, the T_2-preparation duration were 0, 40, 80, and 160 ms. Other imaging parameters were: field-of-view (FOV) 64x64 mm^2, matrix 32x32, slice thickness 5 mm, single-shot gradient-echo EPI, TR/TE/flip angle=8000ms/8ms/90°, half scan factor = 0.89, composite ($90°_x180°_y90°_x$) block pulses for T_2-preparation, MLEV16 RF phase cycling for multiple pulses, scan duration 2 minutes (Lu and Ge 2008b).

3.5.3 Data analysis and the results

The experimental data at different Hct and Y values were fitted to the model described in Eq.17-Eq.29 using a Matlab (Mathworks, Natick, MA) function, nlinfit, yielding six coefficients, a_1, a_2, a_3, b_1, b_2, and c_1. Note that, after characterization of the relationship between T_2, Y and Hct, the knowledge of two parameters should allow the estimation of the third, which was used in the validation study.

The data from the blood samples yielded highly reliable fitting. The 95% confidence intervals of the estimated R_2 ($1/T_2$) were 0.32 s^{-1}. Figure 21a shows a surface plot illustrating the relationship between blood T_2, Y and Hct for τ_{CPMG} of 10ms. The symbols indicated the experimental data points and the mesh showed the model-fitted surface. The coefficients from the fitting are listed in Table 3. Figure 21b shows two dimensional plots of T_2 and Y at a fixed Hct.

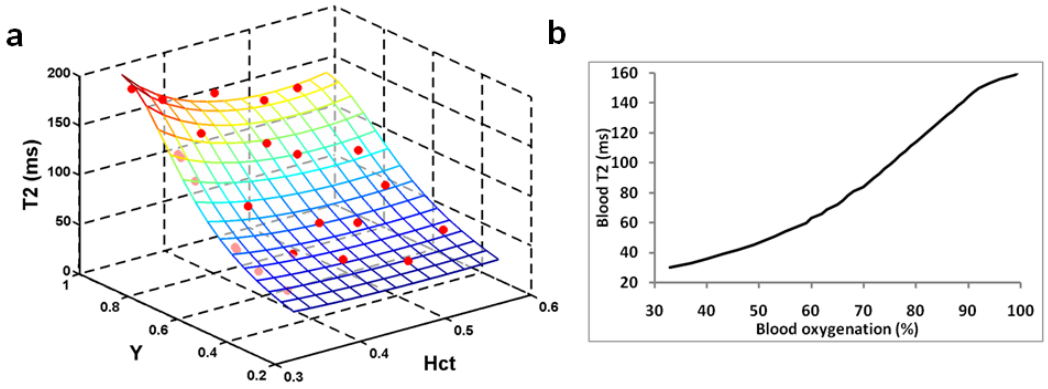

Figure 21 Relationship between T_2, Y, and Hct in blood samples.
(a) T_2 values of blood samples as a function of oxygenation (Y) and hematocrit (Hct) at τ_{CPMG} of 10ms. The symbols indicated the experimental data points and the mesh showed the model-fitted surface using Eq.17-Eq.29. The values of Y and Hct were written in fractions. (b) Two-dimensional plots between T_2 and Y at Hct of 0.4.

	a_1 (s^{-1})	a_2 (s^{-1})	a_3 (s^{-1})	b_1 (s^{-1})	b_2 (s^{-1})	c_1 (s^{-1})
τ_{CPMG} = 10 ms	-13.5	80.2	-75.9	-0.5	3.4	247.4

Table 3 Fitted coefficients for the model described in Eq.17-Eq.29.
These coefficients completely characterize the relationship between blood R_2/T_2, Y and Hct.

In the following studies, I draw blood about 3ml, and centrifuge the blood sample to measure the Hct, and converted the blood R_2 to Y based on this 3D calibration plot (Figure 21).

3.6 The validation for TRUST MRI

3.6.1 The idea of conducting the validation study

There is not a noninvasive standard way to measure Y inside the brain except inserting an oxygen sensor to intracranial cavity. Given the complexity of PET technique described in chapter 2, it is not a good way to validate TRUST

MRI. Unlike Y_v, the Y_a can be conveniently and accurately measured by the well established technique, Pulse Oximetry (PulsOx). The PulsOx, widely accepted on bedside, quantify the Y_a via measuring the obsorbtion of infra-red lights noninvasively at the finger tip. Sine the Y_a values are identical between the brain and the peripheral part of the body, Therefore, the TRUST MRI can be validated from the arterial side. That is measuring the arterial blood T_2 using TRUST MRI, which can be converted to Y_a via the calibration curve established in Chapter 3.5. The TRUST MRI estimated Y_a can be compared to the Y_a measured by gold standard Pulse Oximetry at finger. The drawback of validating TRUST MRI in such a way is that Y_a ranges from 96% - 100%, a relative constant from one person to another, which does not allow an enough dynamic range to validate TRUST MRI at the lower oxygenation level. This problem can be solved by reducing Y_a through a hypoxic challenge (defined by the lower O_2 condition). Hypoxia results a larger range of Y_a to validate the sensitivity and accuracy of TRUST MRI. Thus, the validation study is based on the idea that Y_a obtained from TRUST MRI is compared to that measured by Pulse Oximetry while Y_a is modulated by hypoxia.

3.6.2 MRI experiment

The human experiments were performed on a 3T using body coil for RF transmission and an eight-channel sensitivity encoding (SENSE) head coil for receiving. Foam padding was used to stabilize the head and minimize motion. The

protocol was approved by University of Texas Southwestern Medical Center's Institutional Review Board and informed written consent was obtained from each participant. Seven healthy subjects (3 men and 4 women, 28.9 ± 4.0 years of age) participated in this study.

Before the subject entered the bore of the magnet, a nose clip and a mouth piece were attached so that he/she could breathe through the mouth only. The mouth piece was attached to a two-way non-rebreathing valve (Hans Rudolph, 2600 series, Shawnee, KS) through which the researcher can control the type of inspired air. During the experiment, the subject first breathed room-air for eight minutes while survey, SENSE reference scan, and a (normoxia) TRUST scan were performed. Then the breathing air was switched to 500L bag containing 14% O_2 and 86% N_2 (equivalent to an altitude of 3,600 meters). From test data acquired outside MRI, I determined that it takes approximately 10 minutes after the gas switching for the physiologic parameters (e.g. O_2 and CO_2 levels) to reach a new steady state. Thus, a waiting period of 10 min was used to allow the arterial oxygenation to stabilize before a second (hypoxia) TRUST was performed. The following physiologic parameters were monitored and recorded throughout the MRI session: arterial oxygen saturation fraction (Y_a, in fraction) and heart rate (in beats per minute, bpm) were measured with a PulsOx device attached to a finger (MEDRAD, Pittsburgh, PA), End-tidal (Et) CO_2 (in mmHg) and breathing rate (in breaths per minute, bpm) were measured with a capnograph device (Capnogard,

Model 1265, Novametrix Medical Systems, CT). After the MRI scans were completed and the subject exited the scanner room, a blood sampling with a potassium ethylenediaminetetraacetic acid (EDTA) coated 10ml lavender tube was conducted on the basilic vein of the arm and Hct was measured with a centrifuge (Hemata STAT II, Separation Technology, Inc., Altamonte Springs, FL).

TRUST MRI measured T_2 of the blood in cerebral arteries. A balanced pseudo-continuous labeling scheme (Wong 2007; Wu *et al* 2007) was used with a labeling duration of 800ms and a short delay of 200ms. Based on arterial transit times measured previously for labeling and imaging locations comparable to this study (~1 sec) (Gonzalez-At *et al* 2000; Liu *et al* 2011), the use of these imaging parameters is expected to highlight arterial blood in large arteries before they entered intracortical arteries or arterioles. Major arteries are preferred over smaller arteries, which are known to have a lower Hct (Kuhl *et al* 1980), because our blood sampling and Hct measurement were conducted in the large vessels. The blood labeling position was chosen to be 84 mm below the anterior-commissure (AC) posterior-commissure (PC) line, based on a previous study (Aslan *et al* 2010). The imaging slice consisted of a single axial slice positioned at 10 mm above the AC-PC line. The other components of the TRUST sequence were similar to those used previously (Lu and Ge 2008b). The imaging parameters were: FOV 240x240 mm^2, matrix 64x64, voxel size 3.75x3.75x10

mm^3, TR=2522 ms, four T_2-weightings with the following effective TEs (associated with T_2-preparation): 0ms, 40ms, 80ms and 160ms, with a τ_{CPMG}=10 ms, 16 averages, scan duration 5 minutes and 24 seconds.

The TRUST MRI data were processed using in-house Matlab scripts and standard image processing software. The images with the same effective TE were realigned using a 2D realignment script in SPM2 (University College London, UK). The images at different effective TEs and between scans were co-registered using FSL's function FLIRT (FMRIB Software Library, Oxford University, UK). The estimation of blood T_2 from the TRUST data used procedures similar to the description at chapter 3.2. Briefly, after pair-wise subtraction between control and labeled images, a ROI was manually drawn to include the whole slice. The difference signals in the entire slice were averaged. Note that, although the signals in the control and labeled images have considerable partial voluming between vessel and tissue, the difference signals are expected to originate predominantly from vessels due to cancellation of static tissue signals. The averaged signals were fitted to a mono-exponential function to obtain T_2. The 95% confidence interval of the estimation was also obtained.

The T_2 values obtained from the TRUST data were compared to the predicted T_2 using PulsOx-measured Y_a and Centrifuge-measured Hct via the 3D calibration plot. Correlation analysis was performed between the predicted and experimental T_2. As an alternative analysis, the TRUST-derived T_2 and the Hct

value was used to estimate the arterial oxygenation level during hypoxia and the results were compared to the PulsOx Y_a values.

3.6.3 Results

The Y_a fell from 97.3±0.6% at normoxia to 84±3.6% at hypoxia, a significant decrease ($P<0.001$). Figure 22 shows a representative TRUST dataset with control, labeled and difference images at four effective TEs. During normoxia, the blood T_2 values were 154.2±13.1 ms (N=7, mean ± standard deviation). Since Y_a is close to unity during normoxia and is relative constant across subjects, the variations in arterial T_2 values are expected to be primarily attributed to Hct differences among individuals. Figure 23 shows a scatter plot between blood T_2 and Hct, confirming a significant correlation between these parameters ($P=0.03$). This relationship may be potentially exploited for non-invasive estimation of Hct.

During the hypoxia period, the blood T_2 measured with TRUST MRI was found to be 127.2±15.3 ms. Using the PulsOx-determined Y_a and Centrifuge-determined Hct, one can predict the blood T_2 from the 3D calibration plot (Figure 21a), which was found to be 128.6±18.4 ms. Figure 24 shows the scatter plot between the experimental and predicted T_2 values for both physiologic conditions (red symbols: normoxia data, blue symbols: hypoxia data). A significant correlation was observed ($P<0.001$). In the alternative analysis, using TRUST T_2 and Hct, the estimated Y_a was 0.837±0.036. These values are highly consistent

with the gold-standard values measured with PulsOx (0.840±0.036). The differences between TRUST-derived and PulsOx-measured Y were 0.003±0.026.

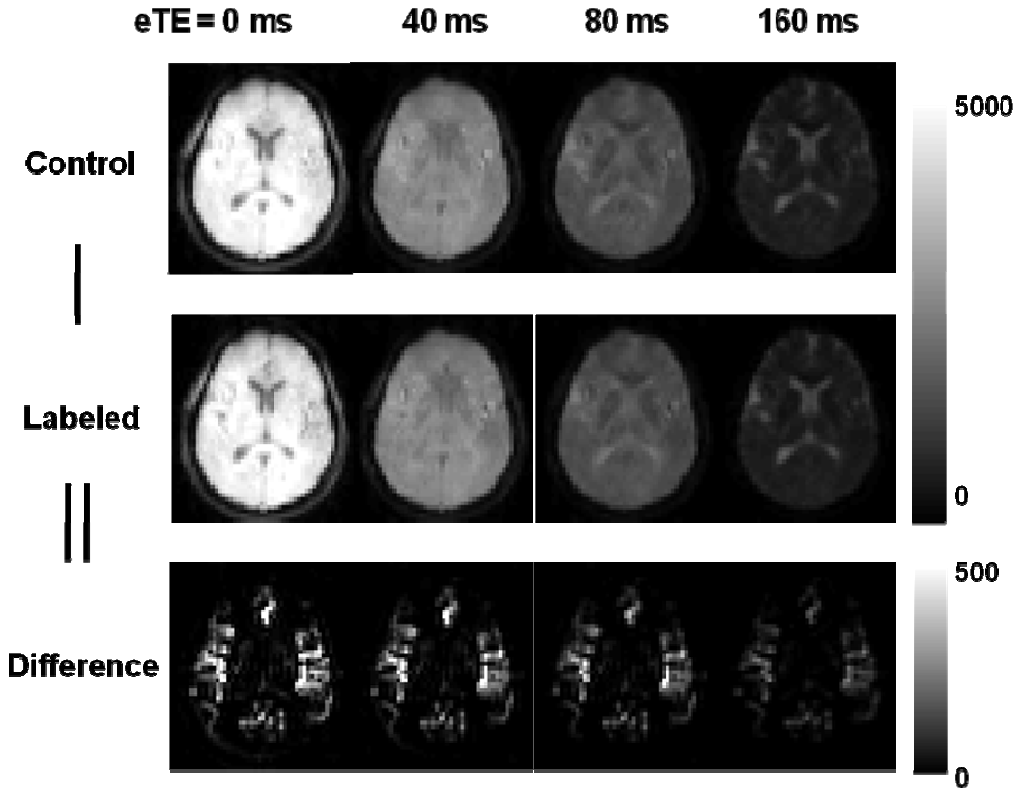

Figure 22 TRUST MRI images for the arterial side.
The scan acquired control and labeled images in an interleaved fashion. Each image type was acquired at four different T_2-weightings as indicated by the effective TE (eTE). The difference images were calculated from the subtractions. The difference images are displayed in a different color scale because their signal intensities are considerably lower than the control and labeled images.

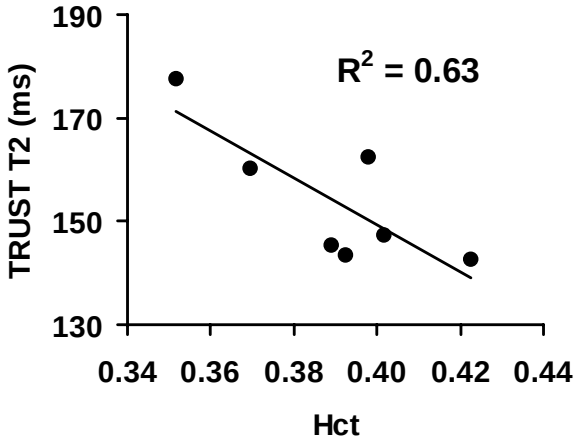

Figure 23 Relationship between arterial blood T_2 and hematocrit in humans during normoxia.
The T_2 was measured using TRUST MRI and the Hct was determined with a centrifuge. The arterial blood was close to full oxygenation under this condition (Y_a=0.973±0.006). The T_2 was therefore primarily dependent upon the Hct levels. The solid line represents the linear fitting curve. This plot is based entirely on the *in vivo* data, and did not involve the calibration data.

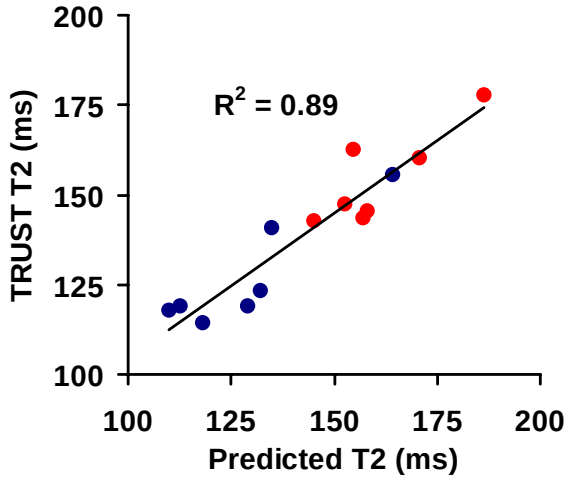

Figure 24 Scatter plot between TRUST-determined blood T_2 values and those predicted using the calibration plot with individual Y_a and Hct.
Red symbols indicate normoxia data points. Blue symbols indicated hypoxia data points. The solid line represents the linear fitting curve.

The *in situ* human validation study utilizing these calibration data revealed that the TRUST-derived arterial blood oxygenation values were in excellent agreement with those measured with a PulsOx device.

3.7 On improving the speed and reliability of TRUST MRI

3.7.1 The background of improving TRUST MRI efficiency

At present, typical duration of TRUST MRI is approximate 4 minutes with an estimation error of about 2%. Our goal is to be able to reduce the scan time to less than 2 minutes with a similar or even smaller error, which would considerably enhance its feasibility in clinical applications. A limitation of the current TRUST protocol is that an excessively long TR (e.g. 7500ms) needs to be used, as a shorter TR results in an over-estimation of R_2 due to magnetization disturbance from RF pulses in the previous TR. To resolve this problem, I modified the TRUST sequence by inserting a non-selective 90° RF pulse immediately following the EPI acquisition, termed post-saturation pulse, to "reset" the magnetization of all spins. In this way, the historical magnetization does not affect the current TR and unbiased R_2 estimation can now be achieved for all TR values tested (1500-7500ms at intervals of 750ms). Shorter TR was found to reduce signal intensity and the precision of R_2 fitting. Therefore, to improve the precision of the estimation, I tested the TE-dependence of the TRUST results. Recommendations for TRUST imaging parameters are provided with considerations of tradeoff between scan duration, accuracy, and precision.

3.7.2 Pulse sequence and simulation

The original TRUST sequence is shown in Figure 25a and was described in details previously in chapter 3.2. The sequence is similar to Arterial-Spin-Labeling (ASL) MRI, except that the labeling slab is above the imaging slice and that a series of non-slice-selective T_2-preparation pulses are placed before the excitation RF pulse. The modification made in the present study is shown as red symbols in Figure 25a, which consists of a non-slice-selective 90° pulse followed by dephasing gradients placed at the end of EPI echo train. This post-saturation pulse effectively resets the longitudinal magnetization of brain spins to 0, thus the spin history is removed and the magnetization evolution is independent of what happened in the previous TR periods. Figure 25b shows simulated magnetizations for blood and tissue under the post-saturation sequence.

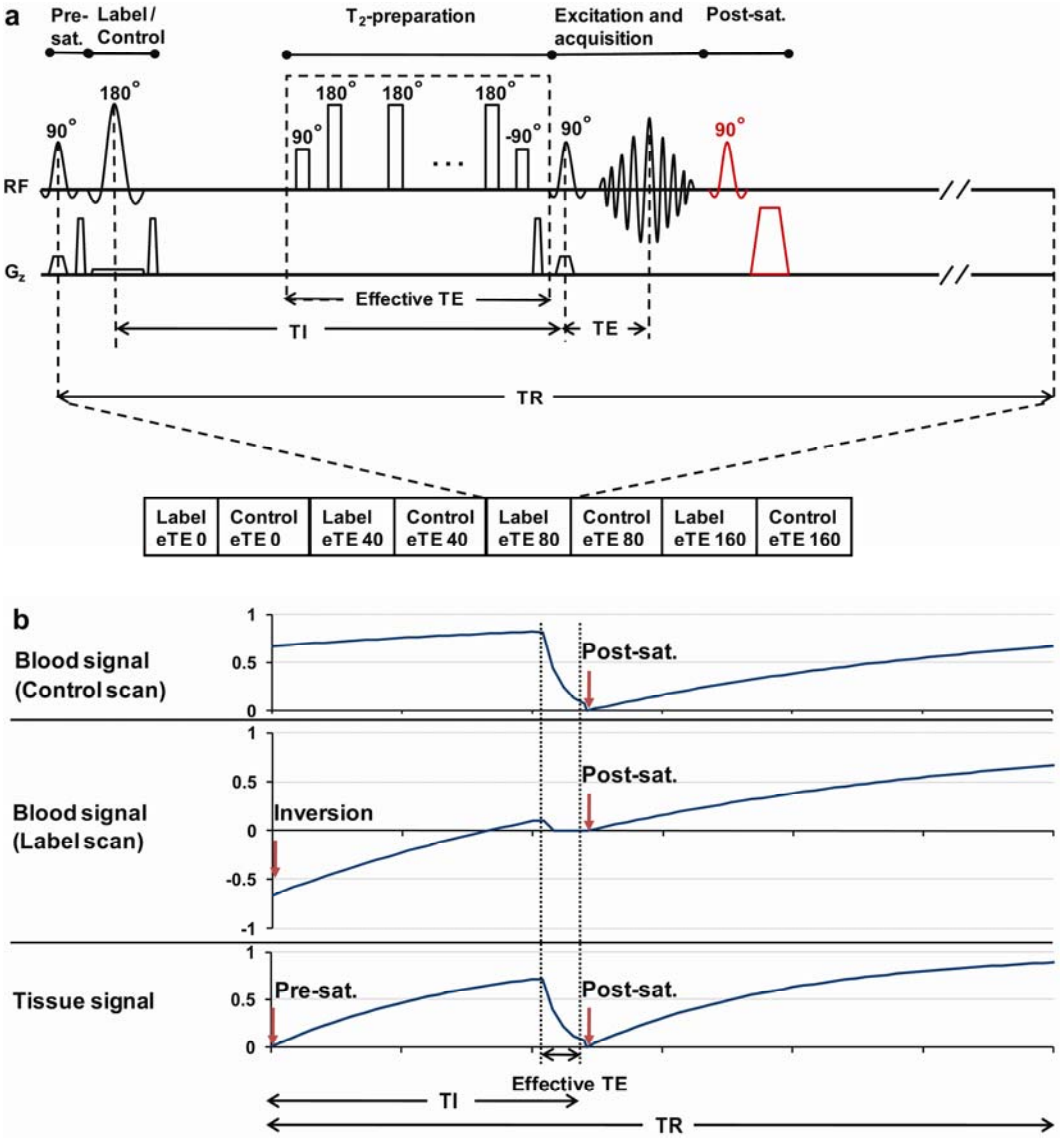

Figure 25 The post-sat TRUST MRI sequence and simulation.
(a) Sequence diagram. The original sequence components are shown in black and the modification proposed in the present study is shown in red. TRUST MRI acquires label and control images at different effective TEs (eTE). The eTE is varied by changing the number of non-selective 180º pulses, which is needed for the R_2-fitting. The limitation of the original TRUST sequence is that, at short TR, the non-selective 180º pulses can attenuate the magnetization of the whole brain, which reduces the signal in the next TR period. The extent of attenuation is dependent on eTE, thus would cause a systematic bias to the R_2-fitting. The proposed modification places a non-selective 90º pulse after the acquisition echo train, thereby removing all spin history and resetting all magnetizations to zero. While the addition of this RF pulse decreases the signal intensity, it eliminates the bias of R_2 which is eTE dependent. (b) Simulated magnetizations of blood and tissue under the post-saturation TRUST sequence using TR of 3000ms and eTE of 160ms. The magnetizations are shown for one TR period only. For clarity, only the components relevant for

the image intensity are plotted. Specifically, transverse component is used during the effective TE period while longitudinal component is used in the other time. For convenience, the time between pre-sat and labeling pulses is neglected. Similarly, the time between the excitation and the post-saturation pulses is neglected.

With the post-saturation TRUST sequence, the blood signal in the control scan is given by:

Eq.30

$$S_{control} = M_{0,b} \cdot (1 - e^{-(TR-eTE)\cdot R_{1,b}}) \cdot e^{-eTE \cdot R_{2,b}}$$

where TR is the repetition time, effective TE (eTE) is the duration of T_2-preparation, $R_{1,b}$ and $R_{2,b}$ are longitudinal and transverse relaxation rates of the blood, respectively. $M_{0,b}$ is the equilibrium magnetization of the blood. The signal in the labeled scan is written as:

Eq.31

$$S_{label} = M_{0,b} \cdot (1 + e^{-(TR-eTE)\cdot R_{1,b}} - 2e^{-(TI-eTE)\cdot R_{1,b}}) \cdot e^{-eTE \cdot R_{2,b}}$$

in which TI is the inversion time. The difference signal can then be calculated as:

Eq.32

$$\begin{aligned} S_{blood} &= S_{control} - S_{label} \\ &= [2M_{0,b} \cdot (1 - e^{-(TR-TI)\cdot R_{1,b}}) \cdot e^{-TI \cdot R_{1,b}}] \cdot e^{eTE \cdot (R_{1,b} - R_{2,b})} \\ &= S_0 \cdot e^{eTE \cdot C} \end{aligned}$$

where $S_0 = M_{0,b} \cdot (1 - e^{-(TR-TI)\cdot R_{1,b}}) \cdot 2e^{-TI \cdot R_{1,b}}$ and $C = R_{1,b} - R_{2,b}$. From Eq. [3], it is clear that the difference signal is a mono-exponential function of eTE and data fitting would yield the exponent, $R_{1,b}$-$R_{2,b}$. Note that $R_{1,b}$ is approximately 20 times smaller than $R_{2,b}$, thus the exponent is primarily determined by blood R_2. In

addition, by assuming $R_{1,b}$=0.62 s^{-1}, the influence of blood R_1 in TRUST MRI is further reduced.

It can also be seen that, while TR does not affect the exponential term of the fitting equation (therefore not causing biases), shorter TR results in a lower S_0 term (Figure 26), thereby reducing signal-to-noise ratio (SNR) and estimation precision. The TE dependence study was therefore conducted to improve the precision.

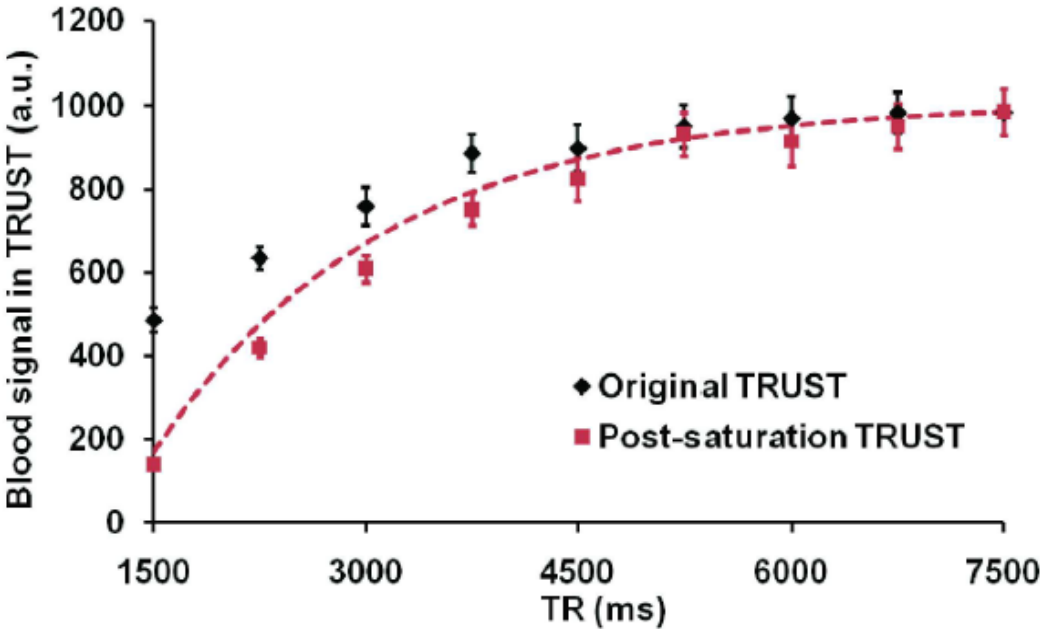

Figure 26 TRUST signal intensity (control-label) as a function of TR in the sagittal sinus. Data from the original and post-saturation TRUST are shown in black and red symbols, respectively. For post-saturation TRUST, simulation results using Eq.32 are also plotted (dashed line), demonstrating excellent correspondence with the experimental data. No simulation data are shown for the original TRUST, as the exact analytical expression of the signal is dependent on the magnetization history of individual spins and numerous assumptions are needed.

3.7.3 MRI experiment

General

The experiments were performed on a 3 Tesla MRI system (Achieva, Philips Medical Systems, The Netherlands) using body coil for RF transmission and an eight-channel sensitivity encoding (SENSE) head coil for receiving. Foam padding was used to stabilize the head and minimize motion. The protocol was approved by University of Texas Southwestern Medical Center's Institutional Review Board and informed written consent was obtained from each participant. Two sub-studies were conducted on separate cohorts: a TR-dependence study and a TE-dependence study. In order to maintain a constant physiological state during the entire scan (e.g. not falling asleep), the subjects were allowed to watch a movie.

TR-dependence study

Ten healthy volunteers (27±7 years old, 5 females, 5 males) participated in this study. Both the original TRUST (original TRUST) sequence without post-saturation and the TRUST with post-saturation were performed. For each sequence, nine TR values ranging from 1500ms to 7500ms with an interval of 750ms were tested. This study used a fixed TE of 7.0ms. The order of TR and sequences (original vs. post-saturation TRUST) was randomized for each subject to avoid time-dependent bias (e.g. due to fatigue or sleepiness). Other imaging

parameters were: inversion-recovery time (TI) of 1200ms; T_2-preparation times (effective TE, eTE) of 0ms, 40ms, 80ms and 160ms; matrix 64x64; voxel size 3.4x3.4x5mm^3; single-shot gradient-echo EPI; single slice perpendicular to sagittal sinus, scan duration ranging from 0.6 (for TR=1500ms) to 3.0 (for TR=7500ms) minutes.

TE-dependence study

Eight healthy volunteers (27±3 years old, 5 females, 3 males) participated in this study. Similar to ASL MRI, a shortest possible TE should be used for TRUST MRI. However, due to the length of EPI echo train, TE cannot practically approach 0. The previous TRUST protocol used parallel imaging to reduce the TE to 7.0ms, which is already shorter than that used in most ASL studies. TE can be further reduced by using a higher SENSE factor and/or a smaller half Fourier factor, which may, however, result in poor SNR as fewer data in the k-space are acquired. Therefore, I tested TE values of 7.0, 4.9 and 3.6ms to assess whether these small variations in TE could yield noticeably differences in TRUST data. The TE values used here correspond to k-line number of 31 (SENSE factor 2, half Fourier factor 0.9), 20 (SENSE factor 3, half Fourier factor 0.9), 17 (SENSE factor 3, half Fourier factor 0.7), respectively. The TR of this study was fixed at 8000ms and the original TRUST sequence was used. All other imaging

parameters are identical to those used in the TR-dependence study. The duration of each scan was 4.3 minutes.

Pilot study using the optimized TRUST protocol

Based on the TR and TE studies, recommendations were made in terms of optimal TR, TE, and pulse sequences. The optimized protocol was then applied on seven new volunteers (26±4 years old, 3 females, 4 males) to verify its performance. The imaging parameters were identical to those used in the above studies except that the choices of TR, TE, and pulse sequence (e.g. original vs. post-saturation TRUST) were based on outcomes of the TR and TE studies. This study used TR of 3sec and TE of 3.6ms, the total scan time is 1min and 12sec.

3.7.4 Data analysis

TRUST MRI data were processed using in-house MATLAB (Mathworks, Natick, MA) scripts. The processing method was identical to that described previously. Briefly, after motion correction, the sagittal sinus signal was obtained through the pair-wise subtraction between control and label images. This ROI tends to have about 30–50 voxels that include the vein as well as some surrounding tissue. To further define the venous voxels, the voxels with the highest blood signals (according to the difference signals) in the ROI were chosen as the final mask for spatial averaging. For the purpose of standardizing protocol, I used 4 voxels throughout the studies, although I have tested the effect of voxel

number and found that the results are relatively insensitive to the number. The difference signal was fitted to an exponential function of eTE, from which $R_{2,b}$ was obtained as described in Eq.32.

Quality of the raw data (i.e. MR images at different TR and TE values) and reliability of the fitted parameters (i.e. estimated R_2 values) were quantified using different indices. For the raw data, an SNR was calculated on a voxel-by-voxel basis, which was defined as the mean of the multiple measurements divided by the standard deviation across the measurements. Thus the SNR dependence on TR, TE, and pulse sequences can be examined. Reliability of the fitted parameters was assessed using two alternative indices, accuracy and precision of the estimation. The accuracy refers to the amount of systematic bias, and was evaluated by comparing the estimated R_2 to that of the longest TR or shortest TE, which was assumed to reflect the true value. The precision refers to the uncertainty of the estimation, and was quantified by the standard error of R_2 (ε_{R2}) from the goodness-of-fit assessment of the data fitting.

Y_v was estimated from the blood R_2 using a calibration curve described in Chapter 3.5. Error propagation from R_2 to Y_v was conducted by converting $R2 \pm \varepsilon R2$ values to corresponding $Y_v \pm \varepsilon Y_v$. All Y_v and εY_v values are written in units of oxygen saturation percentage (%).

For statistical analysis, a mixed effect model was used to assess whether there is a dependence of R_2 or ε_{R2} on TR or TE. The software *R*

(Wirtschaftsuniversität Wien Vienna University, Austria) was used for this analysis. A P value of less than 0.05 after correcting for multiple comparisons is considered statistically significant.

3.7.5 Results

TR-dependence study

Figure 26 shows the blood signal (i.e. the difference between control and label images) as a function of TR (eTE=0 only) using the original TRUST (black symbols) and post-saturation TRUST (red symbols) sequences. The signal intensity decreased at shorter TR, which is consistent with the simulation results using Eq. [3] (dashed line in Figure 26). Figure 27a shows the estimated R_2 as a function of TR. For the original TRUST sequence, shorter TR resulted in an over-estimation in R_2 ($P<0.001$ with mixed-effect model), confirming our previous report (Lu and Ge 2008b). No such dependence was observed for the post-saturation TRUST ($P=0.24$), supporting our hypothesis that the addition of the non-selective pulse can remove the bias and improve the estimation accuracy. Figure 27b plots the standard error of R_2, ε_{R2}, as a function of TR. Shorter TR resulted in poorer estimation precision for both the original TRUST ($P<0.001$) and the post-saturation TRUST ($P<0.001$). This can be explained by the lower signals at shorter TR as shown in Figure 26. I have also examined ε_{R2} per unit time by accounting for the larger number of repetitions one can obtain with a shorter TR. It was found that the error was lowest at a TR of 3000ms (Figure 27c).

TE-dependence study

In the tissue regions, shorter TE corresponded to a lower SNR ($P<0.001$ for TE of 3.6ms vs. 7.0ms), which can be attributed to the reduced k-space sampling associated with parallel imaging and partial Fourier acquisition. In the sagittal sinus, on the other hand, shorter TE improved the signal stability. The SNR of the blood signal was 62±7, 40±6, and 33±6 for TE of 3.6ms, 4.9ms, and 7.0ms, respectively ($P=0.008$ with mix-effect model). This SNR increase is considerable given the relatively small change in TE, and may be because the outflow effect of the blood is drastically reduced at shorter TE. Accordingly, the precision of the blood R_2 estimation was improved at shorter TE ($P<0.001$). Figure 28a shows ε_{R2} as a function of TE, demonstrating that the estimation error at TE=3.6ms was only 51% of that at TE=7.0ms. A weak dependence of R_2 on TE was also observed (Figure 28b, $P=0.017$). Data using longer TE were found to slightly over-estimate R_2. A more careful investigation suggested that the over-estimation (calculated as $R_{2,TE=7.0}–R_{2,TE=3.6}$) was subject-dependent (Figure 28c, $P<0.001$), and an individual with lower SNR tends to have a more pronounced over-estimation. For data with SNR>50, the over-estimation is negligible. Therefore, higher SNR afforded by shorter TE can improve both accuracy and precision of the TRUST data.

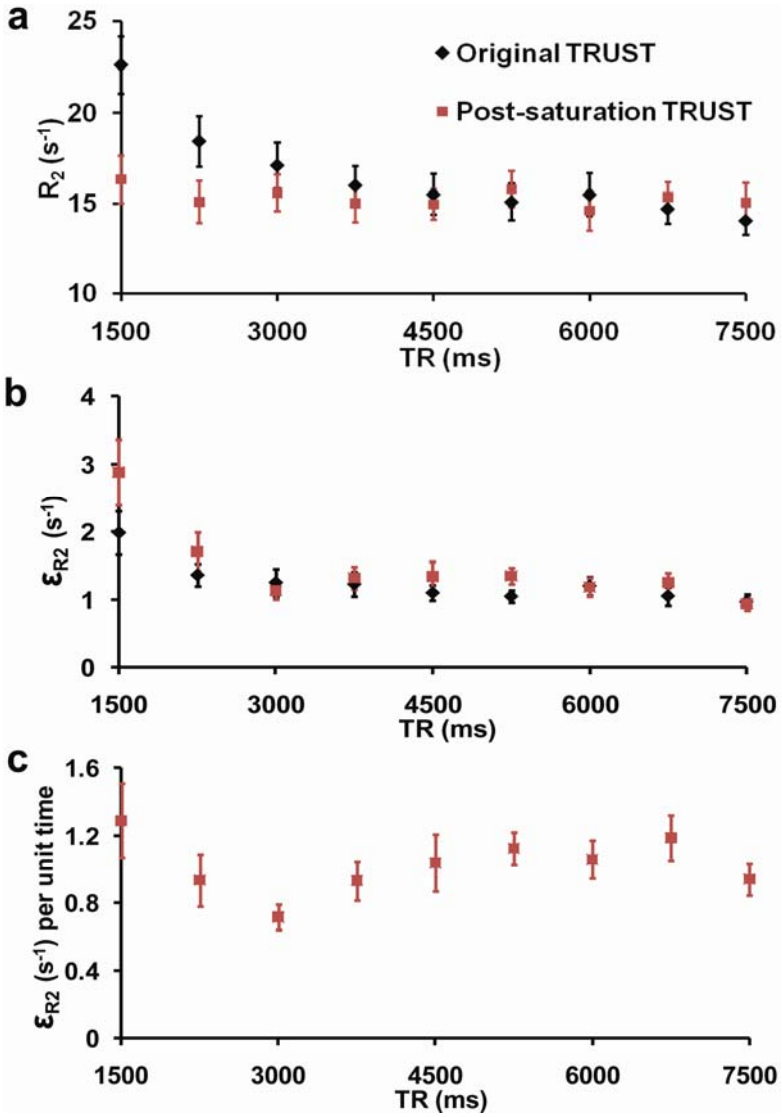

Figure 27 Effect of TR on TRUST MRI results (N=10).
(a) Estimated R_2 (=$1/T_2$) as a function of TR. Data from the original and post-saturation TRUST are shown in black and red symbols, respectively. The R_2 from the original TRUST shows a TR-dependence (P<0.001), while it is not the case for the post-saturation TRUST (P=0.67). (b) Standard error of R_2 (ε_{R2}) from the goodness-of-fit assessment of the data fitting at different TR. This index represents the uncertainty in the estimation and is used as an indicator for precision. As expected, a shorter TR resulted in poorer precision in both sequences. (c) ε_{R2} per unit time, which was computed by multiplying the corresponding values in (b) by $\sqrt{TR/7500}$, where 7500 (ms) is the longest TR used in the TR dependence study.

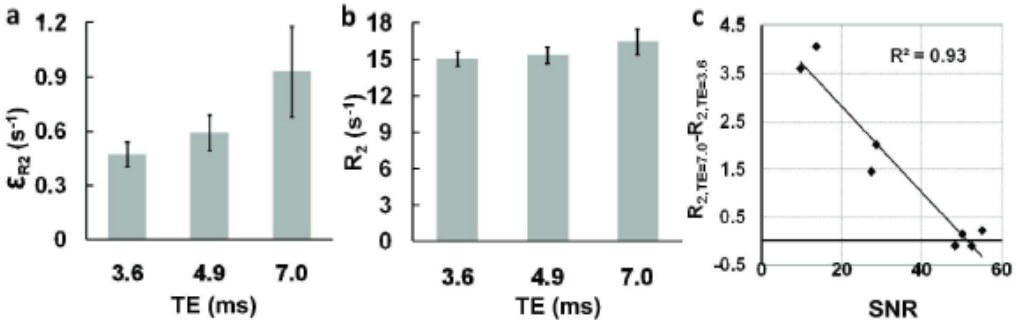

Figure 28 Effect of TE on TRUST MRI results (N=8).
(a) εR2 at different TE values. Shorter TE corresponds to considerably smaller estimation error. (b) Estimated R2 at different TE values. R2 is weakly dependent on TE (P=0.017). R2 from TE of 7.0ms appears to contain some over-estimation compared to TE of 3.6ms. (c) The amount of R2 over-estimation is correlated with SNR (P<0.001). An individual with lower SNR tends to have more over-estimation. For data with SNR>50, the over-estimation is negligible.

Pilot study using the optimized TRUST protocol

Based on the TR and TE studies, the optimal protocol was determined to be TR=3000ms and TE=3.6ms using the post-saturation sequence. Data acquired using this protocol revealed R_2=15.4±0.7s^{-1} and ε_{R2}=0.39±0.04s^{-1} (N=7, mean ± standard deviation). Using an in vitro calibration curve, these values correspond to Y_v=63.5±1.6% (in absolute unit) and ε_{Yv}=0.98±0.11%.

3.7.6 Discussion

The main goal of the present study is to conduct further technical development for TRUST MRI so that it can be performed with a shorter duration without degradation of estimation reliability. The current TRUST protocol takes approximately 4 minutes and a major reason for the relatively long duration is the large TR. A shorter TR can reduce the scan duration, but our previous study has shown that it also causes a systematic bias in the estimated R_2 value (Lu and Ge

2008a). The post-saturation TRUST proposed in the present study effectively eliminated the bias, allowing the sequence to take advantage of a shorter TR and scan duration. An unwanted effect of shorter TR is the lower estimation precision. Therefore, TE of the sequence was also optimized and it was found that a modest reduction of TE can considerably improve the precision of blood R_2. Combining these findings, I recommend the use of post-saturation TRUST sequence with a TR of 3000ms and a TE of 3.6ms for future studies, which is expected to shorten the scan duration by 60% while maintaining the estimation reliability. Compared to the previous TRUST protocol, the choice of this TR value is expected to shorten the scan duration by 60%, while the use of post-saturation can remove the systematic bias which is estimated to be about 3% (in oxygen saturation percentage) at a TR of 3000ms.

A number of techniques have been developed to quantitatively estimate blood oxygenation in the brain. One approach exploits the susceptibility effect of deoxyhemoglobin on extravascular tissue (An and Lin 2003; He and Yablonskiy 2007), and uses simultaneous acquisitions of gradient and spin echoes to obtain Y_v. A second approach measures the phase angle of intravascular blood signal, and estimates Y_v based on the susceptibility effect in venous blood (Fernandez-Seara *et al* 2006; Haacke *et al* 1997). The advantage of this susceptometry technique is tha tit provides greater temporal resolution as the data acquisition can be completed within 30 seconds. A third method is based on T_2 value of blood

signal which can be converted to Y_v using a calibration plot (Golay *et al* 2001; Lu and Ge 2008a; Oja *et al* 1999; Qin *et al* 2011; Wright *et al* 1991). The advantages of T_2-based methods are that only mono-exponential fitting is needed and that it is less sensitive to vessel orientation. A further advance brought by TRUST is that partial voluming between vessel and tissue can be accounted for and the estimation is no longer susceptible to subjective ROI selection, rendering the technique a high test-retest reproducibility (Lu and Ge 2008a) and sensitivity to physiologic alterations (Xu *et al* 2010; Xu *et al* 2011). At present, the scan duration is somewhat long for certain patient populations. With the improvement introduced in this study, TRUST scan can be completed within 1 minute and 12 seconds, and this protocol is now routinely used in our application studies. It is also important to point out that, with this protocol, the estimation error on R_2 is about $0.4s^{-1}$, corresponding to 1% error in venous oxygenation (in units of oxygen saturation percentage).

Using the original TRUST sequence, shorter TR showed an over-estimation of blood R_2. Conceptually, this is because the RF pulses (specifically the T_2-preparation pulses) in the previous TR period attenuated the magnetization in the next TR. Furthermore, the attenuation effect is greater when more T_2-preparation pulses are used. That is, signal at longer eTE is attenuated more than that at shorter eTE. Thus, the T_2-dependent signal decay appears faster than it should be. An alternative way to illustrate this effect is by signal equations.

Assuming that the spins measured during the present TR had experienced the T_2-preparation pulses in the previous TR, one can write the difference signal as:

Eq.33

$$S_{blood} = [2M_{0,b} \cdot (1-(1-e^{-eTE \cdot R_{2,b}}) \cdot e^{-(TR-TI) \cdot R_{1,b}}) \cdot e^{-TI \cdot R_{1,b}}] \cdot e^{eTE \cdot (R_{1,b}-R_{2,b})}$$
$$= S_0(eTE) \cdot e^{eTE \cdot C}$$

In contrast to Eq.32, the term in the bracket in Eq.33 is now dependent on eTE. Thus, when using a mono-exponential function to fit these data, the estimated exponent will be greater than its true value. It is interesting to point out that the signal in Eq.32, S_{blood}, is actually smaller than that in Eq.33. That is, the post-saturation pulse reduced the TRUST signal, which is consistent with the experimental data shown in Figure 26. But its advantage is that the bias is removed. The term in the bracket in Eq.33 will be identical to that in Eq.32 when eTE approaches infinity. It should also be noted that the exact signal in the original TRUST is even more complicated than Eq.33 as the magnetization could also be affected by labeling and excitation RF pulses as well as RF pulses in the earlier TR periods, which was not accounted for in the above equation.

Post-saturation pulses similar to that used in the present study have been employed previously in ASL MRI (Pell *et al* 1999) and Vascular-Space-Occupancy (VASO) MRI (Lu 2008). In those studies, the purpose o fthe post-saturation was to reset magnetization of the arterial blood instead of the venous blood. For example, Pell and colleagues devised a modified flow-sensitive

alternating inversion recovery (FAIR) approach in which a post-saturation pulse was inserted after the acquisition echo train. The authors showed that the modified FAIR sequence can reduce the time for spins to reach a steady state and simplifies the flow quantification. However, the authors also pointed out that the method works effectively when the RF transmission coil covers the entire subject (e.g. including the heart), in which all spins being imaged have previously experienced the saturation pulse (thus their magnetization has been reset). Unfortunately, in human MRI systems, the body coil does not really provide full-body coverage when used for brain imaging. Consequently, the performance of the post-saturation pulse is dependent on other parameters such as arterial transit time, inversion time, and delay time, as shown by both Pell et al and Lu. The application of post-saturation pulse in TRUST MRI provides a unique advantage in that the venous spins being imaged originate from smaller veins or parenchyma tissues and, since these spins were inside the body coild coverage, their manetization has been reset before entering the imaging slice. That is, the post-saturation pulse works more effectively for the venous side compared to the arterial side.

The finding that shorter TE resulted in more precise estimation is not as trivial as it seems at first sight. While shorter TE would correspond to higher signal based on theory, it is important to note that a shorter TE is achieved at the expense of k-space coverage (via higher SENSE factor and/or lower partial

Fourier factor). Fewer data samples in the k-space are associated with higher noise levels, thus shorter TE does not always result in higher SNR. As a matter of fact, our data showed that a TE of 3.6ms yielded lowest SNR in the tissue regions. This is consistent with the common practice in ASL literature that few studies used a TE of less than 5ms (Hendrikse *et al* 2003; Wang *et al* 2002). For the blood signal in the TRUST data, however, shorter TE resulted in a drastic increase in SNR and estimation precision (Figure 28a). This improvement was attributed to both a signal increase (by 31%) and a noise reduction (by 34%) at shorter TE. Numerical simulations confirmed that such a large increase in signal intensity is expected for spins flowing at a velocity characteristic of the sagittal sinus. The extent of the noise reduction was also consistent with simulations using pulsatile flow (22-60 cm/s within one cardiac cycle, mean velocity 35 cm/s). Therefore, we hypothesize that the noise reduction at shorter TE is primarily attributed to a reduction in pulsation-related fluctuation. An alternative strategy to the use of a short TE is to apply flow-compensating gradients. Although the use of additional gradients will increase the TE value, flow-compensation are expected to improve spin coherence within a voxel. The benefit of such schemes shall be assessed in future studies.

The findings from the present study should be interpreted in view of a few limitations. First, the TR and TE dependence studies were conducted in separate cohorts, making the results not directly comparable. This design was chosen

because of the relatively long duration of each study. The TR dependence study included 18 TRUST scans with varying TR and took about 1 hour. The TE dependence study takes about half an hour. I was concerned that excessive long scan time may result in greater motion and physiologic fluctuations. Thus I separated the TR and TE studies. During the scan, the subjects were allowed to watch a movie to prevent them from falling asleep. Second, in explaining the TR-dependent over-estimation in the original TRUST sequence, I have primarily focused on the spin history and magnetization evolution. The smaller SNR in the shorter TR scans could have also contributed to the higher R_2, as demonstrated in the TE-dependence study. However, I note that the effect of SNR on R_2 overestimation is on the order of 1 s^{-1}, which is much less than that observed in the experimental data (Figure 27a). Thus, the spin history effect is the predominant factor in the TR-dependence data.

3.7.7 Conclusion

The speed and reliability of cerebral oxygenation measurement was improved by using a modified implementation of TRUST MRI. The optimal TRUST sequence is to choose the use of post-saturation with a TR of 3000ms and a TE of 3.6ms, which allows the determination of global venous oxygenation with scan duration of 1 minute 12 seconds and an estimation precision of ±1% (in units of oxygen saturation percentage) .

3.8 The reproducibility study for the $CMRO_2$ method

3.8.1 Introduction

Testing the reproducibility is required to assess the applicability and reliability of one technique. These two features are important to push this $CMRO_2$ technique to the bedside. Repeatedly measuring $CMRO_2$ reveals the variation introduced by repositioning the subject and the subject's physiology fluctuation.

3.8.2 MRI Experiment

The $CMRO_2$ measurement was performed on five volunteers for five times (26±4 years old, 2 females, 3 males). Each volunteer participated five $CMRO_2$ studies at five different days which were finished within two weeks. To minimize the repositioning variation, a screen shot of each scan's planning was taken on the first day for following scans' reference. MRI technician was trained to position the patient and scanner table as similar as possible. The scan time was randomized across days to simulate the condition of clinical scans.

Similar to previous study, the $CMRO_2$ measurement includes TRUST MRI, time of fly angiogram, phase-contrast MRI and T1-MPRAGE. Based on the TR and TE studies, the post-saturation TRUT pulse sequence are used with the optimal TR of 3000ms and TE of 3.6ms. The imaging planning of phase-contrast MRI is optimized as such that each phase-contrast scan is performed perpendicular to a single artery. In total, four phase-contrast scans are performed at the level of foramen magnum. As previous study, an angiogram of arteries is

used for planning phase-contrast scans. The other imaging parameters were identical to those used in the above studies except that the choices of TR, TE, and pulse sequence (e.g. original vs. post-saturation TRUST) of TRUST MRI.

3.8.3 Results and conclusions

Figure 29a-c shows the time courses of CBF, Y_v and $CMRO_2$ which are displayed in the same scale (mean ± 30% mean). The time dependent variation of CBF, Y_v and $CMRO_2$ across days are 6±2%, 3±1% and 5±2% of the group mean respectively. Assuming the same repositioning error, the $CMRO_2$ is a more stable physiology parameter than CBF and Y_v. $CMRO_2$ also shows a smaller dynamic range across subjects on each day (Figure 29). This suggests that $CMRO_2$ might be more sensitive to distinguish the difference, which might give a good power to do group comparison, such as the normal versus the diseased. The reason for a tight range of $CMRO_2$ for healthy young adults is that the CBF and Y_v are closely correlated (Figure 29d). So the subject who has big CBF tends to have high level of Y_v, but the $CMRO_2$ might not higher than others because CBF and Y_v affect $CMRO_2$ in an opposite way.

In conclusion, this $CMRO_2$ quantification technique is fairly reproducible. The fluctuation of $CMRO_2$ across days only accounts for 5% of the mean. Given that the fluctuation of $CMRO_2$ is partially contributed from both Y_v and CBF, $CMRO_2$ is a steady physiological parameter comparing to CBF and Y_v. $CMRO_2$ is

also a homogeneous parameter meaning a less variation across people, making it a potential sensitive biomarker to diagnose abnormalities.

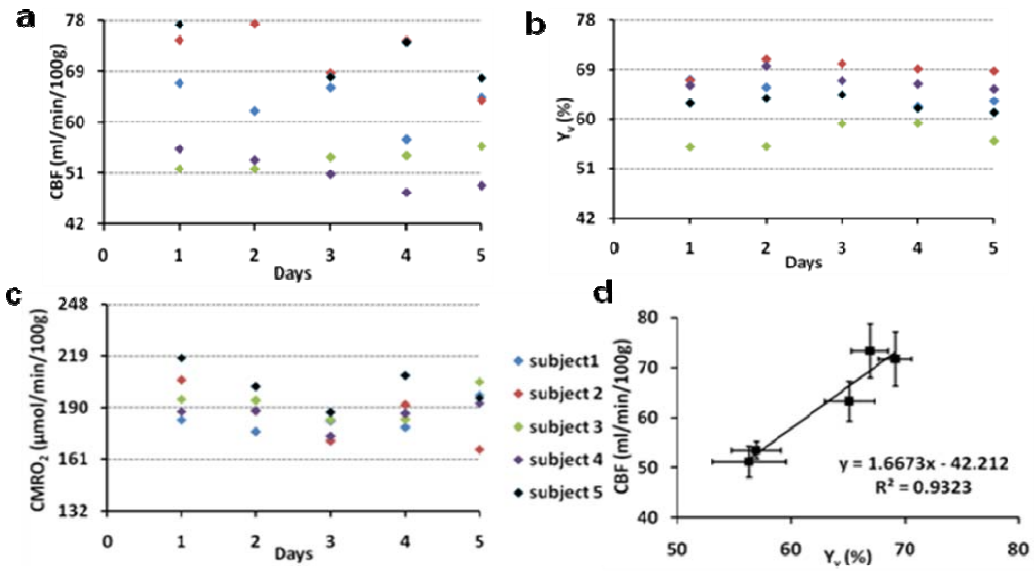

Figure 29 The time course of (a) CBF, (b) Y_v and (c) $CMRO_2$ across days.
Each color encodes one subject, and each dot is one measurement. (d) The scatter plot of CBF and Y_v of subjects. Each dot is the one subject measurements that averaged over five days. The horizontal and vertical error bar is the standard deviation (SD) Y_v and CBF over five days respectively. The scale of this plot is mean±30% of mean for all the parameters to display the variation range for each parameter.

4 The CO_2 and O_2 effect on neural activity

4.1 The motivation to study CO_2/O_2 effect

One of the key goals in many clinical interventions is to be able to modulate the brain's activity as needed. In some circumstances such as neurodegenerative diseases, one often aims to enhance the brain activity. In other cases such as epileptic seizures, one wishes to decrease brain activity. Existing approaches includes surgical procedures, transcranial stimulation, and pharmacological treatment. However, these approaches have their respective limitations. For instance, the complexity and invasiveness of surgical procedure limits the application on general population. Transcranial stimulation does not work well for the deep brain structure. Pharmacological treatment usually gives some side effects. It would be of great interest to develop a non-invasive, convenient and cost-effective means to modulate the brain activity.

With that purpose, I investigated the effect of controlling the inhaled air on the brain activity. In normal barometric condition, the fraction of O_2 is about 21% of the atmosphere, and virtually no CO_2. Increasing inhaled CO_2 is called hypercapnia, increasing inhaled O_2 is called hyperoxia and reducing inhaled O_2 is called hypoxia. Chronic exposure to any of these conditions may lead to a neurovascular change. I used the technique developed in chapter 3 to quantitatively asses the acute responses of the brain to hypercapnia (chapter4.2), hyperoxia and hypoxia (chapter 4.3).

4.2 he effect of CO_2 on the brain activity and metabolism in conscious humans

4.2.1 Abstract

A better understanding of CO_2 effect on brain activity may have a profound impact on clinical studies employing CO_2 manipulation to assess cerebrovascular reserve and on the use of hypercapnia as a means to calibrate fMRI signal. The present study investigates how an increase in blood CO_2, via inhalation of 5% CO_2, may alter brain activity in humans. Dynamic measurement of brain metabolism revealed that mild hypercapnia resulted in a suppression of cerebral metabolic rate of oxygen ($CMRO_2$) by 13.4±2.3% (N=14, Mean±SEM) and, furthermore, the $CMRO_2$ change was proportional to the subject's end-tidal CO_2 change. When using functional connectivity MRI (fcMRI) to assess the changes in resting-state neural activity, it was found that hypercapnia resulted in a reduction in all fcMRI indices assessed including cluster volume, cross-correlation coefficient and amplitude of the fcMRI signal in the default mode network (DMN). The extent of the reduction was more pronounced than similar indices obtained in visual-evoked fMRI, suggesting a selective suppression effect on resting-state neural activity. Scalp electroencephalogram (EEG) studies comparing hypercapnia to normocapnia conditions showed a relative increase in low frequency power in the EEG spectra, suggesting that the brain is entering a low arousal state upon CO_2 inhalation.

4.2.2 Introduction

Carbon dioxide (CO_2) is a potent vasodilator and an increase of CO_2 in the inspired air is known to cause a number of vascular changes in the brain (Kastrup *et al* 1999; Rostrup *et al* 2000; Sicard and Duong 2005), including increased cerebral blood flow (CBF), cerebral blood volume (CBV) as well as higher CO_2 and O_2 concentrations in the blood. The potential effect of CO_2 inhalation on neural activity is not clear. Existing literature mostly presumes that altering CO_2 partial pressure has no effect on brain tissue and the use of CO_2 inhalation or the carbonic anhydrase inhibitor acetazolamide can be considered a purely vascular challenge to assess cerebrovascular reserve (de Boorder *et al* 2004) or to calibrate fMRI signal (Chiarelli *et al* 2007a; Davis *et al* 1998; Kim and Ugurbil 1997).

Despite the wide acceptance and application of these assumptions in cerebrovascular research, some evidence suggested that the influence of CO_2 on brain activity merits more research. An important marker for tissue function, cerebral metabolic rate of oxygen ($CMRO_2$), has been investigated under hypercapnia conditions. The results, however, were not consistent in the literature. A few studies (Barzilay *et al* 1985; Kety and Schmidt 1948b; Novack *et al* 1953) reported that $CMRO_2$ remains constant with hypercapnia, while other studies found a decrease (Kliefoth *et al* 1979; Kogure *et al* 1975; Sicard and Duong 2005) or increase (Horvath *et al* 1994; Jones *et al* 2005; Yang and Krasney 1995) in $CMRO_2$. More recent findings in brain slices and anesthetized animals provided

evidence at the cellular level that higher CO_2 partial pressure can have a profound effect on neural tissue including reducing pH, elevating adenosine concentration, and suppressing synaptic potentials (Dulla *et al* 2005; Gourine *et al* 2005; Zappe *et al* 2008b). However, these previous studies were largely performed under laboratory conditions and it is unclear if the results were influenced by certain factors including the anesthetic agent, which by itself will reduce neural activity (Shulman *et al* 1999). I am therefore interested in conducting measurements in conscious human subjects under physiologically relevant conditions.

The study of neural response to CO_2 pressure change is particularly challenging compared to studies employing sensory, motor or cognitive stimuli. Traditional tools such as PET, fMRI and optimal imaging are not readily usable, because these methods all use vascular response as a surrogate for neural function (Fox and Raichle 1986). However, CO_2 is known to have a strong vascular effect that is present even if neural activity does not change (e.g. it has been shown to change vessel size even in dissected blood vessels). Therefore, an observation of altered blood flow, blood volume or BOLD fMRI signal alone would not necessarily suggest a change in neural activity (Biswal *et al* 1997). In fact, the vascular effect of CO_2 may be a nuisance in the study of tissue. It is perhaps for these reasons that the exact influence of CO_2 inspiration on neural activity is not fully characterized to date (Horvath *et al* 1994; Jones *et al* 2005; Kety and Schmidt 1948b; Kliefoth *et al* 1979).

The present study employed three non-invasive techniques to assess the effect of breathing a CO_2-enriched air (5% CO_2, 21% O_2, 74% N_2) on brain tissue. We have recently developed an MRI technique to quantify $CMRO_2$ (Lu and Ge 2008b; Xu *et al* 2009), allowing us to assess the effect of CO_2 on neural metabolism. In the first study, I compared the participant's $CMRO_2$ levels when breathing CO_2-enriched gases (referred to as hypercapnia) to breathing normal room-air gases (normocapnia). In the second study, I investigated the spontaneous neural activity under normocapnia and hypercapnia conditions by performing functional connectivity MRI (fcMRI). Finally, neural electrical potential was investigated directly by scalp electroencephalogram (EEG) under room-air and CO_2 breathing conditions.

4.2.3 Material and method

Participants

A total of fifty healthy subjects (27.9±6.5 years old, 32 males and 18 females) were studied. Each subject gave an informed written consent before participating in the study. The study protocol was approved by the Institutional Review Board of the University of Texas Southwestern Medical Center. These subjects were divided into four groups for different arms of the study. Fourteen subjects were studied to assess the effect of CO_2 inhalation on $CMRO_2$. Ten subjects were studied in the $CMRO_2$ sham control study. Fourteen subjects were

studied to assess the effect of CO_2 on resting state functional connectivity. Twelve subjects were studied to assess the effect of CO_2 on EEG spectra.

CO_2 manipulation

CO_2 delivery was achieved by using a gas delivery system created in our laboratory, with only non-metallic components (Figure 30). With this system, a change in gas content can be made without stopping the scan or recording and without moving the subject.

Before the start of each study, subjects were given instructions regarding the protocol and were fitted with a nose clip. Hypercapnia was induced by breathing a gas mixture of 5% CO_2, 74% N_2 and 21% O_2 delivered from a plastic bag through a two-way non-rebreathing valve and mouthpiece combination (Hans Rudolph, 2600 series, Shawnee, KS). A research assistant was present during the experiments to monitor the subjects and to switch the valve on the gas delivery system. Physiologic parameters, end-tidal (Et) CO_2, heart rate (HR), breathing rate (BR) and arterial oxygenation (Y_a), were monitored and recorded during the experiments (MEDRAD, Pittsburgh, PA, and Novametrix Medical Systems, Wallingford, CT).

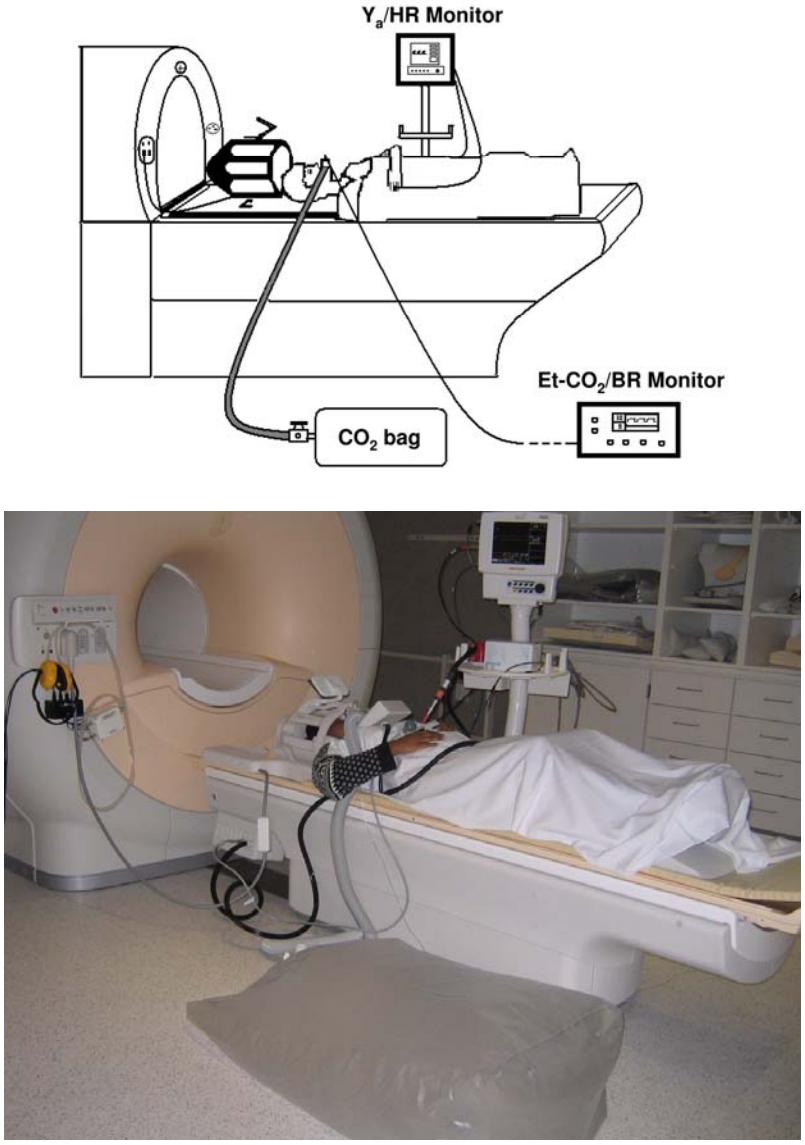

Figure 30 The hypercapnia experiment setup.
The 5% CO_2 balanced with room air is filled in the airbag, and the airbag is connected with the two-way valve with the tube sending the gas to the subject's mouth. The subject's nose is blocked with nose clip and his/her finger is clipped with the pulse oximetry sensor to monitor the heart rate and arterial oxygenation. The exhaled air is sampled through the sampling tube and analyzed by the carpnometer outside MRI room for end-tidal CO_2 and breathing rate.

Measurement of global $CMRO_2$

Measurement of $CMRO_2$ was performed on a 3 Tesla MRI system (Philips Medical Systems, Best, the Netherlands) using the same method described in Chapter 3. The anatomical location of TUST MRI and phase-contrast MRI is sagittal sinus.

The experiment began with the subject breathing room-air for 4 minutes, establishing a normocapnic state, during which $CMRO_2$ was determined. The subject was then switched to the gas mixture containing 5% CO_2 and continued to breath for another 6 minutes. I waited for two minutes to allow for physiological stabilization in the hypercapnic state (Figure 31). $CMRO_2$ was measured again in the last four minutes under stable hypercapnia condition.

The data processing procedures for TRUST MRI and phase contrast MRI were based on an algorithm described previously. The arterial blood oxygenation, Y_a, was recorded at 1 sample/second and the data corresponding to MRI acquisition period (about 4 min) were averaged to yield the final value.

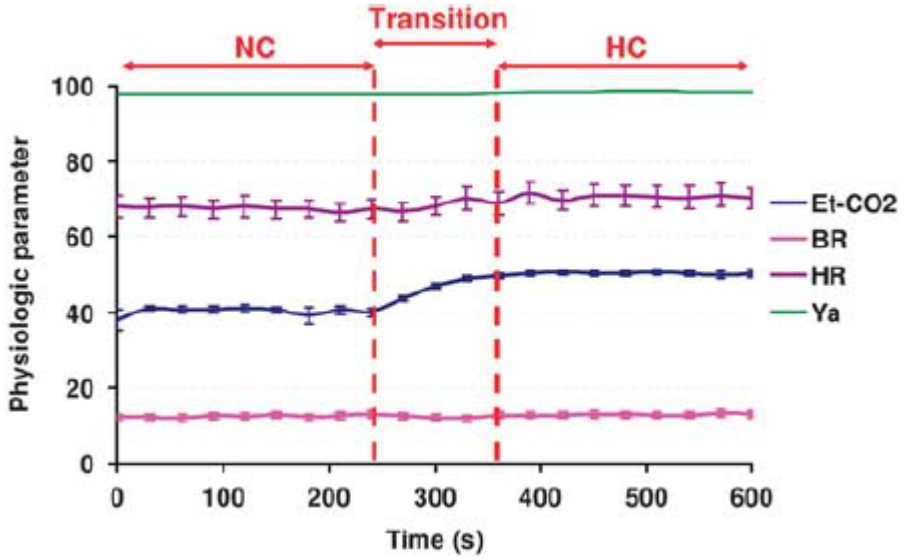

Figure 31 Time-courses of physiologic parameters under normocapnia and hypercapnia conditions.
End-tidal (Et) CO_2, heart rate (HR), breathing rate (BR) and arterial oxygenation (Y_a), were monitored and recorded during the $CMRO_2$ experiments. After the gas valve was switched to the CO_2 mixture, the first two minutes were considered as a transition period, during which no MRI measurements were made. Error bars indicate standard errors of mean across subjects (N=14). Hypercapnia resulted in an increase in Et-CO_2, HR and Y_a ($p<0.05$). BR did not show a significant change.

Once Y_a, Y_v, and CBF were obtained, $CMRO_2$ was calculated from these variables using . The $CMRO_2$ values during normocapnia and hypercapnia were compared using a paired Student t test. A p value of less than 0.05 was considered statistically significant.

A sham control study was conducted in a group of healthy subjects (N=10, age 28.7±5.7 6 males, 4 females), in which the subject was given the same instruction as the real CO_2 study (they were told that they will inhale CO_2) but the gas valve was on room-air for the entire duration of the experiment. This was

conducted to rule out the possibility that the observed $CMRO_2$ change in the CO_2 breathing task was due to mental stress or the subject becoming anxious, drowsy, and/or sleepy after being inside the magnet. All other procedures and MRI scans were identical to the real CO_2 study.

Functional connectivity MRI (fcMRI)

FcMRI scans were performed while the subjects fixated on a crosshair. For comparison, a visual-task fMRI using a flashing checkerboard was also performed. The imaging parameters for the fcMRI scan were: FOV=220×220mm^2, matrix size =64×64, number of slices=33, slice thickness=3mm (gap 1mm), TR/TE=1500ms/25ms, and number of image volumes=200. The visual fMRI employed a fixation of 39s followed by three cycles of checkerboard stimulation (21s, 5Hz) and crosshair (39s). The imaging parameters were identical to those of the fcMRI except that the number of image volumes =146. Each scan was performed twice, first under a normocapnia condition and the other under a hypercapnia condition. Similar to the $CMRO_2$ studies, I waited for 2 minutes to allow a transition between normocapnic and hypercapnic conditions.

I used AFNI (NIMH Scientific and Statistical Computing Core, Bethesda, MD) and in-house Matlab scripts for fcMRI and visual fMRI data processing. For the visual task fMRI data, maps of BOLD percentage changes were generated for each subject using a linear regression between the signal time course and the

stimulation paradigm convolved with a hemodynamic function. Then, a group analysis was performed on the BOLD percentage map to identify visual cortex ROI (threshold: $p<0.005$, cluster size > 2.7 cm^3). The visual cortex ROIs were generated for each of the normocapnia and hypercapnia conditions and the respective activation volume was quantified. The two ROIs were combined to generate an overlapping area that is activated in both conditions. The cc value between the time-course in the overlapping area and the fMRI paradigm was calculated. The fMRI signal, S_{fmri}, in the overlapping voxels was calculated for normocapnia and hypercapnia conditions.

The steps of the fcMRI processing followed those described by Hong et al. (Hong *et al* 2009). Briefly, each data set was preprocessed with slice timing correction, motion correction (realignment), removal of the linear trend, transformation to standard Talairach space (matrix=61×73×61, resolution= 3×3×3 mm^3), and smoothing by a Gaussian filter with a full-width-at-half-maximum (FWHM) of 6 mm. The fcMRI data was then analyzed using a seed-based approach to identify the resting state networks. Low-pass filtering (cut off frequency = 0.1Hz) was applied to the preprocessed signal time course on a voxel-by-voxel basis. Cardiac and respiratory pulsation effects were removed using the respiratory belt and pulse sensor that are integrated into the MRI system. The fluctuations of end-tidal CO_2 (Et-CO_2) and the whole brain averaged fMRI signal were also removed from the subject's voxel time course. For the DMN,

seed ROIs (size=0.73 cm^3) were positioned at bilateral posterior cingulate cortices based on Talairach coordinates. The cross-correlation coefficient (cc) between these seed voxels and all other voxels was calculated to generate a correlation map. Then, a Fisher-z transform was employed and a group analysis was performed on the z-maps of all subjects to identify the DMN (threshold: $p<0.005$, single cluster size > 2.7 cm^3). The data sets from normocapnia and hypercapnia conditions were analyzed separately.

Three fcMRI indices were compared between the normocapnia and hypercapnia conditions. An index of volume of correlated clusters (referred to as "cluster volume" for simplicity) was defined as the total number of voxels that are significantly correlated with the seed ROI (excluding the voxels in the seed cluster). The cc between the seed voxels and the voxels delineated in the correlated clusters was calculated. To avoid the confounding effect of volume differences between normocapnia and hypercapnia, only the voxels that were detected in both conditions (i.e. overlapping voxels) were included in the cc analysis. As a third index, the amplitude of fcMRI signal fluctuation was calculated. Since there is not a ubiquitously defined parameter for fcMRI amplitude, we used an index that is equivalent to the percentage signal change in conventional fMRI. The fcMRI signal, S_{fcmri}, is defined as follows. Let x and y be the time-courses of seed voxels and the voxels in the correlated clusters in fcMRI. Then, S_{fcmri} is calculated by a linear regression on: $y' = S_{fcmri}\, x'$, where

$x' = \frac{x - \text{mean}(x)}{2\|x - \text{mean}(x)\|/\sqrt{n_{dyn}}}$ and $y' = \frac{y - \text{mean}(y)}{\text{mean}(y)}$. In this expression, "mean" indicates the mean signal intensity of the time-course, n_{dyn} is the number of points in the time-course, and the operator ||•|| indicates 2-norm. A desirable feature of this index is that, if we apply this calculation to a conventional fMRI data set with the voxel time-course as *y* and the fMRI paradigm as *x*, the resulting value would be exactly the same as BOLD percentage change obtained from a typical fMRI general linear model (GLM) analysis. Using this index, the CO_2 effect on fcMRI signal can be feasibly compared to that on visual-evoked fMRI signal.

It should be noted that these hypercapnia-induced decreases in fcMRI signal may be caused by a combined effect of CO_2 on neural function (denoted by T) and on basal vascular state (denoted by V) (Cohen *et al* 2002), which has a modulatory effect on BOLD signal amplitude. Therefore, a normalized fcMRI signal amplitude (calculated for each individual) is defined as, $S_{fcmri,n}=S_{fcmri}/S_{fmri}$, where a visual-evoked fMRI, $S_{fmri,}$, is used as a reference to eliminate the vascular effect from fcMRI signal. This calculation assumed that differences in S_{fmri} between normocapnia and hypercapnia were primarily due to vascular effect of CO_2. Previous studies have shown that visual-evoked neural response is minimally affected by the CO_2 level (Jones *et al* 2005; Zappe *et al* 2008b) (although the baseline neural activity may be altered). That is, the visual fMRI signal difference between the normocapnia and hypercapnia conditions is solely

due to basal vascular changes. The fMRI signal can be considered as a product of three factors: relative changes in neural activity, basal vascular parameter (termed the M factor in Hoge et al. (Hoge *et al* 1999) and a constant related to field strength, echo time, etc (Davis *et al* 1998; Hoge *et al* 1999). Thus, $S_{fcmri}=C\times T_{fcmri}\times V_{fcmri}$, and $S_{fmri}=C\times T_{fmri}\times V_{fmri}$. Since the fMRI and fcMRI signals are acquired during the same vascular state, the V terms will cancel out so $S_{fcmri,n}$ becomes $S_{fcmri}/S_{fmri}=T_{fcmri}/T_{fmri}$. When assuming visual-stimulation-induced T_{fmri} is identical between normocapnia and hypercapnia states (Jones *et al* 2005; Zappe *et al* 2008a), $S_{fcmri,n}$ would result in $T_{fcmri,\ hypercapnia}/T_{fcmri,\ normocapnia}$, a relative comparison of the resting state neural activities between normocapnia and hypercapnia. Therefore the normalized fcMRI signal would mainly convey whether the CO_2 alter baseline spontaneous neural activity.

In addition to the DMN, sensorimotor regions were also identified from the fcMRI data. The seed regions were positioned in the right motor cortex and the voxels correlating with the seed time course were identified. We have also tested using the left motor cortex for seed regions and the results were similar. Comparison was made between normocapnia and hypercapnia conditions.

Electroencephalogram (EEG)

I used a 64-channel SynAmps II EEG system (NeuroScan, Charlotte, NC), which included an EEG cap on which the geometric locations of the electrodes

are preset. Saline was applied in each electrode to ensure proper electrode conduction, the impedance of which is monitored on a computer screen. To avoid mechanical pressure on the electrodes, these experiments were conducted with subject sitting upright, unlike the MRI experiments in which the subjects were at supine position. I assumed that the CO_2 effect, if any, is comparable between these two body positions. The subjects were instructed to keep their eyes open and fixate on a white cross throughout the experiments. This control of eye fixation is important as it can change the EEG power spectra (Kiloh et al 1972).

The experiments were conducted for 17 minutes during which time the subjects were breathing room air for 5 minutes, switched to the 5% CO_2 gas mixture for 7 minutes and then returned to room air for the final 5 minutes. EEG recordings were made continuously during this 17 minute period. The EEG data from the first and second normocapnia periods were combined to yield an interpolated signal that will be compared to the signal of the hypercapnia period. The interpolation computation was necessary to correct for linear trends, hysteresis, and rebound effects in the recordings (Zappe *et al* 2008b), which could cause a signal drift over time.

The data were recorded with a reference electrode located near the vertex, resulting in small amplitudes over the top of the head. To eliminate this effect, the data were re-referenced to the average potential over the entire head, which approximates the voltages relative to infinity. In order to reduce a slight bias in

the electrode-based average reference, spherical splines were fit to the data and used to compute the average.

The raw 64-channel EEG signals were recorded at a rate of 1000 samples per second. Pre-processing of the EEG signal was done in Scan v4.3 (Neuroscan, Inc). High-pass filtering was applied with a cutoff frequency of 0.15 Hz and a roll off attenuation factor of 12dB/octave. Next, artifacts associated with eye blinking were removed from the raw EEG time courses. NeuroScan uses the principal-components-analysis (PCA) method to estimate the characteristic waveform of eye blinking and then performs subtractions from the raw EEG recordings. Three data segments were extracted from the EEG recording: first room air period (5 min), stabilized hypercapnia period (5 min after excluding the transition period), and stabilized second room air period (3 min after excluding the transition period). The signals within each segment were further divided to 1 second epochs. Visual inspection was conducted to exclude epochs with signal artifacts.

The post-processing was performed using Matlab in conjunction with an EEG analysis toolbox, EEGLab. Each segment was linearly detrended, mean subtracted, and cosine tapered. Fourier transform was applied to each epoch, and spectrum power density (square of Fourier coefficient magnitude) from 1 to 100Hz was computed in the unit of $\mu v^2/Hz$. The power spectra were then averaged over the epochs to yield a final power spectrum for each segment. The

powers from the first room air and the second room air were interpolated based on the acquisition timing.

Power spectra of three frequency bands were investigated based on well-establish frequency definition: 1-3 Hz for delta band, 4-7 Hz for theta band, and 8-13 Hz for alpha band (Kiloh *et al* 1972). The analysis was performed for each of the channels as well as for the average of all channels.

4.2.4 Results

Inhalation of 5% CO_2 increased the subjects' end-tidal CO_2 (Et-CO_2) from 41.3±0.8 mmHg (N=14, 9 males and 5 females, mean±SEM) to 50.1±0.7 mmHg ($P<0.001$). Figure 32a shows representative TRUST MRI data for the normocpania and hypercapnia conditions. The MR T_2 signal decay is much slower during hypercapnia, suggesting a longer venous blood T_2. Accordingly, venous oxygenation, Y_v, was found to increase significantly (paired t test, $P<0.001$) from normocapnia to hypercapnia (Table 4). Arterial oxygenation (Y_a) measured by Pulse Oximeter showed a negligible change between the two conditions (Table 4). Thus the oxygen extraction fraction (OEF), i.e. Y_a-Y_v, reduced considerably (Table 4). Figure 32b shows representative phase-contrast MRI results. One can see a clear increase of flow velocity as indicated by darker pixel intensity (arrows). Quantitative analysis revealed that CBF increased significantly from normocapnia to hypercapnia ($P<0.001$). Table 4 summarizes the values of the physiologic parameters during normocapnia and hypercapnia

conditions. The relative changes are plotted in Figure 32c. $CMRO_2$ was found to show a reduction of 13.4±2.3% comparing hypercapnia to normocapnia ($P<0.001$). That is, in addition to the pronounced vascular effect, high CO_2 content also modestly reduces tissue's metabolic rate. In the sham study, $CMRO_2$ values during the baseline and sham control periods were 977.6±88.5 μmol/min and 995.4±89.4 μmol/min, respectively, and did not show a difference ($P=0.34$, paired t test, N=10) (Table 5) .

I further hypothesized that CO_2 has a dose dependent effect on $CMRO_2$ where an individual with a smaller Et-CO_2 change during the hypercapnic phase will have a smaller change in $CMRO_2$ and vice versa. Figure 33 shows a scatter plot between Et-CO_2 change and $CMRO_2$ change across the 14 subjects studied. A significant correlation ($P=0.014$) was observed.

Figure 34 shows DMN in both the normocapnia and hypercapnia conditions identified from the fcMRI data (N=14). DMN under normocapnia condition (Figure 34a) clearly illustrates the connectivity among posterior cingulate cortex (seed region), bilateral inferior parietal regions, medial prefrontal cortex and medial temporal lobe. In contrast, cluster volume under hypercapnia condition (Figure 34b) shows a drastic reduction. Similarly, the cc values between the seed region and the other DMN regions were reduced significantly (paired t-test $P=0.024$) comparing hypercapnia to normocapnia. The amplitude of fcMRI signal also showed a reduction by 37.2% due to hypercapnia ($P=0.001$). The

application of similar analysis to the visual fMRI data revealed that the activation volume, cc and fMRI signal amplitude were reduced by 13.5%, 2.4% and 22.1%, respectively, when comparing results under hypercapnia to that under normocapnia (Table 6). All indices showed smaller hypercapnia-induced changes compared to those in the fcMRI data. The normalized fcMRI signals were 0.29±0.03 and 0.23±0.02 for normocapnia and hypercapnia, respectively, showing a 20.1% reduction (P=0.020). In addition to the DMN brain regions, we have studied the sensorimotor regions, which also have a well-defined resting state network (Biswal *et al* 1995; Xiong *et al* 1999). Reductions similar to that observed for the DMN were observed comparing hypercapnia to normocapnia (Table 7, Figure 35).

EEG recordings with scalp electrodes were compared between normocapnia and hypercapnia conditions (N=12). Table 8 shows the EEG signal power in delta band (1-3 Hz), theta band (4-7 Hz) and alpha band (8-13 Hz) under normocapnia and hypercapnia conditions. The signal power was significantly increased in the delta band (P=0.049), accompanied by a significant decrease in the alpha band (P=0.003) (Figure 36). The theta band power did not show a significant change. Therefore, the relative EEG power was shifted toward the lower frequency range, a typical pattern of reduced brain arousal state (Kiloh *et al* 1972). Figure 37 shows the topographic maps of EEG power in different frequency bands during normocapnia and hypercapnia conditions, as well as the

power ratio. The data suggest that the slowing of the EEG signal appeared to be present in all electrodes across the entire brain. I have also studied frequency ranges beyond 13 Hz (e.g. beta band, gamma band), but the signal was small and statistical comparisons did not yield significant differences between the two conditions.

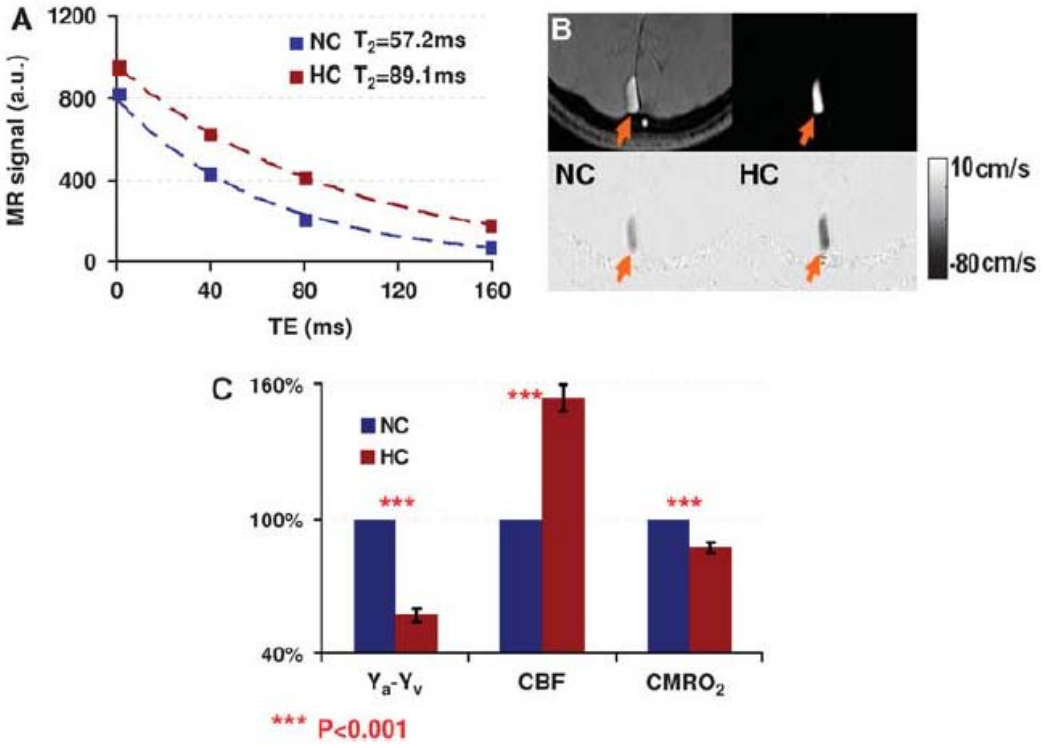

Figure 32 MRI measurement of $CMRO_2$ under normocapnia and hypercapnia conditions. (a) Venous oxygenation, Y_v, used in the $CMRO_2$ calculation was measured with a TRUST MRI technique. MR signal in the venous blood was measured as function of TE. The decay time constant is the blood T_2, which can be converted to blood oxygenation. The time constant during hypercapnia (HC, red) is longer than that in normocapnia (NC, blue). (b) Cerebral blood flow (CBF) used in the $CMRO_2$ calculation was measured with phase-contrast MRI applied in the sagittal sinus. The four images are: raw image, magnitude image, velocity map during NC, and velocity map during HC. Arrows indicate the sagittal sinus. In the velocity maps, the darker color indicates higher outflow velocity. (c) Summary of CO_2-induced changes in Y_a-Y_v, CBF and $CMRO_2$ (N=14). The parameter values under normocapnia were set as 100%. The values under hypercapnia condition were presented relative to the normocapnia values.

	Y_v	Y_a	Y_a-Y_v	CBF (ml/min)	$CMRO_2$ (μmol/min)
NC	0.624± 0.017	0.979± 0.003	0.355± 0.067	352.8± 16.8	1042.3± 76.1
HC	0.782± 0.014	0.985± 0.002	0.203± 0.055	547.1± 35.6	899.0± 66.1
Relative change	26.1%	0.6%	-42.6%	54.5%	-13.4%
P value (paired t-test)	<0.001	<0.001	<0.001	<0.001	<0.001

NC: normocapnia; HC: hypercapnia

Table 4 Summary of vascular and metabolic parameters under normocapnia and hypercapnia conditions.

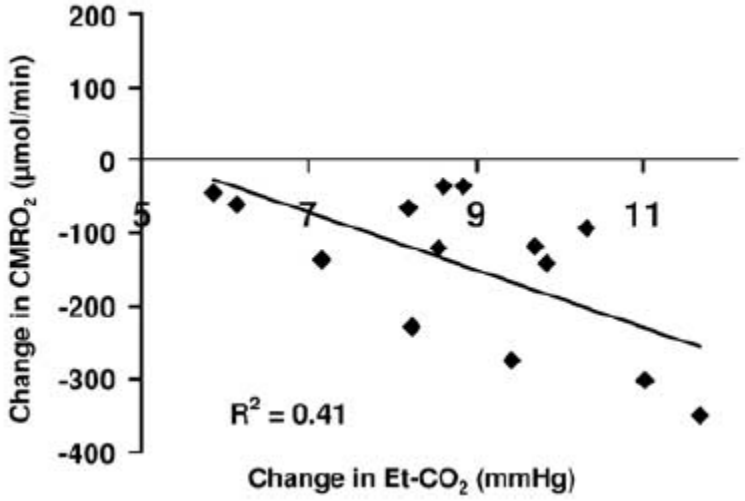

Figure 33 Scatter plot between hypercapnia-induced Et-CO_2 change and $CMRO_2$ change across subjects (N=14).

Inhalation of 5% CO_2 caused an increase in Et-CO_2 and a decrease in $CMRO_2$ in all subjects studied. Different subjects have slightly different Et-CO_2 change. Individuals with a greater Et-CO_2 change tended to have a greater $CMRO_2$ change (P=0.014), suggesting a dose-dependent effect of CO_2 on brain metabolism.

	Y_v	Y_a	CBF (ml/min)	CMRO2 (μmol/min)
NC	0.616± 0.027	0.978± 0.004	325.8±13.7	977.6±88.5
Sham HC	0.621± 0.024	0.975± 0.003	337.6±13.6	995.4±89.4
Parameter ratio (Sham HC/NC)	1.01± 0.02	0.997± 0.006	1.05±0.05	1.03±0.05
P value (t-test)	0.33	0.09	0.18	0.34

NC: normocapnia; HC: hypercapnia

Table 5 Summary of vascular and metabolic parameters during the sham control experiment

	$EtCO_2$ (mmHg)	Cluster volume (ml)		Correlation coefficient		Signal amplitude (%)		
		DMN fcMRI	Visual fMRI	DMN fcMRI	Visual fMRI	DMN fcMRI	Visual fMRI	Normalized fcMRI
NC	40.2± 0.7	120.4	206.9	0.67± 0.03	0.69± 0.04	0.29±0.02	1.02± 0.07	0.29± 0.03
HC	47.4± 0.7	54.3	178.9	0.55± 0.05	0.68± 0.03	0.18± 0.02	0.80± 0.08	0.23± 0.02
Relative change	18.0%	-54.9%	-13.5%	-17.6%	-2.4%	-37.2%	-22.1%	-20.1%
P-value (paired t-test)	< 0.001	N/A*	N/A*	0.024	0.30	0.001	0.018	0.020

NC: normocapnia; HC: hypercapnia

DMN: default mode network

*This index was obtained from a group analysis, thus the value does not have a standard deviation or an associated P-value.

Table 6 Summary of resting-state default mode network parameters during normocapnia and hypercapnia.

For comparison, visual-evoked fMRI results are also shown.

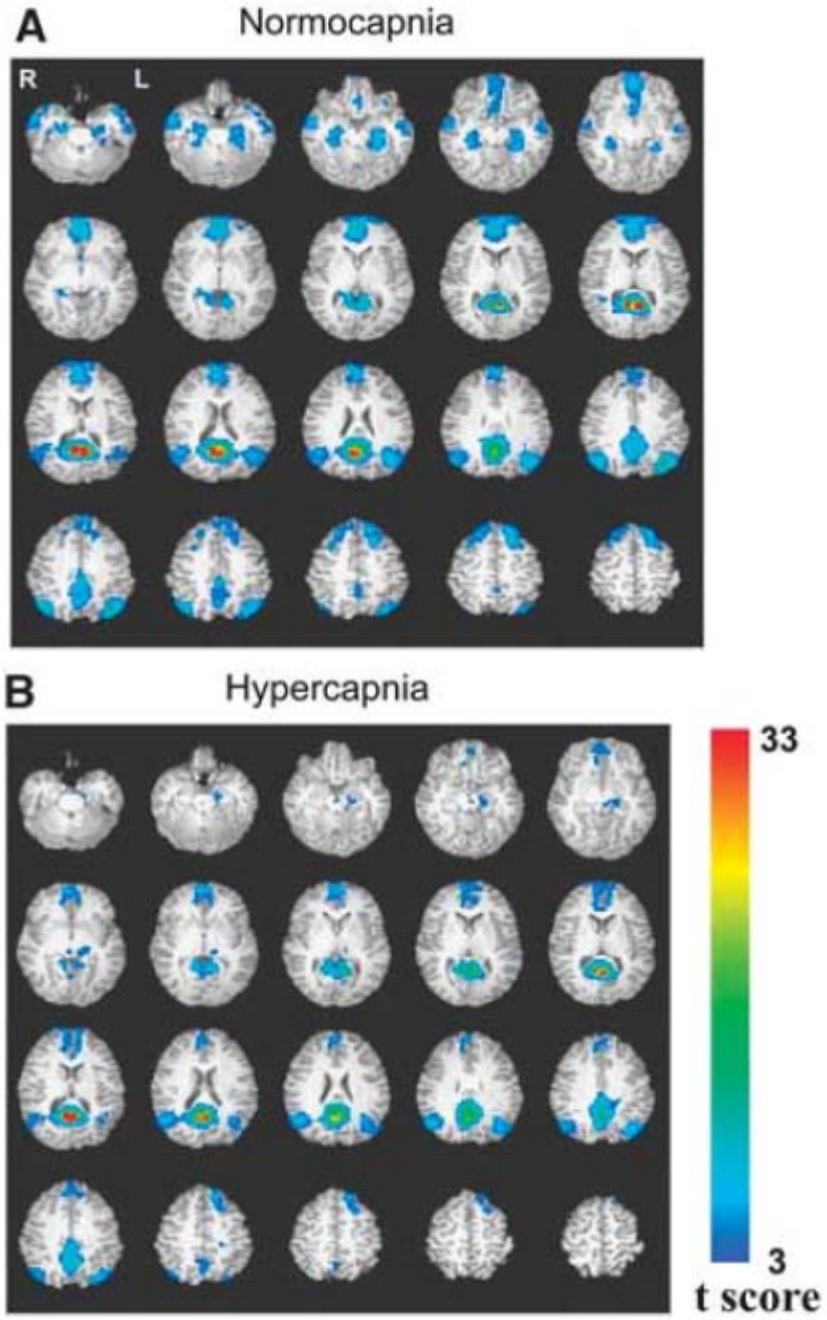

Figure 34 Resting state Default Mode Network (DMN) under normocapnia and hypercapnia conditions (N=14).

The DMN regions consist of posterior cingulate cortex, bilateral inferior parietal cortex, medial frontal cortex and bilateral medial temporal lobe, as defined by many previous studies. Hypercapnia resulted in a significant reduction in the size of the cluster volume.

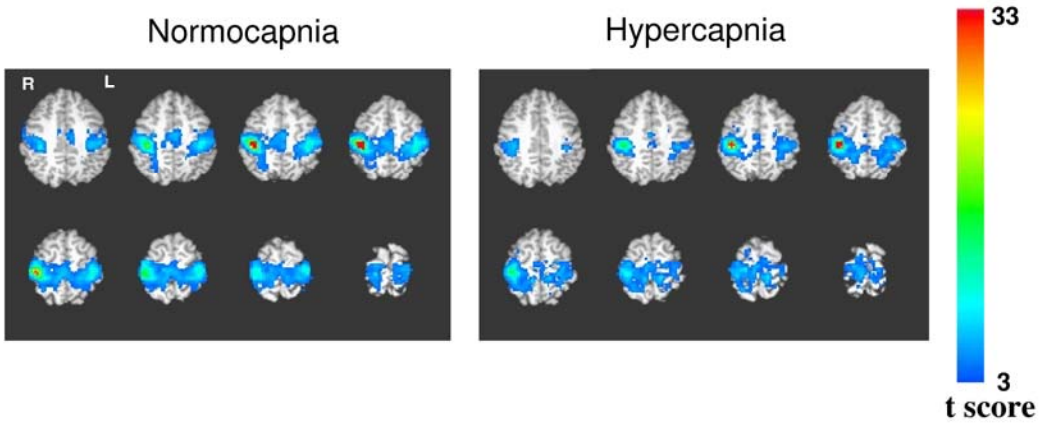

Figure 35 Resting state Motor Network under normocapnia and hypercapnia conditions (N=14).

	EtCO2 (mmHg)	Activation volume (ml)		Correlation coefficient		fMRI signal (%)	
		Sensory motor fcMRI	Visual fMRI	Sensory motor fcMRI	Visual fMRI	Sensory motor fcMRI	Visual fMRI
NC	40.2± 0.7	57.3	206.9	0.61± 0.06	0.69± 0.04	0.22± 0.04	1.02± 0.07
HC	47.4± 0.7	34.3	178.9	0.43± 0.06	0.68± 0.03	0.11± 0.03	0.80± 0.08
Relative change	18.0%	-40.2%	-13.5%	-29.4%	-2.4%	-49.4%	-22.1%
P-value (paired t-test)	< 0.001	N/A	N/A	0.017	0.30	0.013	0.018

NC: normocapnia; HC: hypercapnia

Table 7 Summary of sensorimotor network parameters under normocapnia and hypercapnia conditions.

For comparison, visual-evoked fMRI results are also shown.

Frequency band	Delta	Theta	Alpha
Frequency range	1~3	4~7	8~13
Normocapnia power (μV^2)	6.4±0.7	6.4±0.9	10.2±2.1
Hypercapnia power (μV^2)	7.6±1.1	6.3±1.0	8.1±1.8
Ratio between Hypercapnia power and Normocapnia power	1.16	0.99	0.84
P value	0.049	0.440	0.003

Table 8 EEG power in different frequency bands under normocapnia and hypercapnia conditions.

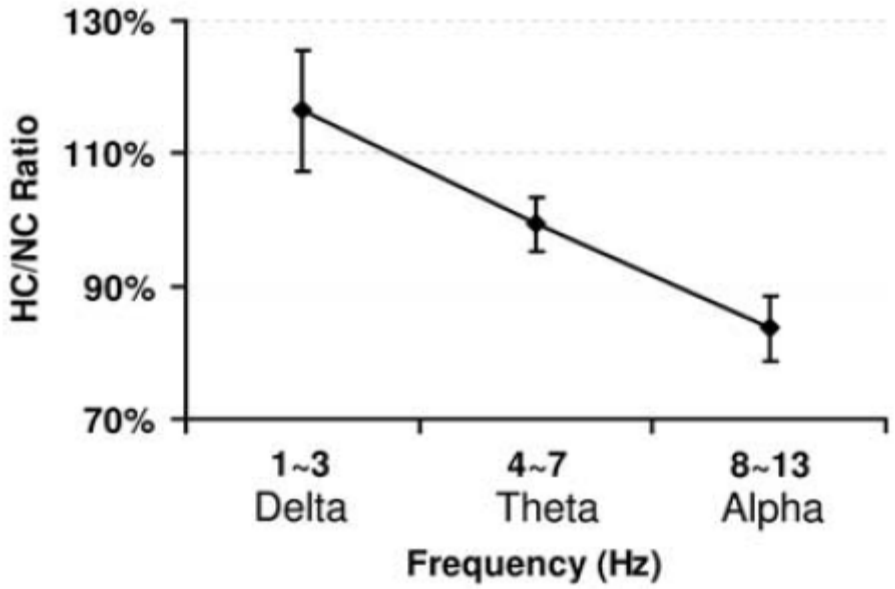

Figure 36 Relative changes in EEG signal power comparing hypercapnia to normocapnia. The powers under normocapnia condition were set as 100%. Hypercapnia resulted in a slowing of the EEG power spectra, with delta band (1-3 Hz) showing a power increase and alpha band (8-13 Hz) showing a decrease.

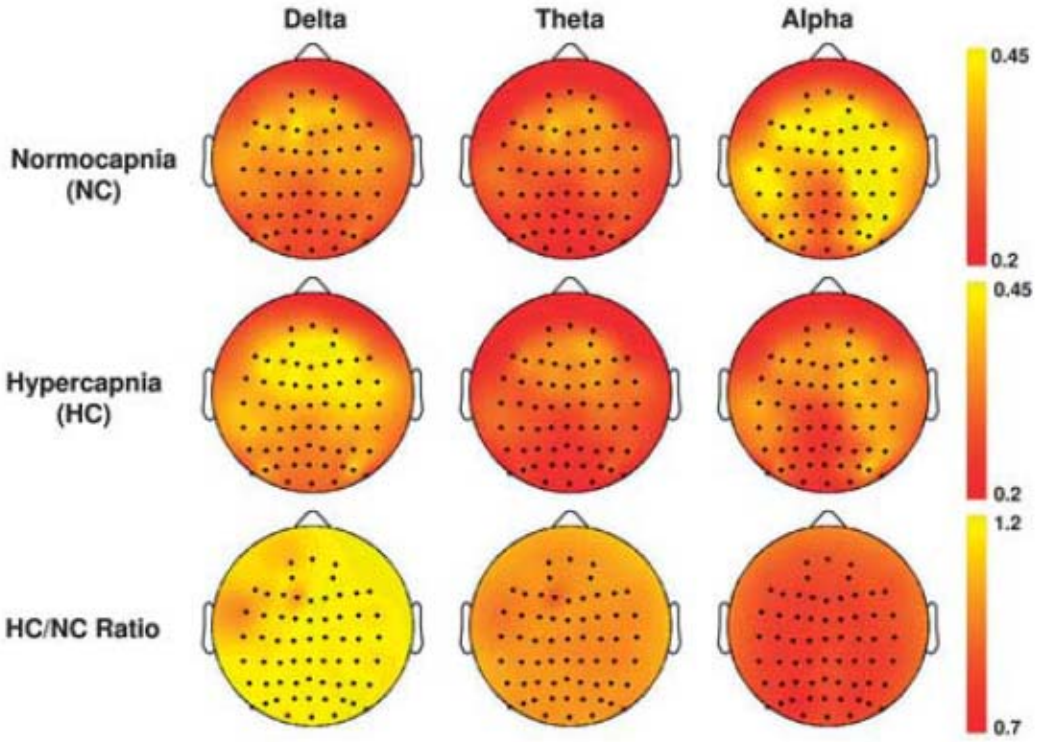

Figure 37 Topographic maps of EEG signals under normocapnia and hypercapnia conditions (N=12).
The EEG signal power was calculated for each frequency band. In the topographic maps, the nose of the subject is on the top, illustrated by the triangle. The ears are illustrated by the rectangles. Each black dot indicates one electrode. The bottom row shows the ratio between hypercapnia and normocapnia signals. It can be seen that the delta power increased during hypercapnia whereas the alpha power decreased. The theta power remained unchanged. From the ratio map, it can also be seen that hypercapnia-induced changes affected all electrodes. The maps shown were averages of all subjects studied. Before averaging, the EEG power of each subject was normalized to the electrode-averaged power under normocapnia, so that the variations in EEG signal power (e.g. due to differences in scalp thickness) between subjects are accounted for.

4.2.5 Discussion

The present study investigated the effect of blood CO_2 levels on brain activity from a number of perspectives. I first showed that hypercapnia reduced metabolic activity in the brain. Second, neural activity was assessed indirectly by BOLD fcMRI and the data suggested that CO_2 inhalation caused a decrease in

spontaneous brain connectivity. Finally, EEG was used as a direct measure of neural activity and the results showed that hypercapnia caused a relative increase in lower frequency power spectra. Overall, our data showed a suppressive effect of CO_2 on brain activity.

The findings from the present study are in general agreement with earlier studies conducted in animals. In a study of macaque monkeys under anesthesia, Zappe and colleagues reported that hypercapnia induced a 15% reduction in resting state multi-unit neural activity in the primary visual cortex (Zappe *et al* 2008b). While the authors did not investigate other brain regions in the study (personal communications), previous literature suggests that this depression effect is likely to be global (Kliefoth *et al* 1979). Our study represents the first systematic investigation of this effect in conscious humans and suggests that resting state neural activity is reduced due to mild hypercapnia. Further, I showed that this suppression of neural activity is accompanied by a reduction in metabolic activity of similar amplitude.

A number of studies in the literature have compared $CMRO_2$ between normocapnia and hypercapnia conditions. Our finding of a 13% decrease is in general agreement with the reports by Kogure et al. (1975) (-15%), Sicard and Duong (2005) (-10%), Barzilay et al. (1985) (-15%), and Klifoth et al. (1979) (-30%), but is inconsistent with those reported by Kety and Schmidt (1948) (+3%), Novack et al. (1953) (0%), Yang and Krasney (1995) (+17%), and Horvath et al.

(1994) (+35%). Possible reasons for the discrepancy include different measurement techniques, different species and the effect of anesthetic agent. Specifically, only the earlier studies by Kety and Schmidt (1948) and by Novack et al. (1953) used human subjects, and the more recent studies all used animal subjects under anesthesia. It is known that anesthetic agent itself may affect neural activity and metabolism (Shulman *et al* 1999).

A change in $CMRO_2$ due to hypercapnia also has important implications for calibrated fMRI. Calibrated fMRI is an approach to obtain quantitative changes in brain metabolism during neural activation (Chiarelli *et al* 2007a; Davis *et al* 1998; Kim and Ugurbil 1997). This technique often uses CO_2 inhalation to determine the calibration factor and assumes that mild hypercapnia does not alter $CMRO_2$. In the case that CO_2 does cause a decrease in $CMRO_2$, the theoretical framework of calibrated fMRI will remain valid but the processing of experimental data should be adjusted slightly. Specifically, the M factor in calibrated fMRI will become lower, the estimated $CMRO_2$ will be smaller, and the $CBF/CMRO_2$ coupling factor n will be greater. Interestingly, these trends will shift the MRI results to become more comparable to earlier reports using PET (Fox and Raichle 1986).

Our observation of a reduced functional connectivity during CO_2 breathing is consistent with previous reports that light sedation (Greicius *et al* 2008) or anesthesia (Deshpande *et al*) decreases connectivity in DMN regions,

and is also in line with suggestions that CO_2 has a mild sedative effect (Fukuda *et al* 2006). The CO_2-induced reduction in sensorimotor connectivity is also in good agreement with a previous report by Biswal and colleagues (Biswal *et al* 1997). In our study, we have taken special precaution to minimize the influence of basal vascular state on BOLD signals, which were not accounted for in previous studies comparing fcMRI data across physiologic states (Biswal *et al* 1997; Deshpande *et al*; Greicius *et al* 2008; Horovitz *et al* 2009). We have used visual-evoked fMRI signal as a reference with the assumption that the alterations in fMRI signal is solely due to a change in vascular state (Jones *et al* 2005; Zappe *et al* 2008a). While this referencing strategy is still based on assumptions and biophysical models (Davis *et al* 1998; Jones *et al* 2005; Zappe *et al* 2008a), it nonetheless provides an additional level of control for non-neuronal effect and is the best available technique to our knowledge. Our results demonstrated that the "normalized" fcMRI signal still showed a significant decrease due to hypercapnia, suggesting that some of the fcMRI signal reduction is of neuronal origin.

In this study, I found a relative increase in low frequency EEG power spectra upon inducing hypercapnia. It is known that EEG frequency is highly dependent on the physiologic state of an individual (Kiloh *et al* 1972). If the brain is in a high arousal state (e.g. conversation, thinking), the EEG power spectra show a relative increase in higher frequencies, whereas if the brain is in a low arousal state (e.g. relaxing, drowsy, sleepy, day dreaming) lower frequencies

predominate. Our data suggests that during hypercapnia the brain's electrical activity resembles lower arousal states. This finding is consistent with reports that mild hypercapnia may improve the duration and efficiency of sleep (Fraigne *et al* 2008).

The findings from the three complementary techniques are consistent with each other. Our observation that a lower metabolic state corresponds to a slower EEG signal is in agreement with reports by Maandag et al. that neurons under low metabolic state have a slower oscillation frequency (Maandag *et al* 2007). The relationship between fcMRI and EEG signals has also been studied by a number of investigators and the majority of the reports appear to suggest that fcMRI signal has a correlation with alpha power in the EEG (Mantini *et al* 2007; Moosmann *et al* 2003). Thus our observation of a concomitant reduction in fcMRI signal and alpha power during hypercapnia is in general agreement with this notion. Another evidence of a link between fcMRI and EEG comes from studies employing simultaneous EEG-fcMRI recordings during sleep (Horovitz *et al* 2009). It has been shown that a slowing of EEG (i.e. greater delta power) is accompanied by reduced functional connectivity among selective DMN regions (Horovitz *et al* 2009). However, it is not straightforward to directly compare our findings of CO_2 effects to deep sleep, because the neural activity changes during sleep are likely more complex than those due to CO_2 inhalation.

The mechanism of the observed suppression of neural activity is not clear. A few in vitro studies suggested that it may be related to tissue acidosis when carbonic acid is formed from CO_2 and water. In a study using brain slices, Dulla and colleagues found that increased CO_2 pressure reduces pH in the extracellular space, which increases the extracellular adenosine concentration (Dulla *et al* 2005). Gourine et al. suggested that ATP release may be involved in the CO_2 sensing pathways (Gourine *et al* 2005).

The neural suppression effect of CO_2 is also consistent with reports that exposure to hypercapnia can terminate epileptic bursting. In laboratory settings, CO_2 breathing has also been shown to terminate some epileptic seizure activity (Dulla *et al* 2005). In addition, acetazolamide, sold under the trade name "Diamox", is a carbonic anhydrase inhibitor and increases CO_2 pressure in the blood. This drug is commonly used as a vasodilator in the assessment of vascular reserve and cerebrovascular function. Interestingly, acetazolamide is also an anti-epileptic drug that is used to treat certain types of epilepsy (e.g. absence epilepsy, myoclonic seizure, catamenial epilepsy) (Levy *et al* 1995). Intake of acetazolamide and inhalation of CO_2 have virtually the same effect and are often considered the same physiologic challenge in the cerebrovascular literature. Therefore, it is reasonable to expect that CO_2 inhalation may also have an anti-epileptic effect. Another line of supporting evidence for the CO_2 effect is that

hyperventilation causes hypocapnia, and has been known to induce interictal spike-and-wave activity (Niedermeyer and da Silva 2005).

In the previously mentioned calculation of $CMRO_2$, I have only considered oxygen bound to hemoglobin but did not account for oxygen that is dissolved in the plasma. This assumption is considered reasonable in our experiments because the majority (>98%) of the oxygen molecules carried by the blood is in the form of hemoglobin-bound oxygen. To confirm this point, I have incorporated an oxygen sensor in our gas apparatus and measured end-tidal (Et) O_2 pressure in four subjects outside the MRI room. This showed that Et-O_2 under normocapnia and hypercapnia conditions were 114.7±3.1 mmHg and 136.6±2.3 mmHg, respectively. The difference is presumably due to hyperventilation when the subject breathes CO_2. By estimating the amount of dissolved oxygen from Et-O_2 (Guyton and Hall 2005), $CMRO_2$ during normocapnia and hypercapnia was re-calculated and the results still showed a reduction of $CMRO_2$ by 10.4±2.2%.

In summary, our findings suggest that increased CO_2 levels cause the brain to reduce metabolism and spontaneous neural activity, and enter a lower arousal state.

4.2.6 Conclusion

This series of experiments demonstrate that hypercapnia suppresses baseline neural activities in various ways, such as oxidative metabolism, spontaneous neural activity and the arousal state.

4.3 The effect of graded O_2 on vascular and metabolic parameters

4.3.1 Abstract

A better understanding of O_2 effect on the brain activity may have a profound impact on the oxygen therapy in clinical settings and on the use of hyperoxia as a means to calibrate fMRI signal. The present study investigates whether changing the O_2 tension in the blood stream would affect the brain metabolism. Dynamic measurements of the cerebral metabolic rate of oxygen ($CMRO_2$) revealed that mild hypoxia increased $CMRO_2$ while hyperoxia resulted in suppression. The "paradoxical" founding suggests that the brain's oxidative metabolism is independent from its supply.

4.3.2 Introduction

The effect of O_2 on the brain vascular function and metabolism has always been of interest to physiology and clinical researchers. Relevant studies can be applied to people living at high attitudes, astronauts spending time in the space, climbers having mountain sickness, and the patients receiving oxygen therapy for traumatic brain injury (Magnoni *et al* 2003), cerebral palsy (Rosenbaum 2003), etc. In order to apply oxygen therapy effectively and explain the effect of hypoxia and hyperoxia, we need to have better understanding the basic question that how the brain metabolism responses to the altered blood O_2 tension.

The O_2 tension in the bloodstream has been found to affect the vasculature, for example, hypoxia increases the cerebral blood flow (CBF) and hyperoxia

suppresses it (Bulte *et al* 2007; Floyd *et al* 2003). In addition, hypoxia is reported to elevate the hematocrit as well as stimulate the angiogenesis, especially in the case of the brain tumor. However, there is no clear evidence of the effect of O_2 on the human brain metabolism, simply because there is not such a technique that can quantify the brain metabolism directly without using the CBF as a surrogate or involving invasive procedures. It is widely assumed in existing literature that altering the blood O_2 tension has no effect on the brain tissue, and so the use of hyperoxic challenge is considered a means to independently modulate the vasculature (Chiarelli *et al* 2007b; Mark *et al* 2011).

With a recent developed MRI technique (Xu *et al* 2009), one can noninvasively investigate the effect of O_2 on the brain's oxidative metabolism. The brain tissue O_2 tension can be regulated via inhaling graded O_2 concentrated gas. The inhaled air alters the blood oxygenation (Y), and then consequently changes CBF. As a result, the O_2 supply to the brain tissue is affected. This study will exam how the $CMRO_2$ responds to the altered O_2 supply caused by acute hypoxia and hyperoxia.

4.3.3 Materials and methods

Participants

Sixteen healthy subjects (26±4years old, 9 males and 7 females) were studied. Each subject gave an informed written consent before participating in the study. The study protocol was approved by the Institutional Review Board of the

University of Texas Southwestern Medical Center. All participants were instructed not to take coffee or tea on the day of experiment to avoid any cocaine effect on metabolism. To maintain a constant state, the participants were allowed to watch a movie to keep awake, and were instructed to keep a uniform breathing pattern through the experiment. This is important because sleep and hyperventilation affect the CBF and brain activity (Braun *et al* 1997; Nofzinger *et al* 2002).

O_2 probation

The graded O_2 gas was stored in three separate Douglas bags, and delivered to the subject's mouth through a two-way non-rebreathing valve (Figure 38a). Hypoxia is induced by the 14% O_2 gas balanced with N_2. Hyperoxic gas is composed by two types of airs: 50% O_2, 1% CO_2 wtih 49% N_2 and 98% O_2 with 2% CO_2. A small fraction of CO_2 was added in hyperoxic gas is tried to maintain a constant Et-CO_2 level. The dose of CO_2 added was based on the response (e.g. ET-CO_2) of three subjects measured outside MRI.

Quantification of $CMRO_2$ for graded O_2 conditions

Again, the measurement of $CMRO_2$ was similar to CO_2 study (Figure 38b) except that the CBF was repeatedly measured by phase-contrast MRI for four times before and after TRUST MRI to minimize the mismatch of CBF during phase-contrast MRI and TRUST MRI shown in Figure 38c. Recordings of Et-CO_2 and Et-O_2 during each scan were used to correct CBF variation since these two

factors regulate the CBF. In addition to Y_a, the CBF was also measured during the transition from one O_2 condition to another (Figure 38c).

At the normoxia, the blood plasma dissolved O_2 is negligible for it only accounts for less than 2% of the hemoglobin bound O_2, while hyperoxia raises the blood O_2 pressure, consequently the dissolved O_2 can go up to 10% of the bond O_2. Subsequently, after account for the dissolved O_2 carried by arterial blood, the $CMRO_2$ by equation is rewritten as following:

Eq.34

$$CMRO_2 = CBF \cdot OEF \cdot C_h = CBF \cdot ([O_2]_a - [O_2]_v) \cdot C_h$$

Eq.35

$$[O_2]_a = (Y_a \cdot C_h + p_aO_2 \cdot C_d)/C_h$$
$$[O_2]_v = (Y_v \cdot C_h + p_vO_2 \cdot C_d)/C_h$$

where CBF is the cerebral blood flow in ml/min, OEF is the O_2 extraction fraction, $[O_2]_a$ and $[O_2]_v$ are the arterial and venous O_2 contents (including both hemoglobin bound and plasma dissolved O_2). C_h (897 μmol O_2/100ml blood) and C_d (0.136 μmol O_2/100ml blood/mmHg O_2 tension) determine the hemoglobin's O_2-carrying capacity and the plasma's O_2-dissolving capacity, respectively. The Y_a and Y_v are the arterial and venous oxygen saturation, i.e. the fraction of hemoglobin bound with O_2. The P_aO_2 and P_vO_2 are the O_2 tension in the blood, in unit of mmHg; $pO_2 \cdot C_d / C_h$ converts the amount of dissolved O_2 per unit blood to an equivalent fraction of bound O_2. So the final index of $[O_2]$ is in fraction (%).

Note that in this study $[O_2]_a$ could reach a value greater than 100% because of the large amount of dissolved O_2 during breathing 50% and 98% O_2.

The CBF was measured with phase contrast MRI, Y_a was determined by a pulse oximetry (MedRed, Pittsburgh, PA); Y_v was estimated with T_2-Relaxation-Under-Spin-Tagging (TRUST) MRI. P_aO_2 is approximated by Et-O_2, which is measured by an oxygen sensor (ANOXL Sensor Technology, Stokesley, North Yorkshire, UK). P_vO_2 is obtained from the blood oxygen dissociation curve based on the measured Y_v. Since the C_h and the Y_v calibration are hematocrit (Hct) dependent, 10ml blood was drawn at arm for each subject to measure Hct. Other physiological parameters including heart rate (HR), breathing rate (BR), end-tidal CO_2 (Et-CO_2) and end-tidal O_2 (Et-O_2) were monitored through the experiment (MedRed, Pittsburgh, PA and Novametrix Medical System, Wallingford, CT).

The sequence parameters were: for TRUST MRI, voxel size 3.44x3.44x5mm^3, TR=8000ms, TI=1200ms, four TEs: 0ms, 40ms, 80ms and 160ms, duration 3.2 min; for PC MRI, voxel size 0.45x0.45x5 mm^3, maximum velocity 80cm/s, duration 30sec.

The arterial blood oxygenation, heart rate and breathing rate was recorded at 1 sample/second, the exhaled CO_2 partial pressure was sampled every 10sec, and the exhaled O_2 partial pressure (ANOXL Sensor Technology, Stokesley, North Yorkshire, UK) was recorded every 30sec. The physiological recordings

were all synchronized with MRI acquisition, and were averaged for corresponding period of the scan.

Data analysis

The TRUST MRI and PC MRI data were analyzed in the same way as previous studies (Xu *et al* 2009; Xu *et al* 2011). The changes of $[O_2]_{a/v}$, CBF and $CMRO_2$ are tested by mix model to correct the repeated measurements across conditions. A p value less than 0.05 after correcting the multiple comparisons is considered significant. In order to eliminate the CO_2 effect, the $CMRO_2$ fractional change is modeled by Et-CO_2 and $[O_2]_a$ changes together. The reason of comparing the relative change is to remove the response variation due to irrelevant factors such as the brain size. The form of linear model is chosen based on the F test for goodness of fit.

4.3.4 Results

As shown in Figure 38c, the $[O_2]_a$ increases and CBF decreases as breathe more O_2. Quantitative values of $[O_2]_a$, $[O_2]_v$, CBF and $CMRO_2$ are listed in the Table 9. The mix-model shows that all parameters are significantly dependent on the inhaled O_2 content ($P<0.001$). To better appreciate the physiology relevant significance, Figure 39 illustrates the changes in the $CMRO_2$ model. As inhale more O_2, the $[O_2]_v$ increases as well as the $[O_2]_a$. Both CBF and $CMRO_2$ show a negative corelation to the O_2.

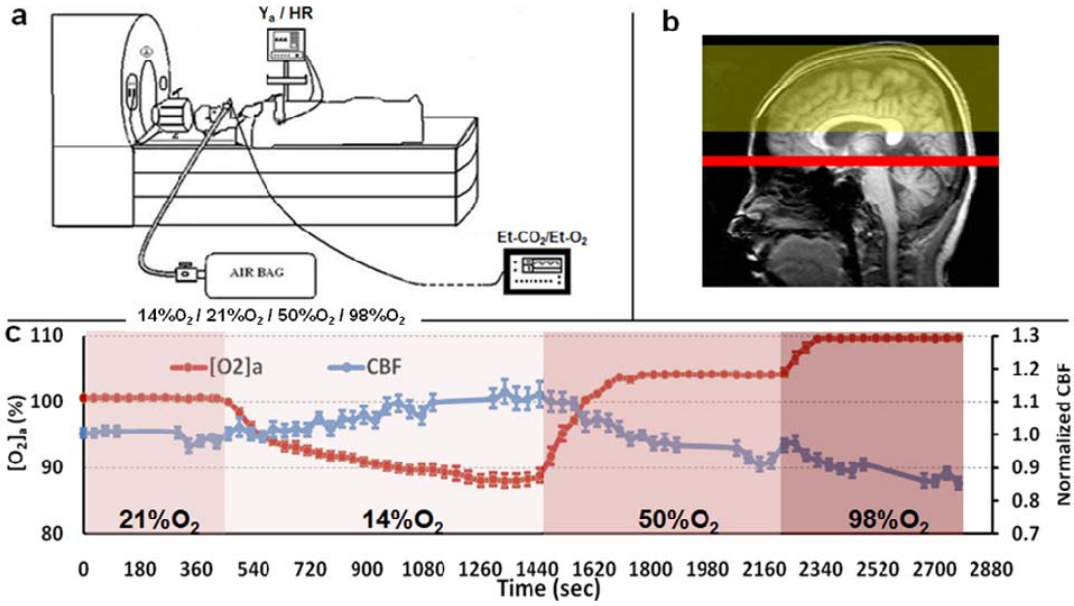

Figure 38 The oxygen experiment design.
(a) The gas delivery system, (b) the TRUST MRI and phase-contrast MRI imaging planning and (c) the order and duration of oxygen challenges. (a) Similar to CO_2 study, this study uses mouthpiece and air bag combination for delivering the gas mixture except that three airbags are filled with graded O_2 concentration. (b) The $CMRO_2$ is measured at sagittal sinus as before. The imaging slice of TRUST MRI and phase-contrast MRI is the red bar; the labeling slab of TRUST MRI is shown in yellow box. (c) In order to remove the mismatch of CBF during TRUST MRI and phase-contrast MRI and correct CBF drift during each block, the CBF is continuously measured shown in blue dots. The continuous Y_a measurement, shown in red dots, is also averaged based the same time frame of the CBF.

Other physiological parameters such as Et-CO_2, Et-O_2, arterial-venous oxygenation difference (also known as OEF), breathing rate and heart rate are summarized in Table 10 as well as Figure 40. The Et-O_2 changes suggest that hypoxia and hyperoxia states were well maintained during the experiment. The OEF appear similar in various graded O_2 conditions (P=0.82, mix model). On the other hand, the flux of O_2 supply does not alter (P=0.45, mix model), suggesting that CBF compensates the O_2 content change. Mild Et-CO_2 reductions during both hyperoxia and hypoxia are observed.

O_2 gas mixture	$[O_2]_a$ (%)	$[O_2]_v$ (%)	CBF (ml/min)	$CMRO_2$ (μmol/min)
21% O_2	100.6±0.1	65.1±1.4	384±17	1097±37
14% O_2	88.3±0.9	54.6±1.1	424±19	1156±38
50% O_2	104.1±0.0	70.5±1.5	364±15	984±33
100% O_2	109.6±0.0	75.7±1.9	338±14	915±44
P value from the mix model	<0.0001	<0.0001	<0.0001	<0.0001

Table 9 The summary of the parameters under various O_2 conditions.
Arterial oxygenation ($[O_2]_a$), venous oxygenation ($[O_2]_v$), cerebral blood flow (CBF) and cerebral metabolic rate of oxygen ($CMRO_2$) measured during inhaling various O_2 concentrated airs (mean ± standard error, N=16)

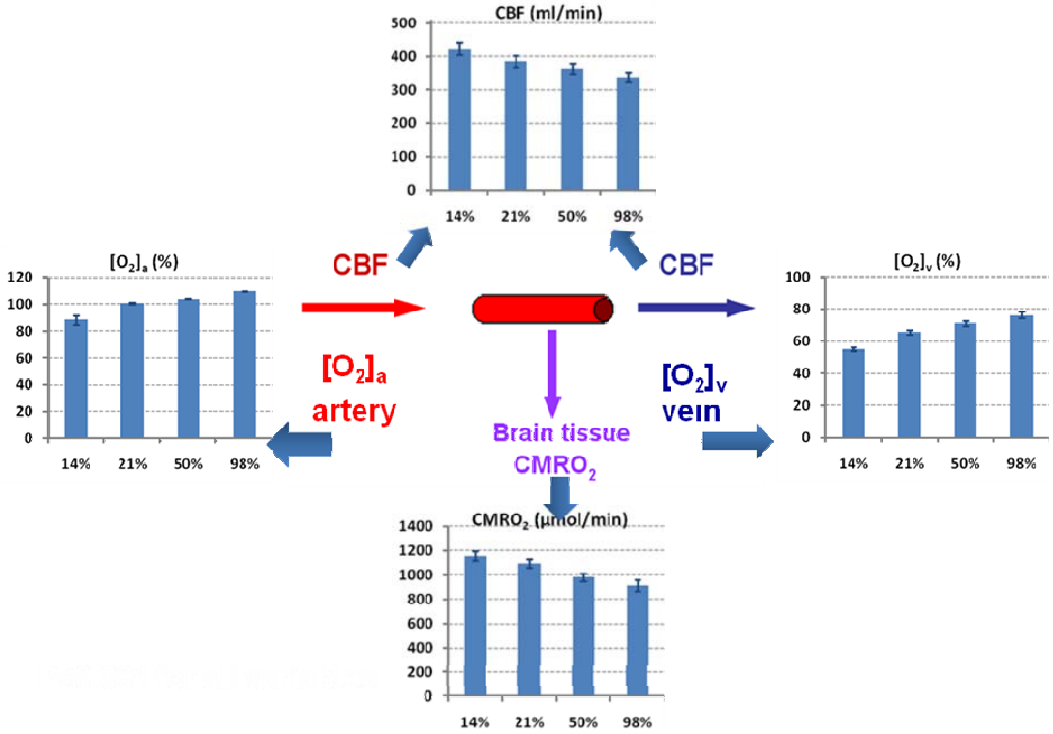

Figure 39 The relationship among vascular and metabolic parameters in the brain and their response to the graded O_2 levels; the error bars indicate standard errors (N=16).

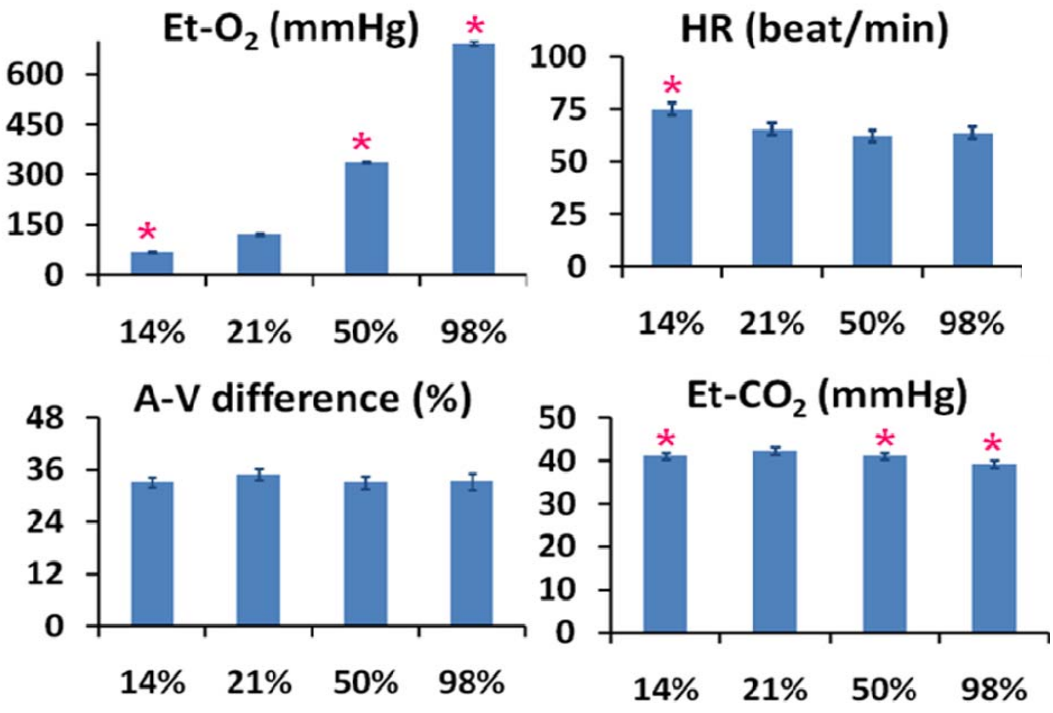

Figure 40 The responses of physiological parameters to the graded O_2 levels (N=16).
The red starts suggest a P<0.05 for the comparison to 21% O_2 by paired t-test.

O_2 gas mixture	OEF=Y_a-Y_v (%)	O_2 supply (μmol/min)	Et-O_2 (mmHg)	Et-CO_2 (mmHg)	HR	BR
21% O_2	34.9±1.4	3221±142	121.3±0.8	42.4±0.9	65±3	13.4±0.9
14% O_2	33.2±1.1	3108±125	67.4±0.7	41.2±0.8	75±3	14.1±1.0
50% O_2	33.1±1.5	3162±127	336.5±0.9	41.2±0.8	62±3	14.9±0.7
100% O_2	33.3±1.9	3085±128	692.9±8.0	39.2±0.8	64±3	15.3±0.9

Table 10 The summary of other physiological parameters responding to graded O_2.
Oxygen extraction fraction (OEF), total flux of oxygen supply, Et-O_2, Et-CO_2, HR and BR measured during inhaling various O_2 concentrated airs (mean ± standard error, N=16).

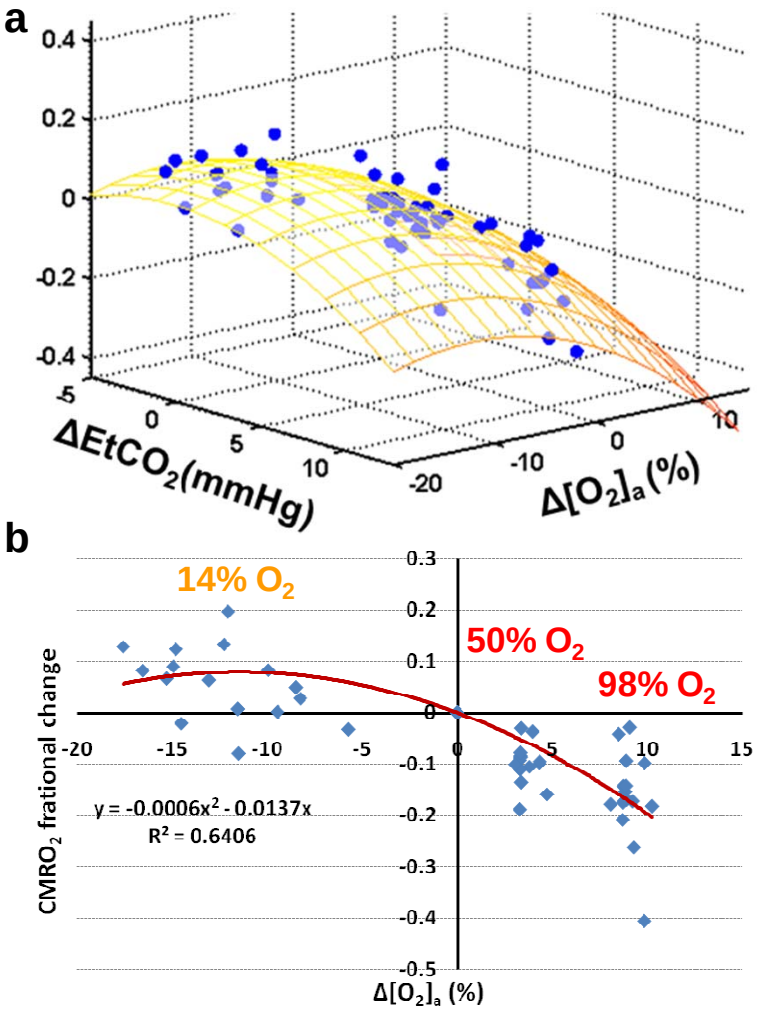

Figure 41 The CO_2 and O_2 effects on the relative $CMRO_2$ ($rCMRO_2$) changes.
(a) Regression model with effects of both CO_2 and O_2 using second order polynomials. The CO_2 and O_2 effect are quantified by $EtCO_2$ change ($\Delta EtCO_2$) and $[O_2]_a$ change ($\Delta[O2]_a$) respectively. $rCMRO_2 = -0.00023 \cdot \Delta EtCO_2 - 0.0015 \cdot \Delta EtCO_2^2 - 0.013 \cdot \Delta[O_2]_a - 0.00054 \cdot \Delta[O_2]_a^2$ (R^2=0.74) (b) The dependence of $rCMRO_2$ on $\Delta[O2]_a$.

The Figure 41a shows the regression model of the fractional $CMRO_2$ change ($rCMRO_2$) with the $EtCO_2$ change ($\Delta EtCO_2$) and $[O_2]_a$ change ($\Delta[O2]_a$). The R^2 of the second order polynomial is significantly larger than the linear

(P<0.001) but not different from the third order (P=0.15). So the second order polynomial was used to regress out CO_2 effect. The model is:

$$rCMRO_2 = -0.00023 \cdot \Delta EtCO_2 - 0.0015 \cdot \Delta EtCO_2^2 - 0.013 \cdot \Delta[O_2]_a - 0.00054 \cdot \Delta[O_2]_a^2$$

After correcting the CO_2 effect by estimating the $rCMRO_2$ at iso-$EtCO_2$, the $rCMRO_2$ is primarily dependent on O_2 change shown in Figure 41b (R^2=0.6, P<0.001). Each group of $rCMRO_2$ values are significantly different from zero (P<0.05) suggesting that O_2 affect the brain metabolism independent from CO_2.

4.3.5 Discussion

Using graded O_2 challenges the brain aerobic metabolism is shown to be dependent on the blood O_2 tension in such a way that $CMRO_2$ is increased by hypoxia and decreased by hyperoxia. In addition, the O_2 effect on the brain metabolism appears to be a dose-dependent manner. The dissolved O_2 was accounted for the arterial oxygenation, which showed a consistent change with venous oxygenation. The arterio-venous difference in oxygenation appears to be steady. The CBF change compensates the blood oxygenation change and subsequently yields a stable O_2 supply to the brain. Coherent changes in CBF and $CMRO_2$ may suggest an undisturbed neurovascular coupling.

The blood flow change due to hypoxia or hyperoxia has been extensively studied (Binks *et al* 2008; Brown *et al* 1985; Bulte *et al* 2007; Demchenko *et al* 2002; Nishimura *et al* 2007; Noth *et al* 2008). However, whether O_2 alters the brain activity is not well understood. This result seems to suggest that the cerebral

oxidative metabolism changes independently from how much O_2 is given. This argument is supported by two observations. Hyperoxia increases and hypoxia decreases the blood pO_2; yet the OEF does not change accordingly. This suggests that increasing or decreasing the intracellular pO_2 does not facilitate or suppress the percentage of O_2 uptake. The brain metabolism even alters against the tissue pO_2 change. Secondly, given the change of O_2 content in the bloodstream, the total amount of O_2 available to the brain tissue is compensated by the CBF. However, the oxygen consumption still changes in spite of a steady O_2 supply estimated by CBF x $[O_2]_a$ x C_h.

Other studies showed evidences of enhanced cerebral metabolism during acute hypoxia. For example, Harik et al. found that hypoxia increased regional metabolic rate of glucose by 10-40% (Harik *et al* 1995; LaManna and Harik 1997). The elevated glucose metabolism was explained by the increased glycolysis (Beck and Krieglstein 1987) and the increased GLUT-1 transporter density associated with hypoxia inducible factor 1 (HIF-1) (Harik *et al* 1996). This study provides new evidence for the increased aerobic metabolism of glucose. The increased glucose metabolism and glutamate oxidation have also been found in ischemic hypoxia (Batista *et al* 2007; Pascual *et al* 1998). In addition, the change of cytochrome oxidase activity, an indicator of oxidative demand, during hypoxia was inconsistently reported (Hamberger and Hyden 1963; Tisdall *et al* 2007).The contradictory findings merit a more direct method to

confirm the result. Among the studies of hyperoxia, ^{13}C NMR of the hippocampus following a cardiac arrest showed a suppressed glucose oxidative metabolism and impaired tricarboxylic acid cycle after a treatment using hyperoxic gas. (Richards *et al* 2007). The study of the microelectrode measured pO_2 on brain slices showed that hyperoxia reduced the pO_2 difference between the metabolic active slice and the metabolic poisoned slice, implying a smaller oxygen consumption in hyperoxia (Mulkey *et al* 2001).

The physiologic responses in our studies are consistent with previous reports. For example, HR was increased under hypoxia, which might be another indicator for a hypermetabolic state (Du *et al* 2008). The reduced Et-CO_2 caused by hyperventilation was frequently observed in both hypoxia and hyperoxia previously (Baddeley *et al* 2000; Dean *et al* 2004; Guyton and Hall 2005). Despite the small fraction of CO_2 added (1% CO_2 for 50% O_2 and 2% CO_2 to 98% CO_2) in order to compensate for the effect of hyperventilation, there was still about 1mmHg decrease in inhaling 14% O_2 and 50% O_2, and 3mmHg decrease in inhaling 98% O_2. Given the knowledge that CO_2 could alter brain activity (Xu *et al* 2011), the subtle Et-CO_2 change as a result of the pulmonary response to the blood O_2 tension may confound the O_2 induced $CMRO_2$ changes. One way of separating the CO_2 and O_2 effects is to quantify each one's contribution to the $CMRO_2$ change. Introducing Et-CO_2 and $[O_2]_a$ change as two regressors and fractional $CMRO_2$ change as a depedent variable in the regression model, the

coefficients can tell quantitative effects on CO_2 and O_2 effects. The fractional change is chosen over the absolute change is to correct the baseline variation across people, such as the brain size. The CO_2/O_2 effect is presented by the changes of Et-CO_2 and $[O_2]_a$. The dynamic range of Et-CO_2 in the current study is too narrow to estimate the CO_2 effect, so previous hypercapnia study data were added to the current O_2 study dataset to more accurately estimate the CO_2 effect. The second order polynomial model gave a better fitting than the linear model according to the F test ($P<0.001$), while the third polynomial does not further improve the fitting ($P=0.15$). A negative effect of O_2 on brain metabolism is maintained after accounting for the CO_2 effect (Figure 41). This effect also appears dose dependent (Figure 41b) since an extreme hyperoxia (98% O_2) yields a greater reduction than the moderate hyperoxia (50% O_2).

The findings from the present study should be interpreted in view of a few limitations. One is the approximation of p_aO_2 by Et-O_2. The Et-O_2 was 693±2 mmHg for 98% O_2, about 10mmHg higher than the blood sampling measurement by Floyd et al. (Floyd *et al* 2003), which results in a 0.1% (the absolute unit) overestimation. Therefore, the real hyperoxia induced $CMRO_2$ reduction could be even bigger. Another limitation of this study is that TRUST MRI can only be applied on the major vein because of the sensitivity limitation, thus the $CMRO_2$ measurement is a global measurement and the $CMRO_2$ changes reflect the averaged effects across the whole brain.

According to the finding of the current study, when using hyperoxia to perform the calibration step in calibrated fMRI, the theoretical framework for calibrated fMRI will remain valid but the data analysis should be adjusted slightly. Specifically, the M factor in the calibrated fMRI will become lower; the estimated $CMRO_2$ will be smaller and the CBF/$CMRO_2$ coupling factor will be greater. The trends of neurovascular coupling shifts towards the earlier PET report (Fox and Raichle 1986).

In summary, this graded oxygen study shows that the brain metabolism is inversely related to the blood O_2 tension, i.e. $CMRO_2$ becomes higher during hyopxia and lower during hyperoxia. Based on this finding, the $CMRO_2$ change should be accounted for applying the hyperoxia calibrated fMRI method.

5 The effect age on metabolic and vascular function

5.1 Abstract

With age, the brain undergoes comprehensive changes in its function and physiology. Cerebral metabolism and blood supply are among the key physiologic processes supporting the daily function of the brain, and may play an important role in age-related cognitive decline. Using the technique described in Chapter 3, the metabolic and vascular parameters such as cerebral metabolic rate of oxygen ($CMRO_2$), cerebral blood flow (CBF) and venous blood oxygenation (Y_v) were quantitatively assessed on a well-characterized healthy adult cohort from 20 to 89 years old (N=232) in a non-invasive manner. The results showed that $CMRO_2$ increased significantly with age while CBF decreased with age. This combination of higher demand and diminished supply resulted in a reduction of venous blood oxygenation with age, suggesting a metabolic stress caused by aging.

5.2 Introduction

Extensive literature has established that cognitive function declines with age, even in healthy adults (Cepeda *et al* 2001; Craik 1983; Hasher and Zacks 1988; Park *et al* 1996; Park *et al* 2002; Salthouse *et al* 1989; Salthouse 1996). The neurobiological basis of these changes has also been partially elucidated, and includes structural shrinkage (Raz *et al* 2000; Raz and Kennedy 2009; Salat *et al* 2004), the development of white matter lesions (Bohnen *et al* 2009; Buckner *et al* 2005), and altered neuronal function (Andrews-Hanna *et al* 2007; Gutchess *et al*

2005; Rypma and D'Esposito 2000). Another plausible contribution to age-related cognitive decline is alterations in cerebral metabolism and blood supply (Iadecola *et al* 2009), especially considering the increased risk of arterial stenosis, hypertension and stroke with aging. The present study aims to investigate age-related changes in these physiologic processes.

The human brain represents about 2% of the total body weight, but consumes about 20% of the total energy (Attwell and Laughlin 2001). The energy homeostasis of the brain can be characterized by three physiologic parameters: Y_v, CBF and $CMRO_2$ (Kety and Schmidt 1948b) (see Figure 8 for a diagram illustration). Arterial vessels deliver blood that has an oxygenation level close to unity, the flow rate of which is denoted by CBF. When the blood transits through capillary beds, a portion of the carried oxygen is extracted by brain tissue for its metabolism, the rate of which is denoted by $CMRO_2$. The portion that remains in the blood will determine the venous oxygenation, Y_v, and is drained through veins. A conceptual simplification of this system is that CBF and $CMRO_2$ reflect oxygen supply and demand, respectively, and Y_v signifies the remaining fraction after demand has been met from the available supply.

With age, the balance of energy demand and supply might be disturbed. There could be several hypotheses of the homeostasis changes. For example, the $CMRO_2$ might decrease as function of age, because of the brain tissue atrophy and neuron deficiency. Or $CMRO_2$ could go higher if the remaining neurons have to

work harder to compensate the loss and less efficiently produce an unchanged behavior. The CBF has been reported for its reduction for aging in positron emission tomography (PET) studies. However, this observation might be confounded by the larger ventricle developed in aged brain since the partial volume effect is unavoidable in PET. Therefore, the change of Y_v is uncertain in either case, and requires further investigation.

In this chapter, how the homeostasis of the cerebral metabolism and vasculature is challenged by aging will be discussed. In addition to CBF, the age effect on cerebral vascular reactivity (CVR) is also studied. CVR measures the vascular reserve via challenging the CBF. In this study, the blood vessels are challenged by inhaling 5% CO_2 which is a potent vascular dilator. The healthy vessels appear elastic responding to CO_2, while aging vessels due to angioscloerosis become less sensive to CO_2 challenge. With the advanced BOLD fMRI technique, one can assess CVR at a high resolution. Quantifying the changes of CVR not only reveals a physiological parameter developing along lifespan, but also provides some hints of understanding the difference of fMRI signals observed in elders compared to those in youngers. Since the fMRI signal relies on vascular response to detect the neural activities, it is likely that age differences in CVR affect evoked blood flow responses, which modulates the fMRI signal independent of neural activity. Thus, cognitive neuroscience of aging

research will be tremendously advanced by the characterization of the age-related changes in CVR.

5.3 Materials and methods

Participants

Participants were recruited from the cohort of a large-scale aging study, the Dallas Lifespan Brain Study (DLBS), which is a comprehensive lifespan study on cognitive function and neuroimaging. DLBS includes detailed and comprehensive measures of brain structure and function using MRI, as well as multiple measurements of a broad range of behavioral measures of cognitive function. The Health Insurance Portability and Accountability Act (HIPAA) compliant protocol was approved by the UT Southwestern Institutional Review Board and written informed consent was obtained from all participants. All participants underwent extensive health screening and had no contraindications to MRI scanning (pacemaker, implanted metallic objects, claustrophobia), and were generally of good health, with no serious or unstable medical conditions such as neurological disease, brain injury, uncontrollable shaking, past by-pass surgery or chemotherapy, or use of medications that affects cognitive function. All participants were highly right-handed, native English speakers with at least a high school education, and a Mini-Mental State Exam (MMSE) (Folstein *et al* 1975) score of 26 or greater. The racial and ethnic distribution of the sample included American Indian (2 or 1%), Asian American (9 or 4%), African American (12 or

5%), Hispanic (10 or 4%), Multiracial (4 or 2%), Caucasian (195 or 84%). Thirty-three subjects who reported a diagnosis of hypertension were taking antihypertensive medications (mostly Angiotensin Converting Enzyme Inhibitors, Beta-blockers, and Angiotensin II Receptor Antagonist). The hypertensive participants were significantly older than their normotensive peers, $t=-8.59$, $p<0.001$, but did not differ on education, $t=-0.491$, ns, or MMSE, $t=1.22$, ns. Mean systolic and diastolic blood pressure for the hypertensive group (137.85/83.48 mm Hg) significantly exceeded (for systolic pressure, $t=5.10$, $p<0.001$; for diastolic pressure, $t=2.70$, $p=0.009$) that of the controls (122.73/79.35 mm Hg). There were in a total of 232 subjects (aged 20-89). Table 11 lists demographic information for the participants.

Age range	20's	30's	40's	50's	60's	70's	80's
N	40	22	33	35	40	40	22
Gender (F/M)	27/13	13/9	23/10	23/12	25/15	23/17	11/11
Education (years, mean±SD)	16.10 ±2.39	17.27 ±2.37	16.27 ±2.79	17.46 ±2.44	16.70 ±2.52	16.10 ±2.88	16.45± 2.48
MMSE* (mean±SD)	28.50± 1.26	28.48±1.36	28.57 ±1.20	28.13 ±1.15	27.70 ±1.24	27.14 ±1.40	27.14± 1.17

* Mini-mental State Exam

Table 11 The subject demographic information and the number of subjects for each physiologic measure.

Overview of experimental procedures

MRI investigations were performed on a 3 Tesla MR system (Philips Medical System, Best, The Netherlands). A body coil was used for radiofrequency (RF) transmission and an 8-channel head coil with parallel imaging capability was used for signal reception. Foam padding was used to stabilize the head to minimize motion. The cerebral metabolic and vascular measurements described below were completely non-invasive and conducted in a scan session of approximately 10 minutes.

Global venous oxygenation

Global venous oxygenation, Y_v, was measured non-invasively from superior sagittal sinus (SS) using a recently developed technique T_2-relaxation-under–spin-tagging (TRUST) MRI (Lu and Ge 2008b). The imaging parameters were: voxel size 3.44x3.44x5mm^3, TR=8000ms, TI=1200ms, four TEs: 0ms, 40ms, 80ms and 160ms, duration 4.3 min.

The data processing procedures was for TRUST MRI were based on an algorithm described in Chapter 3.4.2 and (Lu and Ge 2008b).

Global CBF

Total CBF to the entire brain was measured with phase-contrast (PC) flow velocity MRI with imaging slices positioned at a level that allowed simultaneous assessment of the four feeding arteries, including left/right internal carotid and

left/right vertebral arteries. To visualize these arteries and to ensure correct positioning of PC MRI, a time-of-flight angiogram was first acquired with the parameters: TR/TE/flip angle=23ms/3.45ms/18°, FOV=160x70x160mm^3, voxel size 1.0x1.0x1.5mm^3, number of slices =47, one saturation slab of 60mm positioned above the imaging slab, duration 1 min 26 sec. The PC MRI was then performed with the following parameters: single slice, voxel size = 0.45x0.45x5 mm^3, FOV = 230x230x5 mm^3, TR/TE=20/7 ms, flip angle=15°, maximum velocity encoding = 80 cm/s, duration 30 sec.

To quantify total CBF from PC MRI data, left/right internal carotid and left/right vertebral arteries were identified from the phase image (i.e. velocity map). These arteries were distinguishable from the veins (e.g. internal jugular veins) because their blood flow direction is opposite to that of the veins. An ROI was then drawn on each of the four arteries based on the magnitude image. The ROI mask was applied to the velocity map and the integration of the map (i.e. velocity x area) yielded cerebral blood flow in units of ml/min.

To account for brain size differences and to obtain unit-mass CBF values, the total CBF was divided by the brain mass obtained from a high-resolution T_1-weighted scan with the following parameters: magnetization-prepared rapid acquisition of gradient echo (MPRAGE) sequence, TR/TE/TI=8.1ms/3.7ms/1100ms, flip angle=18°, voxel size 1x1x1mm^3, number of slices 160, sagittal slice orientation, duration 3 minutes and 57 seconds. The

delineation of brain boundary used the software FSL (FMRIB Software Library, Oxford University, UK). The brain volume was converted to brain mass by assuming a density of 1.06 g/ml (Herscovitch and Raichle 1985). The resulting global CBF value is in units of ml/100g/min.

Global $CMRO_2$

Global $CMRO_2$ is calculated using Eq.1. The arterial oxygenation, Y_a, is close to unity and has been reported to be minimally affected by age (Leenders *et al* 1990; Li *et al* 2006). To confirm this notion, I measured Y_a using a pulse oximetry in a subset of the subjects (in the ones that participated in the CO_2 study, N=152) and found that the dependence of Y_a on age can be written as Y_a=99.06%-0.02% x Age (Figure 42), i.e. Y_a decreases by 1% every 50 years. Thus Y_a indeed shows a minimal effect of age. In our $CMRO_2$ calculation, I used the above expression to estimate Y_a of each individual based on his or her age.

Regional CVR

Regional CVR measurement followed protocols established in previous studies (Yezhuvath et al. 2009). CVR was assessed using hypercapnia induced by 5% CO_2-breathing (mixed with 21% O_2 and 74% N_2). Hypercapnia was administered via a plastic bag with a valve to switch between room air and CO_2 air. A mouthpiece and a nose clip were used to achieve mouth-only breathing. A research assistant was inside the magnet room throughout the experiment to switch the valve and monitor the subject. Physiologic parameters, including end-

tidal (Et) CO_2, breathing rate, heart rate, and arterial oxygenation (Y_a), were recorded during the experiment (MEDRAD; Novametrix Medical Systems). The type of air breathed in was switched every minute in a manner similar to a block design fMRI experiment, while blood oxygenation level--dependent (BOLD) MR images were acquired for 7 min. Imaging parameters were: FOV = 220×3×220 mm^2, matrix size = 64×3×64, 43 axial slices, thickness=3.5mm, no gap, TR/TE/flip angle = 2000 ms/25ms/80, single-shot EPI, and duration 7 min.

CVR data were processed using a general linear model (SPM2, University College London, UK) similar to a typical fMRI scan, except that the regressor was the Et-CO_2 time course rather than the fMRI paradigm. In-house MATLAB (Mathworks) scripts were used to obtain Et-CO_2 time courses that were synchronized with MRI acquisitions. Since the hypercapnia-induced vasodilatation is mediated by CO_2 level changes, Et-CO_2 time course provides an input function to the vascular system. The BOLD time course is the output signal, and by comparing the input and output signals, the vascular system property was determined (Yezhuvath et al. 2009). Absolute CVR is in units of %BOLD signal change per mmHg Et-CO_2 chagne (%BOLD/mmHg CO_2).

Data analysis

For the global measures of venous oxygenation, CBF, and $CMRO_2$, multiple regression analysis was employed with the metabolic/vascular measure as the dependent variable. Age and gender were used as the independent variables.

As an exploratory analysis, a quadratic age term, that is, age^2, was also added to the model to assess whether a nonlinear equation could yield better fitting of the data. Decade-bydecade time courses were obtained by averaging the subjects in each decade (e.g., 20--29, 30--39, etc.).

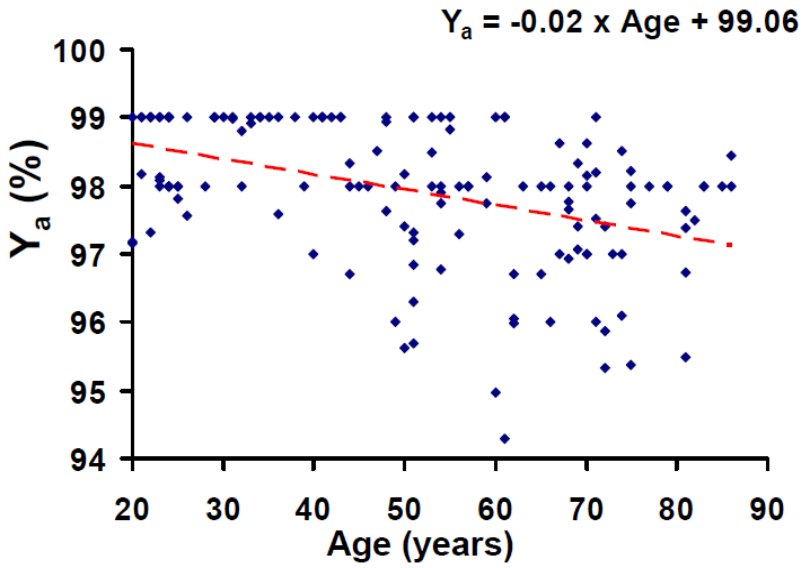

Figure 42 Scatter plot between arterial oxygenation (Y_a) and age.
Similar to reports from literature, the arterial oxygenation value is close to unity and is minimally affected by age. Every year, Y_a decreases by approximately 0.02% (N=152, R=0.42, $p<0.0001$).

For the regional CVR map, in individual space were processed with Statistical Parametric Mapping (SPM2, University College London, UK) and Hierarchical Attribute Matching Mechanism for Elastic Registration (HAMMER, University of Pennsylvania, PA) software packages. The maps were normalized to the Montreal Neurological Institute (MNI) template space using the high-resolution T1-weighted image as an intermediate step. The HAMMER algorithm is used for the spatial normalization process, because it was shown to be relatively

robust even in the presence of brain atrophy and it also has the option to conduct concentration-preserving transformation (Shen and Davatzikos 2002). This was important to make sure the comparison truly reflected vascular parameters rather than being affected by brain volume reduction. The images were further smoothed using a Gaussian filter with full-width-half-maximum of 12mm. This step was necessary to account for small difference in gyri/sulci locations across subjects.

For voxel-by-voxel statistical analysis of CVR maps, a multiple regression analysis with age, gender, gray matter probability and CSF probability as the regressors. The gray matter and CSF probability indices were obtained by segmentation routines in SPM2. They were included in the model to eliminate any residual partial volume effect at the intravoxel level so that the observed age dependence is not due to an increased CSF fraction or reduced gray matter fraction in older subjects.

5.4 Results

Global venous oxygenation decreases with age

Figure 43 shows the scatter plot between Y_v and age (N=232). Regression analysis revealed that age has a statistically significant ($p<0.0001$) effect on Y_v. Specifically, average Y_v in typical 20-year-old subjects is approximately 64.2% and it decreases with age at a rate of 1.4% per decade, suggesting that the balance between oxygen demand and supply is gradually altered with age. A quadratic model with age^2 as an additional regressor did not improve the fit.

Inter-subject variability in Y_v was also assessed on a decade-by-decade basis and it showed a significant increase with age (Figure 44, cross-correlation coefficient between decade and standard deviation of Y_v within the decade R=0.81, p=0.0272). That is, with age, Y_v not only shows a gradual decrease but the inter-subject heterogeneity also becomes greater.

The brain atrophy assessed by the fraction of parenchyma volume to intracranial volume, shows a reduction as function of age (Figure 45). Comparing the Y_v reduced with age, the fractional brain volume appears to decline at a slower rate (Figure 46). This lag of reduction seems suggesting the functional change precedes the anatomical deficiency.

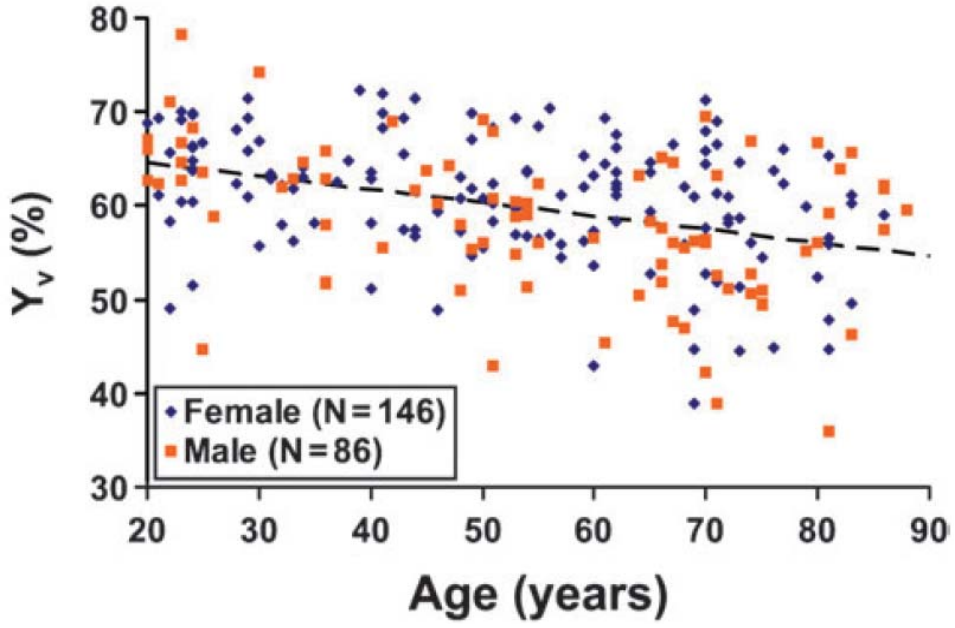

Figure 43 Scatter plot between global venous oxygenation (Y_v) and age (N=232).
Each dot represents data from one subject. The data from female and male subjects are shown with different symbols. The dashed line is a linear fitting of the experimental data from both genders. Regression analysis showed that age has a significant effect on Y_v ($p<0.0001$), but a quadratic

model did not improve the fitting. Female subjects showed higher Y_v compared to male subjects (p=0.0205).

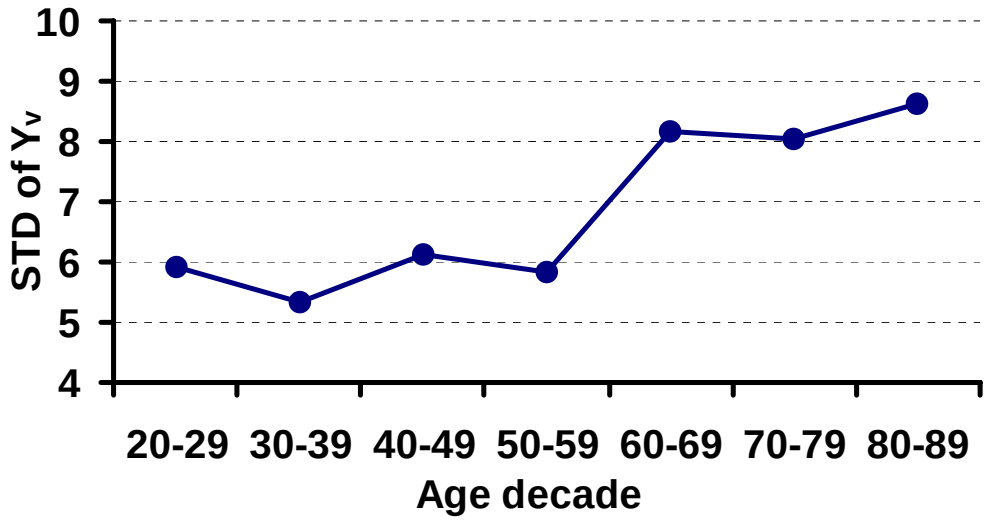

Figure 44 The standard deviation of venous oxygenation (Y_v) in every decade.
The inter-subject variation of Y_v significantly increases as age (R=0.81, p=0.0272).

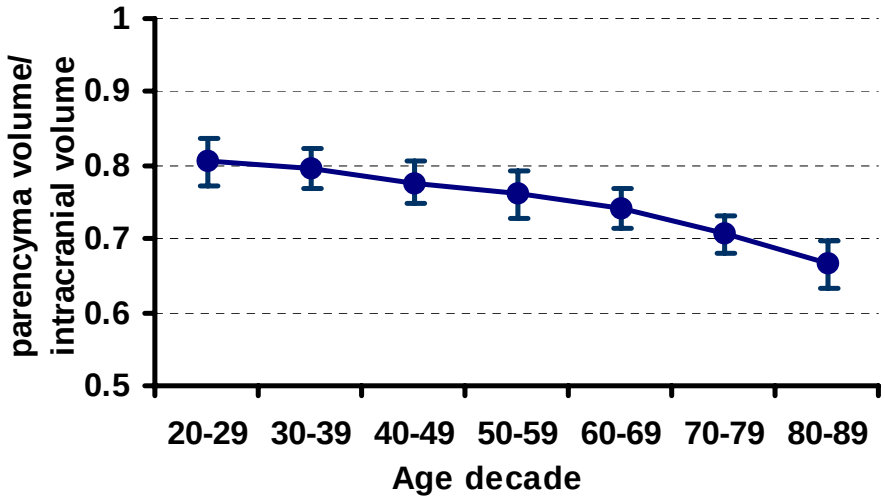

Figure 45 The assessment of brain tissue atrophy.
Atrophy is defined by the fraction of parenchyma volume to intracranial volume for every decade; error bar is the standard deviation.

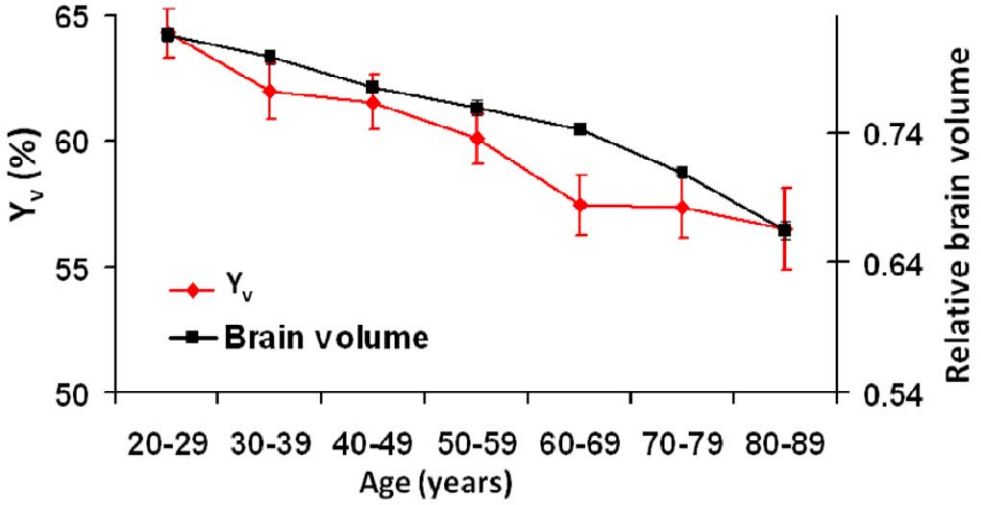

Figure 46 The overlay of venous oxygenation (Y_v) and relative brain volume as a function of age.
The decline of Y_v occurs earlier than the reduction of parenchyma volume fraction, indicating the functional change occurs earlier than the anatomical change during the life span.

Global CBF decreases with age

Figure 47a illustrates the location of the four feeding arteries, from which global CBF was measured and normalized with respect to the brain parenchyma volume to account the brain atrophy shown in Figure 45. Figure 47b shows the scatter plot between CBF and age (N=232). Regression analysis revealed an age-related decrease (p=0.0065) of global CBF at a rate of 0.8 ml/100g/min per decade, from an average CBF of 58.1 ml/100g/min in typical 20-year-old subjects.

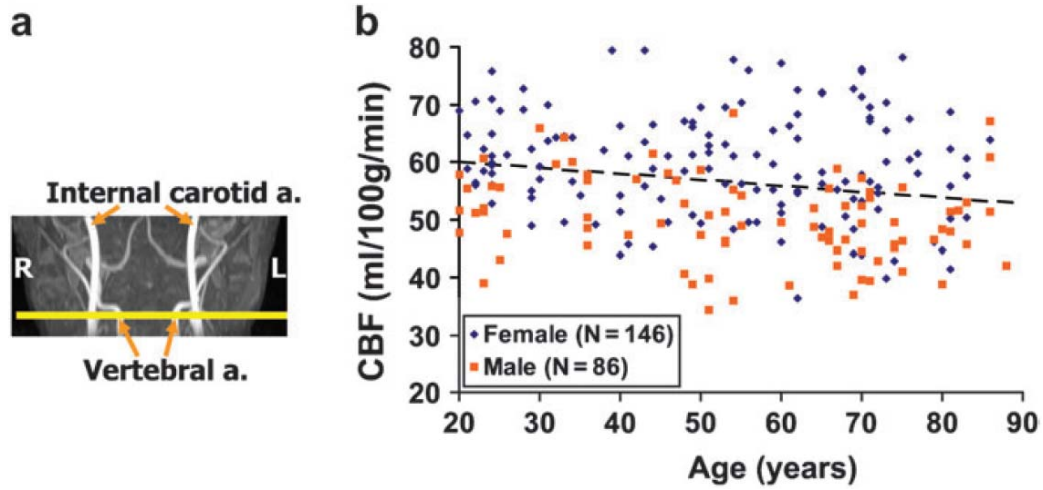

Figure 47 The global CBF changes with age.
(a) Illustration of the imaging slice (yellow) with regards to the major feeding arteries. (b) Scatter plot between global CBF and age (total N=232). The data from female and male subjects are shown with different symbols. The dashed line is a linear fitting of the experimental data from both genders. Regression analysis showed that age has a significant effect on CBF ($p=0.0065$). Female subjects showed higher CBF compared to male subjects ($p<0.0001$).

Global $CMRO_2$ increases with age

Figure 48 shows the scatter plot between $CMRO_2$ and age (N=232). Regression analysis revealed that there is paradoxical increase of $CMRO_2$ with age ($p=0.0101$). Average $CMRO_2$ of typical 20-year-old subjects is approximately 164.1 μmol/100g/min and it increases with age at a rate of 2.6 μmol/100g/min per decade. Therefore, the aging brain appears to suffer from double insults of decreased oxygen supply and increased oxygen demand, resulting in an age-related decrease in venous oxygenation. Note that the $CMRO_2$ value reported in this study is for unit mass brain parenchyma, thus the brain atrophy effect has been accounted for (Figure 45). As far as the total brain oxygen consumption is

concerned, an age-related decrease was observed because the brain size is smaller in older subjects (Figure 49).

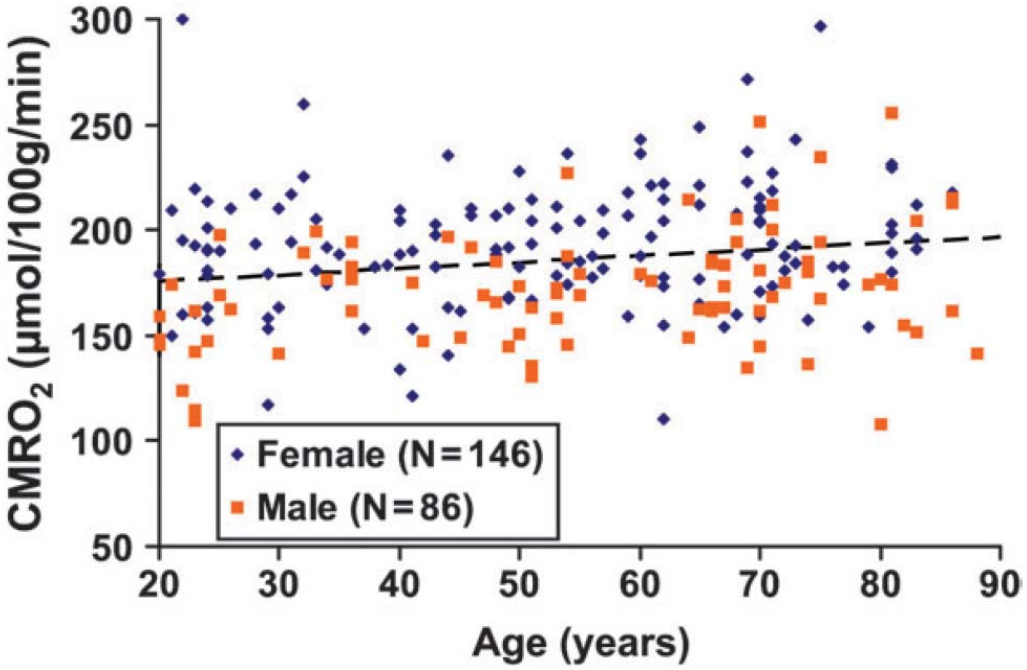

Figure 48 Scatter plot between global $CMRO_2$ and age (N=232).
The data from female and male subjects are shown with different symbols. The dashed line is a linear fitting of the experimental data. Regression analysis showed that age has a positive effect on $CMRO_2$ ($p=0.0101$). Female subjects showed higher $CMRO_2$ compared to male subjects ($p<0.0001$).

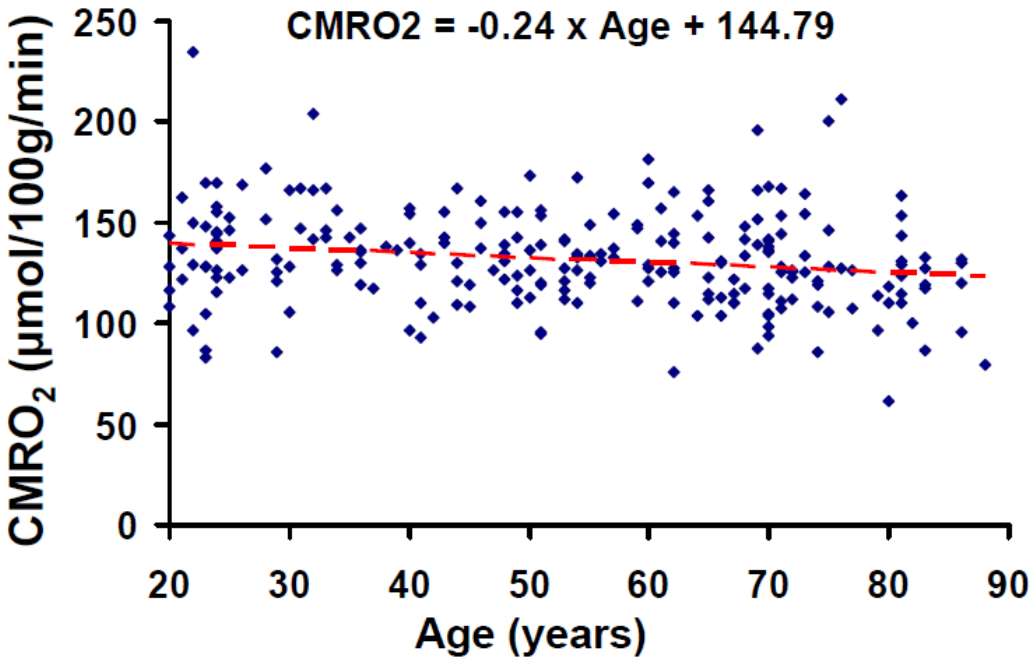

Figure 49 Scatter plot between intracranial-space-based $CMRO_2$ and age (N=232, R=0.19, p=0.008).
The dashed line is a linear fitting of the experimental data. Regression analysis showed that age has a negative effect on intracranial-space-based $CMRO_2$, which is opposite from that on parenchyma-volume-based $CMRO_2$ in Figure 48.

CVR Decreases with Age

Figure 7 shows the voxels that revealed a significant CVR decrease with age using voxel-based linear regression (N=152). It can be seen that CVR reduction is more prevalent compared with CBF. ROI analysis revealed highly significant age effects in all regions assessed, including frontal lobe (corrected P<0.001), parietal lobe (P<0.001), temporal lobe (P=0.003), occipital lobe (P=0.002), insular cortex (P<0.001), and subcortical gray matter (P=0.003). A quadratic term of age was added into the regression mode. The regions showing

an improved fitting include insular cortex (P=0.010) and subcortical gray matter (P=0.007), suggesting that CVR decline may be nonlinear (accelerated) with age.

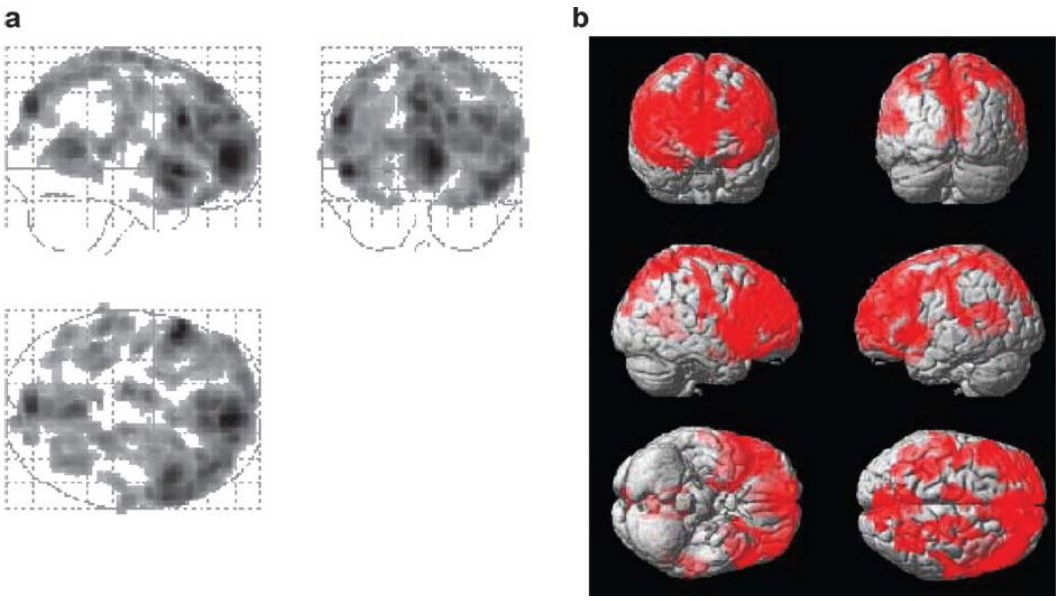

Figure 50 Results of voxel-based analysis of CVR decrease with age.
(a) shows the glass brain overlay, and (b) shows the redering on the Montreal Neurological Institute (MNI) brain template. Colored voxels indicate brain regions with age-related CVR decrease (P<0.005, cluster size=200 voxels). The CVR alterations cover the majority of the brain with the exception of occipital pole.

5.5 Discussion and conclusion

In the present study, I studied the age-related differences in brain metabolism and vasculature in a relatively large cohort of healthy subjects. The CBF and $CMRO_2$ measurement suggest that the brain's energy homeostasis is disturbed in aging due to an increase in oxygen demand and a concomitant reduction in blood supply. Therefore, the venous oxygenation was found to decline as a function of age, and such an alteration occurrs at middle age.

This work represents a thorough investigation of metabolic and vascular physiology in aging with multiple static and dynamic parameters assessed in the same cohort. Age-related CBF differences have been extensively studied in the literature using various imaging modalities and the finding of a CBF decrease with age is in general agreement with most previous reports (Bertsch *et al* 2009; Devous *et al* 1986; Hagstadius and Risberg 1989; Heo *et al* 2009; Leenders *et al* 1990; Martin *et al* 1991). A novel finding from the present study is the highly significant decrease in venous oxygenation (i.e. an increase in oxygen extraction fraction, OEF) with age. Very few studies in the literature assessed OEF in normal aging due to the need of radiotracer injection and arterial blood sampling. The few studies that measured OEF all failed to identify a significant effect of age (Frackowiak *et al* 1980; Leenders *et al* 1990; Marchal *et al* 1992; Yamaguchi *et al* 1986), possibly because of variations in individual values and a relatively small sample size (ranging from 12-34 subjects). Owing to the recent development in non-invasive oxygenation mapping techniques (Lu and Ge 2008b), I were able to measure venous oxygenation in 232 subjects and the results unequivocally showed an age-related difference in OEF, demonstrating a disturbed balance between oxygen supply and consumption in aging. One should note that the TRUST MRI technique, by its design principle, is not susceptible to brain atrophy because the method is based on the MR T_2 decay time constant rather than on the

MR signal itself. Thus the age-related reduction in tissue volume is not a confounding factor in our oxygenation measurement.

Another interesting observation was that the oxygen metabolic rate, $CMRO_2$, was found to increase with age. This is opposite to most of the reports in literature, where $CMRO_2$ was found to decrease with age (Kety 1956; Leenders *et al* 1990; Marchal *et al* 1992; Yamaguchi *et al* 1986). I hypothesized that this discrepancy is due to brain parenchyma volume reduction that is difficult to correct in previous PET and SPECT imaging studies, which would allow CSF to be partial-volumed in the measurement and result in an underestimation in $CMRO_2$ in elderly subjects. To test this hypothesis, I re-analyzed the data by calculating $CMRO_2$ per unit volume of intracranial space (instead of per unit volume of pure tissue). The results then became consistent with the previous findings, showing a significant $CMRO_2$ decrease with age ($p=0.008$, slope =-2.4 μmol/100g/min per decade, see Figure 49 for scatter plot). Therefore, our results suggest that the age-related metabolic decline reported previously may be largely driven by a reduced brain volume in older subjects. For the brain tissue that remained, the metabolic rate is actually higher in the elderly. Such a change may reflect an age-related reduction in neuronal computational efficiency or possible leakage in membrane ion channels, which necessitates more active Na^+/K^+-ATPase pumps to maintain the membrane polarity (D'Esposito *et al* 2003; Iadecola *et al* 2009). For comparison, we note that a few studies have measured

whole body metabolic rate as a function of age (Frisard *et al* 2007; Krems *et al* 2005; St-Onge 2005). It was found that whole body metabolic rate decreases with age. Much of these age-related changes can be explained by the change in body composition (i.e. more fat mass and less fat-free mass) and a reduction in physical activity (Luhrmann *et al* 2009). Interestingly, after adjusting for body composition and physical activity, the remaining energy expenditure actually increased with age, a finding similar to the present study conducted for the brain.

The gender difference was also observed in that female subjects had higher CBF ($p<0.0001$) and $CMRO_2$ ($p<0.0001$) compared to males (Figure 51). This CBF difference has been reported previously by a number of investigators (Bertsch *et al* 2009; Devous *et al* 1986; Rodriguez *et al* 1988). Several hypotheses were proposed to explain this difference. One possibility is that female has lower hematocrit, thus in order to carry equal amount of oxygen a higher CBF is needed (Shaw *et al* 1984). Another hypothesis states that the heart actually delivers similar amount of blood to the brain in male and female subjects. However, since female tends to have a smaller brain volume, the CBF value per weight of brain tissue becomes greater. Another possibility for a higher CBF in female is to match the higher metabolic rate as described below. The present study observed a gender-dependent $CMRO_2$ difference with female having a higher average value. This was not noted in previous $CMRO_2$ studies (Leenders *et al* 1990; Marchal *et al* 1992; Yamaguchi *et al* 1986), but is consistent with a previous report

measuring cerebral glucose metabolic rate (Baxter *et al* 1987). The authors attributed this difference to the influence of estrogens, which regulates basal body temperature, ionic balance, and body fluid (Baxter *et al* 1987). However, other studies using similar techniques have found no apparent differences between men and women (Miura *et al* 1990). Thus, the gender differences in brain energy consumption may require further investigation.

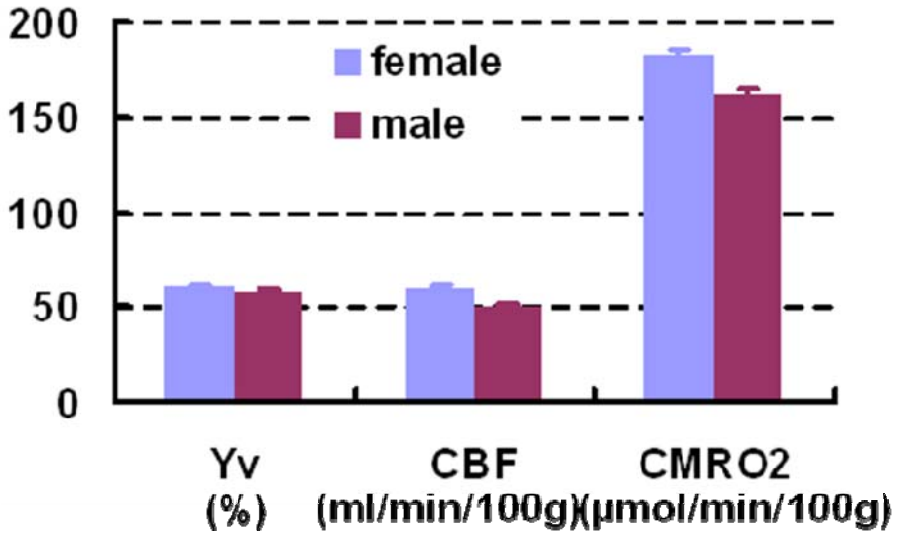

Figure 51 The gender differences in all three parameters.
The venous oxygenation (Y_v, p=0.001), cerebral blood flow (CBF, p<0.0001) and cerebral metabolic rate of oxygen ($CMRO_2$, p<0.0001) all show a gender dependence.

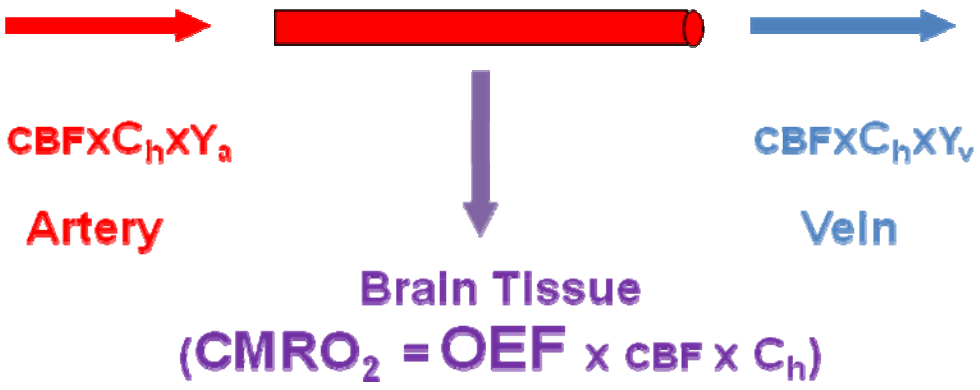

Figure 52 The illustration of the increased metabolic stress in the aging brain.
The venous oxygenation (Y_v) decreases with age, suggesting an unbalanced oxygen supply and consumption. The blood flow (CBF) and arterial oxygenation (Y_a) reduce, resulting a less oxygen supply. However, the oxygen extraction fraction rate (OEF) increase exceeds the CBF suppression, which yields an amplified $CMRO_2$. Aging increases brain metabolism demand but reduces the fuel supply; therefore, the brain faces a metabolic stress.

In summary, noninvasive MRI technique was used to assess metabolic and vascular functions across the adult life span. Age related differences were observed in each of the physiologic parameters studied (Figure 52). In addition, the vessel reactivity is degraded globally. Characterization of these basic physiologic processes may be useful for understanding the mechanisms of age-related changes in cognitive function. In addition, alterations in vascular function have strong implications for interpretation of fMRI signals in cognitive aging.

6 Conclusions and Future work

6.1 Conclusions

My dissertation work can be divided into two parts: one is the technique development for measuring the cerebral metabolic rate of oxygen ($CMRO_2$); the other part is the applications of this $CMRO_2$ method.

The first part includes:

- Implemented the TRUST MRI on both sagittal sinus and internal jugular vein to compare their blood oxygenation values via measuring the blood T_2. Their blood oxygenation values are similar between two locations on healthy subjects.
- Implemented the phase-contrast MRI on both arterial side and venous side to quantify the cerebral blood flow. To remove the pulsation artifact, cardiac gated phase-contrast MRI was implemented. Comparing to the non-gated phase-contrast, the gated phase-contrast MRI results in similar CBF values, but takes much longer time. Therefore, the non-gated phase-contrast MRI was used for its time effeiciency.
- Quantified the whole brain $CMRO_2$ for young healthy subjects using TRUST MRI and phase-contrast MRI. To my knowledge, this study is the first quantitative report of absolute $CMRO_2$ on humans using a completely noninvasive and radioactive free method.

- Obtained the *in vitro* calibration curve for converting the blood T_2 to the blood oxygenation.
- Validated the TRUST MRI using pulse oximetry as a standard. The blood oxygenation was measured at major arteries of the brain for pulse oximetry measures arterial blood oxygenation at finger. To validate the TRUST measurement in a wider range, the hypoxia challenge was used to reduce arterial blood oxygenation.
- Improved the speed of TRUST MRI by shortening TR and removing the bias in short TR via adding a post-saturation pulse. The challenge brought by short TR is the lower signal. So the TE was further reduced to improve the blood signal. An optimal protocol of performing TRUST MRI was proposed as TR of 3000ms and TE of 3.6ms, which reduces the scan time from 3.5min to 1.5min.
- Investigated the reproducibility of this $CMRO_2$ MRI technique on different subjects and different scan sessions. The $CMRO_2$ measurement can be robustly repeated across days/sessions. The parameter of $CMRO_2$ is relative constant across days compared to CBF or blood oxygenation.

The second part includes:

- Studied the neural activities changes during hypercapnia by multi-modalities, such as $CMRO_2$ MRI, functional connectivity MRI and electroencephalography (EEG). The hypercapnia was found to reduce

$CMRO_2$, decrease spontaneous neural activities and slow EEG power spectrua.

- Studied the metabolic and vascular changes caused by hypoxia and hyperoxia. The arterial and venous oxygenations are modulated by the blood O_2 tension. Increaseed $CMRO_2$ and CBF were observed at hypoxia and an opposite trend was found at hyperoxia.
- Studied the aged related changes in CBF, blood oxygen and $CMRO_2$. The slow but significant trends of these parameters were found across lifespan. The lower blood supply and higher metabolic consumption of older subjects suggest a metabolic stress in the aged brain.

6.2 Future work

This $CMRO_2$ MRI technique is a novel method. The current technical development at 3T has made this $CMRO_2$ MRI technique ready for research studies and clinical applications. Along the line, there are a few directions that worth further studying.

6.2.1 Towards the high field

To improve the SNR of TRUST MRI, one direction to go is to use higher magnetic field, such as 7T. The energy level in an applied field is proportional to the magnetic field strength (i.e. $E=h\cdot\gamma\cdot B$, where h is Planck constant and γ is a constant of gyromagnetic ratio). The high energy level results in a higher magnetization of blood, therefore a higher SNR in TRUST MRI. With higher

SNR, the TRUST MRI will have potential to measure the blood T_2 at smaller blood vessels.

Challenges come with the benefit. Firstly, the field inhomogeneity is the main challenge of 7T. A more careful B0 shielding is needed for 7T. Furhtermore, the B_1 inhomogeneity makes the RF pulse hard to play out at the designed flip angle. Therefore, the blood spins cannot be efficiently or correctly tagged by the inversion pulse or T_2-preparation pulses. This problem might be improved by changing the sinc pulse or hard pulse to adiabatic pulse which is less sensitive to B1 homogeneity. In high field, the blood T_1 will become longer, which might make the TR longer. The proposed post-sat TRUST MRI can be used to solve this problem. To adjust the longer blood T_1, the inversion delay time (TI) which uses 1200ms at 3T need to be set longer at 7T. The blood T_2 at 7T will be shorter than that at 3T. Therefore the T_2 preparation period has to be shortened. Besides the problems mentioned above, there will be other challenges for implementing TRUST on the 7T MRI scanner.

6.2.2 Investigate the potential applications for this $CMRO_2$ technique

A normal oxidative metabolism is important for brain health. Applying this $CMRO_2$ technique on patients with impaired aerobic metabolism may aid the diagnosis. Because this technique only gives a whole brain $CMRO_2$, its application will be more suitable for the diseases or innovations affecting the

whole brain metabolism. For example, multiple sclerosis, glucose transport deficiency, diabetes, caffeine ingestion, diet effect and so on.

Notably, the $CMRO_2$ measurement is not limited to diagnostic purpose but also can be applied to evaluating the treatment effect as well as monitoring the symptoms' progression as this method does not exhaust patients by repeated scans because of its non-invasive, non- radioactive, time efficient and cost effective nature.

6.2.3 Further investigate the mechanism of gas challenges

6.2.3.1 Demonstrate the gas effect on the pH *in vivo*

I demonstrated that CO_2 and O_2 modulate $CMRO_2$. It would be more interesting to illustrate the mechanism of these observations. Hypercapnia has been found *in vitro* to suppress neural activities via reducing the intracellular pH (Dulla *et al* 2005). Using phosphorus magnetic resonance spectroscopy (31P MRS), the pH can be quantified *in vivo* (Prichard et al 1983). The improvement of sensitivity of phosphorus spectrum on 7T gives a better estimation of pH. Demonstrating that intracellular pH regulated by hypercapnia, hypoxia and hyperoxia provides relevant evidence for the neural effect of CO_2 and O_2 on conscious humans.

6.2.3.2 Study the O_2 stress on the brain metabolism

Hyperoxia increases the production of reactive oxygen species (ROS) which can cause significant cell damages through oxidizing DNAs, proteins and

enzymes. Consequently, the brain metabolism might be affected by the elevated ROS. The antioxidant substance such as ascorbic acid (i.e. vitamin C) takes up the free electron from ROS and reduces hydroxyl radicals, consequently prevents the cell damages from the oxidative stress. To illustrate that the $CMRO_2$ is impaird by ROS, a study can be designed as following: a group of subjects are given vitamin C, and the other group are given placebo. With the hyperoixa challenge, the vitamin C group is expected to show less $CMRO_2$ reduction than the placebo group. The hypothesis is that vitamin C can reverse the ROS effect by reacting with the hydroxyl radicals. Since ROS is produced in normal condition, one can push this point further more to hypothesize that ROS modulates the oxidative metabolism by comparing $CMRO_2$ value before and after taking vitamin C. The conjecture is that the ROS is suppressed by vitamin C and therefore oxidative metabolism (i.e. $CMRO_2$) is elevated consequently due to smaller oxidative stress. If this holds true, the hypoxia increase $CMRO_2$ might be explained by the reduced ROS stress for less O_2 going to the mitochondria yields less ROS produced proportionally.

Bibliograpy

Abbott NJ, Ronnback L, Hansson E (2006) Astrocyte-endothelial interactions at the blood-brain barrier. *Nat Rev Neurosci* 7:41-53.

Alsop DC, Detre JA (1996) Reduced transit-time sensitivity in noninvasive magnetic resonance imaging of human cerebral blood flow. *J Cereb Blood Flow Metab* 16:1236-49.

An H, Lin W, Celik A, Lee YZ (2001) Quantitative measurements of cerebral metabolic rate of oxygen utilization using MRI: a volunteer study. *NMR Biomed* 14:441-7.

An H, Lin W (2003) Impact of intravascular signal on quantitative measures of cerebral oxygen extraction and blood volume under normo- and hypercapnic conditions using an asymmetric spin echo approach. *Magn Reson Med* 50:708-16.

Andrews-Hanna JR, Snyder AZ, Vincent JL, Lustig C, Head D, Raichle ME, Buckner RL (2007) Disruption of large-scale brain systems in advanced aging. *Neuron* 56:924-35.

Aslan S, Xu F, Wang PL, Uh J, Yezhuvath US, van Osch M, Lu H (2010) Estimation of labeling efficiency in pseudocontinuous arterial spin labeling. *Magn Reson Med* 63:765-71.

Attwell D, Laughlin SB (2001) An energy budget for signaling in the grey matter of the brain. *J Cereb Blood Flow Metab* 21:1133-45.

Attwell D, Iadecola C (2002) The neural basis of functional brain imaging signals. *Trends Neurosci* 25:621-5.

Augustine GJ (2004) Neural Signaling. In: *Neuroscience* (Purves D, Augustine GJ, Fitzpatrick D, Hall WC, La Mantia A, McNamara LQ, Williams SM, eds), 3rd edition ed., Sunderland: Sinauer Associates, Inc.

Baddeley H, Brodrick PM, Taylor NJ, Abdelatti MO, Jordan LC, Vasudevan AS, Phillips H, Saunders MI, Hoskin PJ (2000) Gas exchange parameters in radiotherapy patients during breathing of 2%, 3.5% and 5% carbogen gas mixtures. *Br J Radiol* 73:1100-4.

Bandettini PA, Wong EC, Hinks RS, Tikofsky RS, Hyde JS (1992) Time course EPI of human brain function during task activation. *Magn Reson Med* 25:390-7.

Bangash MF, Xie A, Skatrud JB, Reichmuth KJ, Barczi SR, Morgan BJ (2008) Cerebrovascular response to arousal from NREM and REM sleep. *Sleep* 31:321-7.

Barzilay Z, Britten AG, Koehler RC, Dean JM, Traystman RJ (1985) Interaction of CO2 and ammonia on cerebral blood flow and O2 consumption in dogs. *Am J Physiol* 248:H500-7.

Batista CE, Chugani HT, Juhasz C, Behen ME, Shankaran S (2007) Transient hypermetabolism of the basal ganglia following perinatal hypoxia. *Pediatr Neurol* 36:330-3.

Baxter LR, Jr., Mazziotta JC, Phelps ME, Selin CE, Guze BH, Fairbanks L (1987) Cerebral glucose metabolic rates in normal human females versus normal males. *Psychiatry Res* 21:237-45.

Beck T, Krieglstein J (1987) Cerebral circulation, metabolism, and blood-brain barrier of rats in hypocapnic hypoxia. *Am J Physiol* 252:H504-12.

Benga G, Borza T (1995) Diffusional water permeability of mammalian red blood cells. *Comp Biochem Physiol B Biochem Mol Biol* 112:653-9.

Bertsch K, Hagemann D, Hermes M, Walter C, Khan R, Naumann E (2009) Resting cerebral blood flow, attention, and aging. *Brain Res* 1267:77-88.

Binks AP, Cunningham VJ, Adams L, Banzett RB (2008) Gray matter blood flow change is unevenly distributed during moderate isocapnic hypoxia in humans. *J Appl Physiol* 104:212-7.

Biswal B, Yetkin FZ, Haughton VM, Hyde JS (1995) Functional connectivity in the motor cortex of resting human brain using echo-planar MRI. *Magn Reson Med* 34:537-41.

Biswal B, Hudetz AG, Yetkin FZ, Haughton VM, Hyde JS (1997) Hypercapnia reversibly suppresses low-frequency fluctuations in the human motor

cortex during rest using echo-planar MRI. *J Cereb Blood Flow Metab* 17:301-8.

Bohnen NI, Muller ML, Kuwabara H, Constantine GM, Studenski SA (2009) Age-associated leukoaraiosis and cortical cholinergic deafferentation. *Neurology* 72:1411-6.

Bolar D. (2010) Magnetic Resonance Imaging of Cerebral Metabolic Rate of Oxygen (CMRO2). In: *Electrical and Biomedical Engineering*, Boston: Massachusetts Institute of Technology, p 128

Braun AR, Balkin TJ, Wesenten NJ, Carson RE, Varga M, Baldwin P, Selbie S, Belenky G, Herscovitch P (1997) Regional cerebral blood flow throughout the sleep-wake cycle. An H2(15)O PET study. *Brain* 120 (Pt 7):1173-97.

Brown MM, Wade JP, Marshall J (1985) Fundamental importance of arterial oxygen content in the regulation of cerebral blood flow in man. *Brain* 108 (Pt 1):81-93.

Buckner RL, Snyder AZ, Shannon BJ, LaRossa G, Sachs R, Fotenos AF, Sheline YI, Klunk WE, Mathis CA, Morris JC, Mintun MA (2005) Molecular, structural, and functional characterization of Alzheimer's disease: evidence for a relationship between default activity, amyloid, and memory. *J Neurosci* 25:7709-17.

Bulte DP, Chiarelli PA, Wise RG, Jezzard P (2007) Cerebral perfusion response to hyperoxia. *J Cereb Blood Flow Metab* 27:69-75.

Buxton RB, Frank LR, Wong EC, Siewert B, Warach S, Edelman RR (1998) A general kinetic model for quantitative perfusion imaging with arterial spin labeling. *Magn Reson Med* 40:383-96.

Cauli B, Hamel E (2010) Revisiting the role of neurons in neurovascular coupling. *Front Neuroenergetics* 2:9.

Cepeda NJ, Kramer AF, Gonzalez de Sather JCM (2001) Changes in executive control across the life span: Examination of task-switching performance. *Developmental Psychology* 37:715-30.

Champe PC, Harvey RA, Ferrier DR. (2008). *Lippincott's Illustrated Reviews Biochemistry*. 4th edition ed. Baltimore: Wolters Kluwer and Lippincott Williams & Wilkins.

Chanarin I, Brozovic M, Tidmarsh E, Waters D. (1984). *Blood and its Disease*. Third Edition ed. New York: Churchill Livingstone.

Chiarelli PA, Bulte DP, Piechnik S, Jezzard P (2007a) Sources of systematic bias in hypercapnia-calibrated functional MRI estimation of oxygen metabolism. *Neuroimage* 34:35-43.

Chiarelli PA, Bulte DP, Wise R, Gallichan D, Jezzard P (2007b) A calibration method for quantitative BOLD fMRI based on hyperoxia. *Neuroimage* 37:808-20.

Cohen ER, Ugurbil K, Kim SG (2002) Effect of basal conditions on the magnitude and dynamics of the blood oxygenation level-dependent fMRI response. *J Cereb Blood Flow Metab* 22:1042-53.

Coles JP, Fryer TD, Bradley PG, Nortje J, Smielewski P, Rice K, Clark JC, Pickard JD, Menon DK (2006) Intersubject variability and reproducibility of 15O PET studies. *J Cereb Blood Flow Metab* 26:48-57.

Craik FI (1983) On the transfer of information from temporal to permanent memory. *Philosophical transactions of the Royal Society of London* 302:341-59.

D'Esposito M, Deouell LY, Gazzaley A (2003) Alterations in the BOLD fMRI signal with ageing and disease: a challenge for neuroimaging. *Nat Rev Neurosci* 4:863-72.

Davis TL, Kwong KK, Weisskoff RM, Rosen BR (1998) Calibrated functional MRI: mapping the dynamics of oxidative metabolism. *Proc Natl Acad Sci U S A* 95:1834-9.

de Boorder MJ, Hendrikse J, van der Grond J (2004) Phase-contrast magnetic resonance imaging measurements of cerebral autoregulation with a breath-hold challenge: a feasibility study. *Stroke* 35:1350-4.

Dean JB, Mulkey DK, Henderson RA, 3rd, Potter SJ, Putnam RW (2004) Hyperoxia, reactive oxygen species, and hyperventilation: oxygen sensitivity of brain stem neurons. *J Appl Physiol* 96:784-91.

Demchenko IT, Oury TD, Crapo JD, Piantadosi CA (2002) Regulation of the brain's vascular responses to oxygen. *Circ Res* 91:1031-7.

Deshpande G, Kerssens C, Sebel PS, Hu X Altered local coherence in the default mode network due to sevoflurane anesthesia. *Brain Res*.

Devous MD, Sr., Stokely EM, Chehabi HH, Bonte FJ (1986) Normal distribution of regional cerebral blood flow measured by dynamic single-photon emission tomography. *J Cereb Blood Flow Metab* 6:95-104.

Du F, Zhu XH, Zhang Y, Friedman M, Zhang N, Ugurbil K, Chen W (2008) Tightly coupled brain activity and cerebral ATP metabolic rate. *Proc Natl Acad Sci U S A* 105:6409-14.

Dulla CG, Dobelis P, Pearson T, Frenguelli BG, Staley KJ, Masino SA (2005) Adenosine and ATP link PCO2 to cortical excitability via pH. *Neuron* 48:1011-23.

Fernandez-Seara MA, Techawiboonwong A, Detre JA, Wehrli FW (2006) MR susceptometry for measuring global brain oxygen extraction. *Magn Reson Med* 55:967-73.

Floyd TF, Clark JM, Gelfand R, Detre JA, Ratcliffe S, Guvakov D, Lambertsen CJ, Eckenhoff RG (2003) Independent cerebral vasoconstrictive effects of hyperoxia and accompanying arterial hypocapnia at 1 ATA. *J Appl Physiol* 95:2453-61.

Folstein MF, Folstein SE, McHugh PR (1975) "Mini-mental state". A practical method for grading the cognitive state of patients for the clinician. *J Psychiatr Res* 12:189-98.

Fox PT, Raichle ME (1986) Focal physiological uncoupling of cerebral blood flow and oxidative metabolism during somatosensory stimulation in human subjects. *Proc Natl Acad Sci U S A* 83:1140-4.

Fox PT, Raichle ME, Mintun MA, Dence C (1988) Nonoxidative glucose consumption during focal physiologic neural activity. *Science* 241:462-4.

Frackowiak RS, Lenzi GL, Jones T, Heather JD (1980) Quantitative measurement of regional cerebral blood flow and oxygen metabolism in man using 15O and positron emission tomography: theory, procedure, and normal values. *J Comput Assist Tomogr* 4:727-36.

Frahm J, Bruhn H, Merboldt KD, Hanicke W (1992) Dynamic MR imaging of human brain oxygenation during rest and photic stimulation. *J Magn Reson Imaging* 2:501-5.

Fraigne JJ, Dunin-Barkowski WL, Orem JM (2008) Effect of hypercapnia on sleep and breathing in unanesthetized cats. *Sleep* 31:1025-33.

Frisard MI, Broussard A, Davies SS, Roberts LJ, 2nd, Rood J, de Jonge L, Fang X, Jazwinski SM, Deutsch WA, Ravussin E (2007) Aging, resting metabolic rate, and oxidative damage: results from the Louisiana Healthy Aging Study. *J Gerontol A Biol Sci Med Sci* 62:752-9.

Fukuda T, Hisano S, Toyooka H (2006) Moderate hypercapnia-induced anesthetic effects and endogenous opioids. *Neurosci Lett* 403:20-3.

Golay X, Silvennoinen MJ, Zhou J, Clingman CS, Kauppinen RA, Pekar JJ, van Zij PC (2001) Measurement of tissue oxygen extraction ratios from venous blood T(2): increased precision and validation of principle. *Magn Reson Med* 46:282-91.

Gonzalez-At JB, Alsop DC, Detre JA (2000) Cerebral perfusion and arterial transit time changes during task activation determined with continuous arterial spin labeling. *Magn Reson Med* 43:739-46.

Gourine AV, Llaudet E, Dale N, Spyer KM (2005) ATP is a mediator of chemosensory transduction in the central nervous system. *Nature* 436:108-11.

Greicius MD, Kiviniemi V, Tervonen O, Vainionpaa V, Alahuhta S, Reiss AL, Menon V (2008) Persistent default-mode network connectivity during light sedation. *Hum Brain Mapp* 29:839-47.

Gutchess AH, Welsh RC, Hedden T, Bangert A, Minear M, Liu LL, Park DC (2005) Aging and the neural correlates of successful picture encoding:

frontal activations compensate for decreased medial-temporal activity. *J Cogn Neurosci* 17:84-96.

Guyton AC, Hall JE (2005) Respiration. In: *Textbook of Medical Physiology* (Guyton AC, Hall JE, eds), 11th edition ed.: Saunders, Elsevier.

Haacke EM, Lai S, Reichenbach JR, Kuppusamy K, Hoogenraad FG, Takeichi H, Lin W (1997) In vivo measurement of blood oxygen saturation using magnetic resonance imaging: a direct validation of the blood oxygen level dependent concept in functional brain imaging. *Human Brain Mapping* 5:341-6.

Haacke EM, Brown RW, Thompson MR, Venkatesan R. (1999) MR Angiography and Flow Quantification. In: *Magnetic Resonance Imaging: Physical Principles and Sequence Design*: Wiley-Liss

Hagstadius S, Risberg J (1989) Regional cerebral blood flow characteristics and variations with age in resting normal subjects. *Brain Cogn* 10:28-43.

Hamberger A, Hyden H (1963) Inverse enzymatic changes in neurons and glia during increased function and hypoxia. *J Cell Biol* 16:521-5.

Harik N, Harik SI, Kuo NT, Sakai K, Przybylski RJ, LaManna JC (1996) Time-course and reversibility of the hypoxia-induced alterations in cerebral vascularity and cerebral capillary glucose transporter density. *Brain Res* 737:335-8.

Harik SI, Lust WD, Jones SC, Lauro KL, Pundik S, LaManna JC (1995) Brain glucose metabolism in hypobaric hypoxia. *J Appl Physiol* 79:136-40.

Hasher L, Zacks RT (1988) Working memory, comprehension and aging: A review and a new view. In: *The Psychology of Learning and Motivation* (Bower GH, ed), Vol. 22, San Diego, CA: Academic Press, 193-225.

Hattori N, Bergsneider M, Wu HM, Glenn TC, Vespa PM, Hovda DA, Phelps ME, Huang SC (2004) Accuracy of a method using short inhalation of (15)O-O(2) for measuring cerebral oxygen extraction fraction with PET in healthy humans. *J Nucl Med* 45:765-70.

Hayashi T, Suzuki A, Hatazawa J, Hadeishi H, Shirane R, Tominaga T, Yasui N (2008) Post-operative changes of cerebral circulation and metabolism in

the acute stage of low-grade aneurysmal subarachnoid hemorrhage. *Neurol Res* 30:678-83.

He X, Yablonskiy DA (2007) Quantitative BOLD: mapping of human cerebral deoxygenated blood volume and oxygen extraction fraction: default state. *Magn Reson Med* 57:115-26.

He X, Zhu M, Yablonskiy DA (2008) Validation of oxygen extraction fraction measurement by qBOLD technique. *Magn Reson Med* 60:882-8.

Hendrikse J, Lu H, van der Grond J, Van Zijl PC, Golay X (2003) Measurements of cerebral perfusion and arterial hemodynamics during visual stimulation using TURBO-TILT. *Magn Reson Med* 50:429-33.

Heo S, Prakash RS, Voss MW, Erickson KI, Ouyang C, Sutton BP, Kramer AF (2009) Resting hippocampal blood flow, spatial memory and aging. *Brain Res*.

Herscovitch P, Markham J, Raichle ME (1983) Brain blood flow measured with intravenous H2(15)O. I. Theory and error analysis. *J Nucl Med* 24:782-9.

Herscovitch P, Raichle ME (1985) What is the correct value for the brain--blood partition coefficient for water? *J Cereb Blood Flow Metab* 5:65-9.

Hoge RD, Atkinson J, Gill B, Crelier GR, Marrett S, Pike GB (1999) Linear coupling between cerebral blood flow and oxygen consumption in activated human cortex. *Proc Natl Acad Sci U S A* 96:9403-8.

Hong LE, Gu H, Yang Y, Ross TJ, Salmeron BJ, Buchholz B, Thaker GK, Stein EA (2009) Association of nicotine addiction and nicotine's actions with separate cingulate cortex functional circuits. *Arch Gen Psychiatry* 66:431-41.

Horovitz SG, Braun AR, Carr WS, Picchioni D, Balkin TJ, Fukunaga M, Duyn JH (2009) Decoupling of the brain's default mode network during deep sleep. *Proc Natl Acad Sci U S A* 106:11376-81.

Horvath I, Sandor NT, Ruttner Z, McLaughlin AC (1994) Role of nitric oxide in regulating cerebrocortical oxygen consumption and blood flow during hypercapnia. *J Cereb Blood Flow Metab* 14:503-9.

Hua J, Stevens RD, Huang AJ, Pekar JJ, van Zijl PC (2011) Physiological origin for the BOLD poststimulus undershoot in human brain: vascular compliance versus oxygen metabolism. *J Cereb Blood Flow Metab*.

Huettel SA, Song AW, McCarthy G. (2004). *Functional Magnetic Resonance Imaging*. Sunderland: Sinauer Associates, 492pp.

Hyder F, Chase JR, Behar KL, Mason GF, Siddeek M, Rothman DL, Shulman RG (1996) Increased tricarboxylic acid cycle flux in rat brain during forepaw stimulation detected with 1H[13C]NMR. *Proc Natl Acad Sci U S A* 93:7612-7.

Iadecola C, Park L, Capone C (2009) Threats to the mind: aging, amyloid, and hypertension. *Stroke* 40:S40-4.

Ibaraki M, Miura S, Shimosegawa E, Sugawara S, Mizuta T, Ishikawa A, Amano M (2008) Quantification of cerebral blood flow and oxygen metabolism with 3-dimensional PET and 15O: validation by comparison with 2-dimensional PET. *J Nucl Med* 49:50-9.

Ishii K, Sasaki M, Kitagaki H, Sakamoto S, Yamaji S, Maeda K (1996) Regional difference in cerebral blood flow and oxidative metabolism in human cortex. *J Nucl Med* 37:1086-8.

Ito H, Kanno I, Fukuda H (2005) Human cerebral circulation: positron emission tomography studies. *Ann Nucl Med* 19:65-74.

Jain V, Langham MC, Wehrli FW (2010) MRI estimation of global brain oxygen consumption rate. *J Cereb Blood Flow Metab* 30:1598-607.

Jones M, Berwick J, Hewson-Stoate N, Gias C, Mayhew J (2005) The effect of hypercapnia on the neural and hemodynamic responses to somatosensory stimulation. *Neuroimage* 27:609-23.

Kastrup A, Li TQ, Glover GH, Moseley ME (1999) Cerebral blood flow-related signal changes during breath-holding. *AJNR Am J Neuroradiol* 20:1233-8.

Kety SS, Schmidt CF (1948a) The Nitrous Oxide Method for the Quantitative Determination of Cerebral Blood Flow in Man: Theory, Procedure and Normal Values. *J Clin Invest* 27:476-83.

Kety SS, Schmidt CF (1948b) The Effects of Altered Arterial Tensions of Carbon Dioxide and Oxygen on Cerebral Blood Flow and Cerebral Oxygen Consumption of Normal Young Men. *J Clin Invest* 27:484-92.

Kety SS (1956) Human cerebral blood flow and oxygen consumption as related to aging. *J Chronic Dis* 3:478-86.

Kiloh LG, McComas AJ, osselton JW. (1972). *Clinical Electroencephalography*. Third ed.: APPLETON-CENTURY-CROFTS.

Kim SG, Ugurbil K (1997) Comparison of blood oxygenation and cerebral blood flow effects in fMRI: estimation of relative oxygen consumption change. *Magn Reson Med* 38:59-65.

Kliefoth AB, Grubb RL, Jr., Raichle ME (1979) Depression of cerebral oxygen utilization by hypercapnia in the rhesus monkey. *J Neurochem* 32:661-3.

Kogure K, Busto R, Scheinberg P, Reinmuth O (1975) Dynamics of cerebral metabolism during moderate hypercapnia. *J Neurochem* 24:471-8.

Krems C, Luhrmann PM, Strassburg A, Hartmann B, Neuhauser-Berthold M (2005) Lower resting metabolic rate in the elderly may not be entirely due to changes in body composition. *Eur J Clin Nutr* 59:255-62.

Kuhl DE, Alavi A, Hoffman EJ, Phelps ME, Zimmerman RA, Obrist WD, Bruce DA, Greenberg JH, Uzzell B (1980) Local cerebral blood volume in head-injured patients. Determination by emission computed tomography of 99mTc-labeled red cells. *J Neurosurg* 52:309-20.

Kwong KK, Belliveau JW, Chesler DA, Goldberg IE, Weisskoff RM, Poncelet BP, Kennedy DN, Hoppel BE, Cohen MS, Turner R, Cheng HM, Brady TJ, Rosen BR (1992) Dynamic magnetic resonance imaging of human brain activity during primary sensory stimulation. *Proc Natl Acad Sci U S A* 89:5675-9.

LaManna JC, Harik SI (1997) Brain metabolic and vascular adaptations to hypoxia in the rat. Review and update. *Adv Exp Med Biol* 428:163-7.

Lassen NA (1978) Cerebral blood flow in cerebral ischemia. A review (with 1 color plate). *Eur Neurol* 17 Suppl 1:4-8.

Leenders KL, Perani D, Lammertsma AA, Heather JD, Buckingham P, Healy MJ, Gibbs JM, Wise RJ, Hatazawa J, Herold S, et al. (1990) Cerebral blood flow, blood volume and oxygen utilization. Normal values and effect of age. *Brain* 113 (Pt 1):27-47.

Levy RH, Mattson RH, Meldrum BS. (1995). *Antiepileptic drugs*. Fourth Edition ed. New York: Raven Press.

Li M, Ratcliffe SJ, Knoll F, Wu J, Ances B, Mardini W, Floyd TF (2006) Aging: impact upon local cerebral oxygenation and blood flow with acute isovolemic hemodilution. *J Neurosurg Anesthesiol* 18:125-31.

Liu P, Uh J, Lu H (2011) Determination of spin compartment in arterial spin labeling MRI. *Magn Reson Med* 65:120-7.

Lu H, Clingman C, Golay X, van Zijl PC (2004) Determining the longitudinal relaxation time (T1) of blood at 3.0 Tesla. *Magn Reson Med* 52:679-82.

Lu H. (2008) Magnetization "reset" for non-steady-state blood spins in Vascular-Space-Occupancy (VASO) fMRI. . In: *In. Proc Intl Soc Mag Reson Med*, Toronto, Canada, p 406

Lu H, Ge Y (2008a) Quantitative evaluation of oxygenation in venous vessels using T2-Relaxation-Under-Spin-Tagging MRI. *Magn Reson Med* 60:357-63.

Lu H, Ge Y (2008b) Quantitative evaluation of oxygenation in venous vessels using T2-Relaxation-Under-Spin-Tagging MRI. *Magn Reson Med* in press.

Luhrmann PM, Bender R, Edelmann-Schafer B, Neuhauser-Berthold M (2009) Longitudinal changes in energy expenditure in an elderly German population: a 12-year follow-up. *Eur J Clin Nutr* 63:986-92.

Maandag NJ, Coman D, Sanganahalli BG, Herman P, Smith AJ, Blumenfeld H, Shulman RG, Hyder F (2007) Energetics of neuronal signaling and fMRI activity. *Proc Natl Acad Sci U S A* 104:20546-51.

Magnoni S, Ghisoni L, Locatelli M, Caimi M, Colombo A, Valeriani V, Stocchetti N (2003) Lack of improvement in cerebral metabolism after hyperoxia in severe head injury: a microdialysis study. *J Neurosurg* 98:952-8.

Mantini D, Perrucci MG, Del Gratta C, Romani GL, Corbetta M (2007) Electrophysiological signatures of resting state networks in the human brain. *Proc Natl Acad Sci U S A* 104:13170-5.

Marchal G, Rioux P, Petit-Taboue MC, Sette G, Travere JM, Le Poec C, Courtheoux P, Derlon JM, Baron JC (1992) Regional cerebral oxygen consumption, blood flow, and blood volume in healthy human aging. *Arch Neurol* 49:1013-20.

Mark CI, Fisher JA, Pike GB (2011) Improved fMRI calibration: precisely controlled hyperoxic versus hypercapnic stimuli. *Neuroimage* 54:1102-11.

Martin AJ, Friston KJ, Colebatch JG, Frackowiak RS (1991) Decreases in regional cerebral blood flow with normal aging. *J Cereb Blood Flow Metab* 11:684-9.

Mintun MA, Raichle ME, Martin WR, Herscovitch P (1984) Brain oxygen utilization measured with O-15 radiotracers and positron emission tomography. *J Nucl Med* 25:177-87.

Miura SA, Schapiro MB, Grady CL, Kumar A, Salerno JA, Kozachuk WE, Wagner E, Rapoport SI, Horwitz B (1990) Effect of gender on glucose utilization rates in healthy humans: a positron emission tomography study. *J Neurosci Res* 27:500-4.

Moore KL, Dalley AF. (1999). *Clinically Oriented Anatomy*. Fourth ed.: Lippincott Williams & Wilkins.

Moosmann M, Ritter P, Krastel I, Brink A, Thees S, Blankenburg F, Taskin B, Obrig H, Villringer A (2003) Correlates of alpha rhythm in functional magnetic resonance imaging and near infrared spectroscopy. *Neuroimage* 20:145-58.

Mulkey DK, Henderson RA, 3rd, Olson JE, Putnam RW, Dean JB (2001) Oxygen measurements in brain stem slices exposed to normobaric hyperoxia and hyperbaric oxygen. *J Appl Physiol* 90:1887-99.

Niedermeyer E, da Silva FHL. (2005). *Electroencephalography: basic principles, clinical applications, and related fields*. Fifth Edition ed. Philadelphia: Lippincott Williams & Wilkins.

Nishimura N, Iwasaki K, Ogawa Y, Shibata S (2007) Oxygen administration, cerebral blood flow velocity, and dynamic cerebral autoregulation. *Aviat Space Environ Med* 78:1121-7.

Nofzinger EA, Buysse DJ, Miewald JM, Meltzer CC, Price JC, Sembrat RC, Ombao H, Reynolds CF, Monk TH, Hall M, Kupfer DJ, Moore RY (2002) Human regional cerebral glucose metabolism during non-rapid eye movement sleep in relation to waking. *Brain* 125:1105-15.

Noth U, Kotajima F, Deichmann R, Turner R, Corfield DR (2008) Mapping of the cerebral vascular response to hypoxia and hypercapnia using quantitative perfusion MRI at 3 T. *NMR Biomed* 21:464-72.

Novack P, Shenkin HA, Bortin L, Goluboff B, Soffe AM (1953) The effects of carbon dioxide inhalation upon the cerebral blood flow and cerebral oxygen consumption in vascular disease. *J Clin Invest* 32:696-702.

Ogawa S, Tank DW, Menon R, Ellermann JM, Kim SG, Merkle H, Ugurbil K (1992) Intrinsic signal changes accompanying sensory stimulation: functional brain mapping with magnetic resonance imaging. *Proc Natl Acad Sci U S A* 89:5951-5.

Oja JM, Gillen JS, Kauppinen RA, Kraut M, van Zijl PC (1999) Determination of oxygen extraction ratios by magnetic resonance imaging. *J Cereb Blood Flow Metab* 19:1289-95.

Park DC, Smith AD, Lautenschlager G, Earles JL, Frieske D, Zwahr M, Gaines CL (1996) Mediators of long-term memory performance across the life span. *Psychol Aging* 11:621-37.

Park DC, Lautenschlager G, Hedden T, Davidson NS, Smith AD, Smith PK (2002) Models of visuospatial and verbal memory across the adult life span. *Psychol Aging* 17:299-320.

Pascual JM, Carceller F, Roda JM, Cerdan S (1998) Glutamate, glutamine, and GABA as substrates for the neuronal and glial compartments after focal cerebral ischemia in rats. *Stroke* 29:1048-56; discussion 56-7.

Pell GS, Thomas DL, Lythgoe MF, Calamante F, Howseman AM, Gadian DG, Ordidge RJ (1999) Implementation of quantitative FAIR perfusion

imaging with a short repetition time in time-course studies. *Magn Reson Med* 41:829-40.

Perlmutter JS, Powers WJ, Herscovitch P, Fox PT, Raichle ME (1987) Regional asymmetries of cerebral blood flow, blood volume, and oxygen utilization and extraction in normal subjects. *J Cereb Blood Flow Metab* 7:64-7.

Powers WJ, Grubb RL, Jr., Darriet D, Raichle ME (1985) Cerebral blood flow and cerebral metabolic rate of oxygen requirements for cerebral function and viability in humans. *J Cereb Blood Flow Metab* 5:600-8.

Prichard JW, Alger JR, Behar KL, Petroff OA, Shulman RG (1983) Cerebral metabolic studies in vivo by 31P NMR. *Proc Natl Acad Sci U S A* 80:2748-51.

Qin Q, Grgac K, van Zijl PC (2011) Determination of whole-brain oxygen extraction fractions by fast measurement of blood T(2) in the jugular vein. *Magn Reson Med* 65:471-9.

Raichle ME, Martin WR, Herscovitch P, Mintun MA, Markham J (1983) Brain blood flow measured with intravenous H2(15)O. II. Implementation and validation. *J Nucl Med* 24:790-8.

Raichle ME, Mintun MA (2006) Brain work and brain imaging. *Annu Rev Neurosci* 29:449-76.

Raz N, Williamson A, Gunning-Dixon F, Head D, Acker JD (2000) Neuroanatomical and cognitive correlates of adult age differences in acquisition of a perceptual-motor skill. *Microsc Res Tech* 51:85-93.

Raz N, Kennedy KM (2009) A systems approach to age-related change: Neuroanatomical changes, their modifiers, and cognitive correlates. In: *Imaging the Aging Brain* (Jagust W, D'Esposito M, eds), New York, NY: Oxford University Press, 43-70.

Richards EM, Fiskum G, Rosenthal RE, Hopkins I, McKenna MC (2007) Hyperoxic reperfusion after global ischemia decreases hippocampal energy metabolism. *Stroke* 38:1578-84.

Rodriguez G, Warkentin S, Risberg J, Rosadini G (1988) Sex differences in regional cerebral blood flow. *J Cereb Blood Flow Metab* 8:783-9.

Rosenbaum P (2003) Controversial treatment of spasticity: exploring alternative therapies for motor function in children with cerebral palsy. *J Child Neurol* 18 Suppl 1:S89-94.

Rostrup E, Law I, Blinkenberg M, Larsson HB, Born AP, Holm S, Paulson OB (2000) Regional differences in the CBF and BOLD responses to hypercapnia: a combined PET and fMRI study. *Neuroimage* 11:87-97.

Rothman DL, Novotny EJ, Shulman GI, Howseman AM, Petroff OA, Mason G, Nixon T, Hanstock CC, Prichard JW, Shulman RG (1992) 1H-[13C] NMR measurements of [4-13C]glutamate turnover in human brain. *Proc Natl Acad Sci U S A* 89:9603-6.

Roy CS, Sherrington CS (1890) On the Regulation of the Blood-supply of the Brain. *J Physiol* 11:85-158 17.

Rypma B, D'Esposito M (2000) Isolating the neural mechanisms of age-related changes in human working memory. *Nat Neurosci* 3:509-15.

Salat DH, Buckner RL, Snyder AZ, Greve DN, Desikan RS, Busa E, Morris JC, Dale AM, Fischl B (2004) Thinning of the cerebral cortex in aging. *Cereb Cortex* 14:721-30.

Salthouse TA, Mitchell DR, Skovronek E, Babcock RL (1989) Effects of adult age and working memory on reasoning and spatial abilities. *J Exp Psychol Learn Mem Cogn* 15:507-16.

Salthouse TA (1996) The processing-speed theory of adult age differences in cognition. *Psychol Rev* 103:403-28.

Shaw TG, Mortel KF, Meyer JS, Rogers RL, Hardenberg J, Cutaia MM (1984) Cerebral blood flow changes in benign aging and cerebrovascular disease. *Neurology* 34:855-62.

Shen D, Davatzikos C (2002) HAMMER: hierarchical attribute matching mechanism for elastic registration. *IEEE Trans Med Imaging* 21:1421-39.

Shulman RG, Rothman DL, Hyder F (1999) Stimulated changes in localized cerebral energy consumption under anesthesia. *Proc Natl Acad Sci U S A* 96:3245-50.

Sicard KM, Duong TQ (2005) Effects of hypoxia, hyperoxia, and hypercapnia on baseline and stimulus-evoked BOLD, CBF, and CMRO2 in spontaneously breathing animals. *Neuroimage* 25:850-8.

Siegelbaum SA, Koester J (2000) Cell and Molecular Biology of the Neuron. In: *Principles of Neural Science* (Kandel ER, Schwartz JH, Jessell TM, eds), 4th edition ed., New York: McGraw-Hill Companies.

Silvennoinen MJ, Clingman CS, Golay X, Kauppinen RA, van Zijl PC (2003) Comparison of the dependence of blood R2 and R2* on oxygen saturation at 1.5 and 4.7 Tesla. *Magn Reson Med* 49:47-60.

Smirnakis SM, Schmid MC, Weber B, Tolias AS, Augath M, Logothetis NK (2007) Spatial specificity of BOLD versus cerebral blood volume fMRI for mapping cortical organization. *J Cereb Blood Flow Metab* 27:1248-61.

Spilt A, Box FM, van der Geest RJ, Reiber JH, Kunz P, Kamper AM, Blauw GJ, van Buchem MA (2002) Reproducibility of total cerebral blood flow measurements using phase contrast magnetic resonance imaging. *J Magn Reson Imaging* 16:1-5.

St-Onge MP (2005) Relationship between body composition changes and changes in physical function and metabolic risk factors in aging. *Curr Opin Clin Nutr Metab Care* 8:523-8.

Stefanovic B, Pike GB (2004) Human whole-blood relaxometry at 1.5 T: Assessment of diffusion and exchange models. *Magn Reson Med* 52:716-23.

Thulborn KR, Waterton JC, Matthews PM, Radda GK (1982) Oxygenation dependence of the transverse relaxation time of water protons in whole blood at high field. *Biochim Biophys Acta* 714:265-70.

Tisdall MM, Tachtsidis I, Leung TS, Elwell CE, Smith M (2007) Near-infrared spectroscopic quantification of changes in the concentration of oxidized cytochrome c oxidase in the healthy human brain during hypoxemia. *J Biomed Opt* 12:024002.

van Zijl PC, Eleff SM, Ulatowski JA, Oja JM, Ulug AM, Traystman RJ, Kauppinen RA (1998) Quantitative assessment of blood flow, blood

volume and blood oxygenation effects in functional magnetic resonance imaging. *Nat Med* 4:159-67.

Vanzetta I, Grinvald A (1999) Increased cortical oxidative metabolism due to sensory stimulation: implications for functional brain imaging. *Science* 286:1555-8.

Vazquez AL, Masamoto K, Fukuda M, Kim SG (2010) Cerebral oxygen delivery and consumption during evoked neural activity. *Front Neuroenergetics* 2:11.

Videen TO, Perlmutter JS, Herscovitch P, Raichle ME (1987) Brain blood volume, flow, and oxygen utilization measured with 15O radiotracers and positron emission tomography: revised metabolic computations. *J Cereb Blood Flow Metab* 7:513-6.

Wang J, Alsop DC, Li L, Listerud J, Gonzalez-At JB, Schnall MD, Detre JA (2002) Comparison of quantitative perfusion imaging using arterial spin labeling at 1.5 and 4.0 Tesla. *Magn Reson Med* 48:242-54.

Wong EC (2007) Vessel-encoded arterial spin-labeling using pseudocontinuous tagging. *Magn Reson Med* 58:1086-91.

Wright GA, Hu BS, Macovski A (1991) Estimating oxygen saturation of blood in vivo with MR imaging at 1.5 T. *J Magn Reson Imaging* 1:275-83.

Wu WC, Fernandez-Seara M, Detre JA, Wehrli FW, Wang J (2007) A theoretical and experimental investigation of the tagging efficiency of pseudocontinuous arterial spin labeling. *Magn Reson Med* 58:1020-7.

Xiong J, Parsons LM, Gao JH, Fox PT (1999) Interregional connectivity to primary motor cortex revealed using MRI resting state images. *Hum Brain Mapp* 8:151-6.

Xu F, Ge Y, Lu H (2009) Noninvasive quantification of whole-brain cerebral metabolic rate of oxygen (CMRO2) by MRI. *Magn Reson Med* 62:141-8.

Xu F, Yezhuvath US, Liu P, Lu H. (2010) Hypoxia and hyperoxia alter brain metabolism in awake human. In: *Proc Intl Soc Mag Reson Med*, Stockholm, Sweden, p 1032

Xu F, Uh J, Brier MR, Hart J, Jr., Yezhuvath US, Gu H, Yang Y, Lu H (2011) The influence of carbon dioxide on brain activity and metabolism in conscious humans. *J Cereb Blood Flow Metab* 31:58-67.

Yablonskiy DA, Haacke EM (1994) Theory of NMR signal behavior in magnetically inhomogeneous tissues: the static dephasing regime. *Magn Reson Med* 32:749-63.

Yamaguchi T, Kanno I, Uemura K, Shishido F, Inugami A, Ogawa T, Murakami M, Suzuki K (1986) Reduction in regional cerebral metabolic rate of oxygen during human aging. *Stroke* 17:1220-8.

Yang SP, Krasney JA (1995) Cerebral blood flow and metabolic responses to sustained hypercapnia in awake sheep. *J Cereb Blood Flow Metab* 15:115-23.

Yang Y, Engelien W, Xu S, Gu H, Silbersweig DA, Stern E (2000) Transit time, trailing time, and cerebral blood flow during brain activation: measurement using multislice, pulsed spin-labeling perfusion imaging. *Magn Reson Med* 44:680-5.

Zappe AC, Uludag K, Logothetis NK (2008a) Direct measurement of oxygen extraction with fMRI using 6% CO2 inhalation. *Magn Reson Imaging* 26:961-7.

Zappe AC, Uludag K, Oeltermann A, Ugurbil K, Logothetis NK (2008b) The influence of moderate hypercapnia on neural activity in the anesthetized nonhuman primate. *Cereb Cortex* 18:2666-73.

Zhao JM, Clingman CS, Narvainen MJ, Kauppinen RA, van Zijl PC (2007) Oxygenation and hematocrit dependence of transverse relaxation rates of blood at 3T. *Magn Reson Med* 58:592-7.

Zhu XH, Zhang Y, Tian RX, Lei H, Zhang N, Zhang X, Merkle H, Ugurbil K, Chen W (2002) Development of (17)O NMR approach for fast imaging of cerebral metabolic rate of oxygen in rat brain at high field. *Proc Natl Acad Sci U S A* 99:13194-9.

Zhu XH, Zhang N, Zhang Y, Zhang X, Ugurbil K, Chen W (2005) In vivo 17O NMR approaches for brain study at high field. *NMR Biomed* 18:83-103.